

MEHRDAD MIRSHAFIEI

# Ultra-wideband Indoor Communications Using Optical Technology

Thèse présentée  
à la Faculté des études supérieures et postdoctorales de l'Université Laval  
dans le cadre du programme de doctorat en génie électrique  
pour l'obtention du grade de Philosophiæ Doctor (Ph.D.)

Faculté des sciences et de génie  
UNIVERSITÉ LAVAL  
QUÉBEC

2013



# Résumé

La communication ultra large bande (UWB) a attiré une énorme quantité de recherches ces dernières années, surtout après la présentation du masque spectral de US Federal Communications Commission (FCC). Les impulsions ultra-courtes permettent de très hauts débits de faible puissance tout en éliminant les interférences avec les systèmes existants à bande étroite. La faible puissance, cependant, limite la portée de propagation des radios UWB à quelques mètres pour la transmission sans fil à l'intérieur d'une pièce. En outre, des signaux UWB reçus sont étendus dans le temps en raison de la propagation par trajet multiple qui résulte en beaucoup d'interférence inter-symbole (ISI) à haut débit.

Le monocycle Gaussien, l'impulsion la plus commune dans UWB, a une mauvaise couverture sous le masque de la FCC. Dans cette thèse, nous démontrons des transmetteurs qui sont capables de générer des impulsions UWB avec une efficacité de puissance élevée. Une impulsion efficace résulte dans un rapport de signal à bruit (SNR) supérieur au récepteur en utilisant plus de la puissance disponible sous le masque spectral de la FCC. On produit les impulsions dans le domaine optique et utilise la fibre optique pour les transporter sur plusieurs kilomètres pour la distribution dans un réseau optique passif. La fibre optique est très fiable pour le transport des signaux radio avec une faible consommation de puissance. On utilise les éléments simples comme un modulateur Mach-Zehnder ou un résonateur en anneau pour générer des impulsions, ce qui permet l'intégration dans le silicium. Compatible avec la technologie CMOS, la photonique sur silicium a un potentiel énorme pour abaisser le coût et l'encombrement des systèmes optiques. La photodétection convertit les impulsions optiques en impulsions électriques avant la transmission sur l'antenne du côté de l'utilisateur.

La réponse fréquentielle de l'antenne déforme la forme d'onde de l'impulsion UWB.

Nous proposons une technique d'optimisation non-linéaire qui prend en compte la distorsion d'antenne pour trouver des impulsions qui maximisent la puissance transmise, en respectant le masque spectral de la FCC. Nous travaillons avec trois antennes et concevons une impulsion unique pour chacune d'entre elle. L'amélioration de l'énergie des impulsions UWB améliore directement la SNR au récepteur. Les résultats de simulation montrent que les impulsions optimisées améliorent considérablement le taux d'erreur (BER) par rapport au monocycle Gaussien sous propagation par trajet multiple.

Notre autre contribution est l'évaluation d'un filtre adapté pour recevoir efficacement des impulsions UWB. Le filtre adapté est synthétisé et fabriqué en technologie microstrip, en collaboration avec l'Université McGill comme un dispositif de bande interdite électromagnétique. La réponse fréquentielle du filtre adapté montre une excellente concordance avec le spectre ciblé de l'impulsion UWB. Les mesures de BER confirment la performance supérieure du filtre adapté par rapport à un récepteur à conversion directe.

Le canal UWB est très riche en trajet multiple conduisant à l'ISI à haut débit. Notre dernière contribution est l'étude de performance des récepteurs en simulant un système avec des conditions de canaux réalistes. Les résultats de la simulation montrent que la performance d'un tel système se dégrade de façon significative pour les hauts débits. Afin de compenser la forte ISI dans les taux de transfert de données en Gb/s, nous étudions l'algorithme de Viterbi (VA) avec un nombre limité d'états et un égaliseur DFE (decision feedback equalizer). Nous examinons le nombre d'états requis dans le VA, et le nombre de coefficients du filtre dans le DFE pour une transmission fiable de UWB en Gb/s dans les canaux en ligne de vue. L'évaluation par simulation de BER confirme que l'égalisation améliore considérablement les performances par rapport à la détection de symbole. La DFE a une meilleure performance par rapport à la VA en utilisant une complexité comparable. La DFE peut couvrir une plus grande mémoire de canal avec un niveau de complexité relativement réduit.

# Abstract

Ultra-wideband (UWB) communication has attracted an enormous amount of research in recent years, especially after the introduction of the US Federal Communications Commission (FCC) spectral mask. Ultra-short pulses allow for very high bit-rates while low power eliminates interference with existing narrowband systems. Low power, however, limits the propagation range of UWB radios to a few meters for indoors wireless transmission. Furthermore, received UWB signals are spread in time because of multipath propagation which results in high intersymbol interference at high data rates.

Gaussian monocycle, the most commonly employed UWB pulse, has poor coverage under the FCC mask. In this thesis we demonstrate transmitters capable of generating UWB pulses with high power efficiency at Gb/s bit-rates. An efficient pulse results in higher signal-to-noise ratio (SNR) at the receiver by utilizing most of the available power under the FCC spectral mask. We generate the pulses in the optical domain and use optical fiber to transport the pulses over several kilometers for distribution in a passive optical network. Optical fiber is very reliable for transporting radio signals with low power consumption. We use simple elements such as a Mach Zehnder modulator or a ring resonator for pulse shaping, allowing for integration in silicon. Being compatible with CMOS technology, silicon photonics has huge potential for lowering the cost and bulkiness of optical systems. Photodetection converts the pulses to the electrical domain before antenna transmission at the user side.

The frequency response of UWB antennas distorts the UWB waveforms. We propose a nonlinear optimization technique which takes into account antenna distortion to find pulses that maximize the transmitted power, while respecting the FCC spectral mask. We consider three antennas and design a unique pulse for each. The energy im-

provement in UWB pulses directly improves the receiver SNR. Simulation results show that optimized pulses have a significant bit error rate (BER) performance improvement compared to the Gaussian monocycle under multipath propagation.

Our other contribution is evaluating a matched filter to receive efficiently designed UWB pulses. The matched filter is synthesized and fabricated in microstrip technology in collaboration with McGill University as an electromagnetic bandgap device. The frequency response of the matched filter shows close agreement with the target UWB pulse spectrum. BER measurements confirm superior performance of the matched filter compared to a direct conversion receiver.

The UWB channel is very rich in multipath leading to ISI at high bit rates. Our last contribution is investigating the performance of receivers by simulating a system employing realistic channel conditions. Simulation results show that the performance of such system degrades significantly for high data rates. To compensate the severe ISI at gigabit rates, we investigate the Viterbi algorithm (VA) with a limited number of states and the decision feedback equalizer (DFE). We examine the required number of states in the VA, and the number of taps in the DFE for reliable Gb/s UWB transmission for line-of-sight channels. Non-line-of-sight channels were also investigated at lower speeds. BER simulations confirm that equalization considerably improves the performance compared to symbol detection. The DFE results in better performance compared to the VA when using comparable complexity as the DFE can cover greater channel memory with a relatively low complexity level.

# Contents

Résumé	iii
Abstract	v
Contents	vii
Acknowledgements	x
List of Figures	xi
List of Tables	xvi
Acronyms and Abbreviations	xvii
<b>1 Introduction</b>	<b>1</b>
1.1 Motivation . . . . .	1
1.2 Objectives and Major Contributions . . . . .	3
1.3 Structure of the thesis . . . . .	4
<b>2 UWB communication systems</b>	<b>6</b>
2.1 UWB basics . . . . .	6
2.1.1 UWB applications . . . . .	9
2.1.2 Impulse radio vs. multiband UWB . . . . .	10
2.2 UWB pulse generation techniques . . . . .	11
2.2.1 Pulse generation in the electrical domain . . . . .	12
2.2.2 Pulse generation in the optical domain . . . . .	14
2.3 UWB channel models and measurements . . . . .	18
2.3.1 Path loss model . . . . .	18
2.3.2 Multipath model . . . . .	19
2.4 UWB antennas . . . . .	20
2.5 UWB receivers . . . . .	22

2.5.1	Coherent UWB receivers . . . . .	22
2.5.2	Noncoherent UWB receivers . . . . .	23
2.6	Conclusion . . . . .	26
<b>3</b>	<b>UWB Pulse generation techniques</b>	<b>28</b>
3.1	EIRP calculation method . . . . .	29
3.2	Upconversion of Gain-Switched Laser Pulses for Generation of UWB Signals . . . . .	33
3.2.1	Introduction . . . . .	33
3.2.2	Experimental setup . . . . .	35
3.2.3	Simulation and Experimental Results . . . . .	38
3.2.4	BER performance of the receiver . . . . .	43
3.3	Low Complexity generation of BPSK UWB signals . . . . .	47
3.3.1	Introduction . . . . .	47
3.3.2	Experimental Setup . . . . .	49
3.3.3	Theoretical Study . . . . .	50
3.3.4	Experimental Results and Discussion . . . . .	51
3.4	UWB waveform generation using a microring resonator . . . . .	56
3.4.1	Introduction . . . . .	56
3.4.2	Principle of Operation and RTR design . . . . .	60
3.4.3	Experimental Results and Discussion . . . . .	66
3.5	Conclusion . . . . .	67
<b>4</b>	<b>UWB pulse shaping: bypassing the limitations of the monocycle</b>	<b>70</b>
4.1	UWB Pulse Design . . . . .	72
4.2	Common UWB pulse shapes . . . . .	73
4.3	Antennas and Efficient UWB Pulses . . . . .	74
4.3.1	The SkyCross Antenna . . . . .	75
4.3.2	The circular monopole antenna . . . . .	76
4.3.3	The monopole antenna with two steps . . . . .	78
4.4	Experimental Validation . . . . .	78
4.4.1	Pulse Generation . . . . .	78
4.4.2	Pulse characterization . . . . .	80
4.5	Simulation Results and Discussion . . . . .	81
4.6	Conclusion . . . . .	85
<b>5</b>	<b>UWB receivers</b>	<b>86</b>



5.1	UWB Reception Using an EBG . . . . .	87
5.1.1	Introduction . . . . .	87
5.1.2	Experimental setup . . . . .	88
5.1.3	EBG Design and Fabrication . . . . .	90
5.1.4	Matched filter characterization . . . . .	91
5.1.5	BER measurement and discussion . . . . .	93
5.2	Equalizers for IR-UWB Linear Receivers . . . . .	95
5.2.1	System Model . . . . .	97
5.2.2	Equalization . . . . .	99
5.2.3	Simulation results . . . . .	101
5.3	Conclusion . . . . .	105
<b>6</b>	<b>Conclusions and Future Work</b>	<b>107</b>
	<b>Publication List</b>	<b>110</b>
	<b>Bibliography</b>	<b>112</b>

# Acknowledgements

There are many people who have helped me throughout the course of my graduate study. I would like to thank my advisor professor Leslie A. Rusch, for her guidance, encouragement and support throughout my graduate career. We have had regular discussions over the last six years. The opportunities for growth and the excitement of working in our group are deeply appreciated; I am honored to have had the chance to be part of it. My gratitude also goes to professor Sophie LaRochelle who was my M.Sc. cosupervisor and has continued to be a great inspiration for the work in this thesis. We held many meetings with professor LaRochelle to discuss optical aspects of this work.

I thank the members of the jury Prof. Jianping Yao, Prof. José Azaña, and Prof. Jean-Yves Chouinard for taking the time to read my thesis. I would also like to thank members of my pre-doctoral exam Prof. Tayeb Denidni and Prof. David Plant for their time and many fruitful comments about the project.

Several members of Leslie and Sophie group have contributed to this work and others have been good friends. I want to particularly thank David, Amir, Mehdi, Francesco, Ramtin, Alexandre, and Mansour. Being in COPL with you all has been a pleasure. Greatest thanks to Dr. Mohammad Abtahi without whom this project would have never started. He was always there with motivating discussions, and shared with me his technical experience. I would like to thank the COPL technicians Philippe Chrétien and Patrick LaRochelle for their help in experiments. Dr. Joshua Schwartz designed and fabricated the EBGs, many thanks to him for all the discussions we had. I am also grateful to Prof. Lukas Chrostowski for teaching me about silicon photonics and to Dan Deptuck for his help with chip layout.

My deepest appreciation goes to my parents Afsaneh and Ali for their support and kindness. They have always been there for me, provided me with the best education and encouraged me to learn. My brothers Farshad and Farzad and my final gratitude to my grandmother Afsar who has always encouraged me to become a scientist.

# List of Figures

1.1	FCC spectral masks for indoor and outdoor communication applications [1].	2
2.1	WiMedia landscape of UWB compared to Wireless local area networks (WLAN) [2]	8
2.2	(a) impulse radio (IR-UWB), and (b) multiband (MB-UWB).	11
2.3	UWB pulse generation techniques. (a) upconversion of baseband pulses, (b) shaping baseband pulses using a filter, (c) optical generation/transport of UWB signals, and (d) electrical UWB pulse generation.	12
2.4	Schematic diagram of pulse generation by spectral pulse shaping. SMF: single-mode fiber, FBG: fiber Bragg grating.	14
2.5	Block diagram of the UWB waveform generator.	16
2.6	A WDM-PON network transporting UWB radio signals.	17
2.7	Coherent receivers: The matched filter receiver (a), and the correlation receiver (b). ADC: analog-to-digital convertor.	22
2.8	Generic noncoherent UWB receiver structures: the energy detection (ED) for OOK receiver(a), the ED receiver for PPM modulation, and the DPSK noncoherent receiver.	25
3.1	(a) The experimental setup for measuring the antenna frequency response,(b) antenna frequency response, (c) antenna link delay, and (d) antenna reflection response.	30
3.2	(a) Smoothed antennas frequency response, (b) normalized time response.	32
3.3	PA frequency response.	32
3.4	Simplified block diagram of the proposed UWB waveform generator. GSL: gain switched laser, FBG: fiber Bragg grating, SMF: single-mode fiber.	33

3.5	The schematic diagram of the proposed UWB waveform generator, and the receiving schemes. GSL: gain-switched laser, PC: polarization controller, MZM: Mach-Zehnder modulator, SMF: single-mode fiber, FBG: fiber Bragg grating, EDFA: erbium-doped fiber amplifier, BPF: bandpass filter, VOA: variable optical attenuator, DL: delay line, ATT: attenuator, BPD: balanced photodetector, LNA: low-noise amplifier. . . . .	35
3.6	The simulated and measured response of the FBG at transmission and reflection. . . . .	37
3.7	(a) the simulated and measured response at the MZM output (from the positive input of the BPD), and the measured GSL pulse after 20 km fiber propagation (from the negative input of the BPD). (b) the simulated and measured UWB waveforms. (c) The normalized PSD and EIRP of the UWB pulse. . . . .	40
3.8	The normalized PSD of UWB waveforms for various optical fiber lengths plotted against the 3.1-10.6 GHz band of the FCC spectral mask. . . .	41
3.9	(a) UWB waveform generated using the FBG filter at the transmitter, (b) The normalized PSD and EIRP of the UWB pulse. . . . .	42
3.10	UWB transmitter with 20 km of SMF, (a) eyediagram of the transmit pulse, (b) eyediagram of the linear filter output, (c) eyediagram of the energy detector output, (d) BER versus average transmit power plotted for various wireless distances. . . . .	44
3.11	UWB transmitter with FBG filter, (a) eyediagram of the transmit pulse, (b) eyediagram of the linear filter output, (c) eyediagram of the energy detector output, (d) BER versus average transmit power plotted for various wireless distances. . . . .	46
3.12	(a) BER versus wireless transmission distance. The average transmit power is set to -6.5 dBm for the transmitter with the FBG filter. . . . .	47
3.13	The schematic diagram of the experimental setup. PC: polarization controller, MZM: Mach-Zehnder modulator, VOA: variable optical attenuator, SMF: single-mode fiber, PD: photodetector, LNA: low-noise amplifier, LPF: lowpass filter. . . . .	49
3.14	(a) The normalized transmit UWB signal, (b) the normalized received waveform, and (c) the power spectral density of the transmit pulse (red) and the EIRP (blue). . . . .	52
3.15	The multiband-UWB signals centered around (a) 5 GHz, (b) 6.8 GHz, and (c) 8.5 GHz. (d) The corresponding EIRP plots. . . . .	53

3.16	The PSK scheme. (a) The transmit UWB pulses, (b) the received waveforms, (c) the autocorrelation function of the received waveform, (d) superposition of a 1 and a 0, and (e) the EIRP of the 1 and 0 pulses. . . . .	55
3.17	The PSK signals. (a) The eyediagram of the UWB signal at the transmitter, (b) The eyediagram of the received signal after 50 cm of wireless propagation, (c) the power spectral density of the transmit pulses obtained from the electrical spectrum analyzer (gray), the normalized EIRP (blue), vs. the FCC mask (red). (d) the BER performance for back-to-back and 20 km SMF. . . . .	57
3.18	BER performance of the receiver with no equalization (solid blue), and with MMSE equalizer (dashed red) are compared for several wireless distances. . . . .	58
3.19	The schematic diagram of the experimental setup. Gain-switched laser: GSL, SMF: single-mode fiber, polarization controller: PC, erbium-doped fiber amplifier: EDFA, bandpass filter: BPF, photodetector: PD. . . . .	60
3.20	Y-splitter. (a) Lumerical layout (b) power versus position, blue curve is at the input and the green is at the output. . . . .	61
3.21	The amplitude of the electric field. (a) symmetric supermode, and (b) the anti-symmetric supermode. . . . .	62
3.22	(a) the effective indices of the symmetric and antisymmetric supermodes, and (b) the difference of the two indices. . . . .	63
3.23	Simulation result for filtering the gain-switched laser with the RTR notch filter. . . . .	65
3.24	The design layout from DW-2000 software. . . . .	65
3.25	(a) picture of the fabricated chip; the portion dedicated to our design is indicated by a red box, (b) a scanning electron microscope (SEM) image of an RTR, and (c) the SEM image of the Y-splitter. . . . .	66
3.26	Simulated (dotted blue) and measured (solid red) transmission response of the RTR. . . . .	67
3.27	The generated UWB waveforms. (a) The time domain waveforms for the filtered and unfiltered branches, and the resulting UWB pulse. (b) The PSD and the calculated EIRP of the UWB pulse. Simulation results match the experiment. . . . .	68

4.1	Commonly used UWB pulses. (a) the Gaussian 5th derivative, (b) the Gaussian monocycle, (c) a highpass filtered gaussian monocycle pulse, and (d) the corresponding spectra with respect to the normalized FCC spectral mask. . . . .	74
4.2	(a) The SkyCross antenna structure, (b) the measured channel frequency response, (c) the effective mask (dotted, green), the normalized EIRP-optimized pulse spectral density (target in dashed red, and measured in solid blue), and (d) the normalized EIRP-optimized pulses in the time domain (target in dashed red, and measured in solid blue). . . . .	76
4.3	(a) the circular monopole antenna, (b) the measured channel frequency response, (c) the effective mask (dotted, green), the normalized EIRP-optimized pulse spectral density (target in dashed red, and measured in solid blue), and (d) the normalized EIRP-optimized pulses in the time domain (target in dashed red, and measured in solid blue). . . . .	77
4.4	(a) the monopole antenna with two steps, (b) the measured channel frequency response, (c) the effective mask (dotted, green), the normalized EIRP-optimized pulse spectral density (target in dashed red, and measured in solid blue), and (d) the normalized EIRP-optimized pulses in the time domain (target in dashed red, and measured in solid blue). . .	79
4.5	The schematic diagram of the arbitrary UWB waveform generator. GSL: gain switched laser, SMF: Single mode fiber, BPD: balanced photodetector, FBG: fiber Bragg grating, HE: Heating element, [3]. . . . .	80
4.6	The EIRP-optimized pulse (solid, blue) and the Gaussian 5 <sup>th</sup> order derivative (dotted, red) (3), and the Gaussian monocycle pulse (dashed, green); for (a) the SkyCross, (b) the circular monopole, and (c) the monopole antenna with two steps. . . . .	81
4.7	BER simulations; (a) the AWGN channel, (b) average over 52 LOS indoor multipath UWB channels. . . . .	84
5.1	(a) The target UWB waveform (dotted line) and the generated pulse (solid line), (b) The spectral density of the generated UWB waveform under the FCC mask. . . . .	89
5.2	The schematic diagram of the UWB transmitter and receiver systems. GSL: gain switched laser, PC: polarization controller, MZM: Mach-Zehnder modulator, DL: delay line, ATT: attenuator, PD: photodetector, EBG: electromagnetic bandgap, LO: local oscillator, BERT: bit-error-rate tester. .	90

5.3	Characterization of the EBG filter. (a) The target frequency response of the filter, the measured response, and the response of the filter when used with the circulator, (b) the impulse response of the EBG compared to the ideal matched filter impulse response. Amplitude values are normalized.	91
5.4	The normalized output waveform of the matched filter. The measurement is in good agreement with the theory. . . . .	92
5.5	(a) The output waveform of the matched filter for a bit sequence of [1 0 0 1 1 1 0 0 1], (b) the output of the direct conversion receiver for the same bit sequence. . . . .	94
5.6	The measured BER curves for the matched filter and the direct conversion receivers. . . . .	94
5.7	(a) LOS impulse response measurement (b) NLOS impulse response measurement. . . . .	96
5.8	The system model. . . . .	98
5.9	BER simulations of OOK UWB signals in LOS multipath channel conditions; (a) symbol detection, and (b) the VA versus the DFE. . . . .	102
5.10	BER simulations of BPSK UWB signals in LOS multipath channel conditions; (a) symbol detection, and (b) the VA versus the DFE. . . . .	104
5.11	BER simulations of BPSK UWB signals in NLOS multipath channel conditions. . . . .	105
5.12	The fault percentage of NLOS UWB signal detection using a DFE with 21 taps. . . . .	106

# List of Tables

3.1	Link budget . . . . .	43
3.2	Design Parameters . . . . .	64
4.1	Relative power efficiency of antennas under study; Ant. 1: the SkyCross, Ant. 2: the circular monopole, and Ant. 3: the monopole antenna with two steps. . . . .	82
5.1	Channel parameters from <a href="#">[4]</a> . . . . .	97



# Acronyms and Abbreviations

<i>ADC</i>	Analog-to-digital convertor.....	22
<i>ASE</i>	amplified spontaneous emission .....	36
<i>ATT</i>	attenuator .....	15
<i>AWGN</i>	additive white Gaussian noise .....	24
<i>BER</i>	Bit-error-rate .....	4
<i>BPD</i>	balanced photodetector .....	15
<i>BPF</i>	bandpass filter .....	38
<i>BPSK</i>	binary Phase shift-keying.....	3
<i>CFBG</i>	chirped fiber Bragg grating.....	79
<i>CMOS</i>	Complementary metal-oxide-semiconductor .....	13
<i>CW</i>	continuous wave .....	35
<i>DFB</i>	distributed feedback .....	35
<i>DFE</i>	decision feedback equalizer .....	4
<i>DL</i>	delay line .....	15
<i>DPSK</i>	differential PSK.....	24
<i>E/O</i>	electrical to optical conversion .....	13
<i>EBG</i>	electromagnetic bandgap.....	88
<i>ED</i>	energy detector .....	23
<i>EDFA</i>	erbium-doped fiber amplifier .....	36

<i>EIRP</i> equivalent isotropically radiated power .....	1
<i>FBG</i> fiber Bragg grating .....	2
<i>FCC</i> Federal Communications Commission .....	1
<i>FEC</i> forward error correction .....	34
<i>FIR</i> finite impulse response .....	72
<i>FSR</i> free spectral range .....	66
<i>FWHM</i> full-width half-maximum .....	35
<i>GA</i> genetic algorithm .....	73
<i>GSL</i> gain-switched laser .....	16
<i>GVD</i> group velocity dispersion .....	64
<i>HDTV</i> high definition television .....	1
<i>HE</i> heating element .....	79
<i>HPF</i> highpass filter .....	70
<i>IR – UWB</i> impulse radio UWB .....	10
<i>ISI</i> intersymbol interference .....	18
<i>LAN</i> local area network .....	1
<i>LNA</i> low-noise amplifier .....	8
<i>LO</i> local oscillator .....	12
<i>LOS</i> line-of-sight .....	18
<i>LPF</i> lowpass filter .....	51
<i>MB – UWB</i> multiband UWB .....	10
<i>MLSE</i> maximum likelihood sequence estimator .....	100
<i>MMSE</i> minimum-mean-square-error .....	48
<i>MPC</i> multipath component .....	19

<i>MZM</i>	Mach-Zehnder modulator .....	34
<i>NF</i>	noise figure .....	43
<i>NLOS</i>	non-line-of-sight .....	18
<i>NRZ</i>	non-return-to-zero .....	55
<i>OFDM</i>	orthogonal frequency-division multiplexing .....	34
<i>OOK</i>	on-off keying .....	9
<i>PA</i>	power amplifier .....	31
<i>PAM</i>	pulse amplitude modulation .....	9
<i>PC</i>	polarization controller .....	36
<i>PCB</i>	Printed circuit board .....	21
<i>PE</i>	power efficiency .....	41
<i>PLL</i>	phase-locked-loop .....	37
<i>PON</i>	passive optical network .....	3
<i>PPM</i>	pulse position modulation .....	9
<i>PRBS</i>	pseudorandom bit sequence .....	43
<i>PSD</i>	power spectral density .....	36
<i>QAM</i>	quadrature amplitude modulation .....	109
<i>QPSK</i>	quadrature Phase Shift Keying .....	109
<i>RF</i>	radio frequency .....	3
<i>RF</i>	radio frequency .....	17
<i>RMS</i>	root mean square .....	19
<i>RTR</i>	race-track ring resonator .....	58
<i>Rx</i>	receiver .....	30
<i>SEM</i>	scanning electron microscope .....	65

<i>SMF</i>	single mode fiber .....	14
<i>SNR</i>	signal-to-noise ratio .....	2
<i>SOI</i>	silicon-on-insulator .....	58
<i>SQP</i>	sequential quadratic program .....	71
<i>TDMA</i>	time-division multiple access .....	16
<i>TR</i>	transmitted reference .....	24
<i>Tx</i>	transmitter .....	30
<i>UMTS</i>	universal mobile telecommunication system .....	7
<i>UV</i>	ultraviolet .....	36
<i>UWB</i>	ultra-wideband .....	1
<i>VA</i>	Viterbi algorithm .....	4
<i>VNA</i>	vector network analyzer .....	31
<i>VOA</i>	variable optical attenuator .....	50
<i>WDM</i>	wavelength-division-multiplexed .....	3
<i>WPAN</i>	Wireless Personal Area Networking .....	9

# Chapter 1

## Introduction

### 1.1 Motivation

Today, wireless communications is the fastest growing segment of the communication industry. Cellular phones and the Internet have rapidly become an essential part of our everyday life. The popularity of streaming videos over the Internet has caused a growth in bandwidth demand. Nowadays, the popularity of high definition television (HDTV) is particularly pushing up bandwidth demand. The Internet is typically brought to homes by cables with migration to optical fiber considered for the future. Once in the home, people seek the convenience of wireless access. There are usually other personal devices at home, such as printers, cameras, and DVD players. The communication between the computer and these devices is primarily accomplished by cable connections. Wouldn't it be amazing to connect all these devices with no cable at all?

The IEEE 802.11 wireless LAN data rates are not high enough for the mentioned applications. Ultra-wideband (UWB) communications is a research field that promises very high data rate wireless indoor communications. To support deployment of UWB radio, the US Federal Communications Commission (FCC) issued its first report in 2002 [1]. Per this ruling, UWB radio enjoys a huge 7.5 GHz bandwidth, from 3.1 GHz to 10.6 GHz. However, the equivalent isotropically radiated power (EIRP) from a UWB device should be below a spectral mask (Figure 1.1). The radiated power constraints ensure UWB systems do not cause interference with other coexisting narrowband systems. Power limitations make UWB radio short range. Currently, UWB systems have a

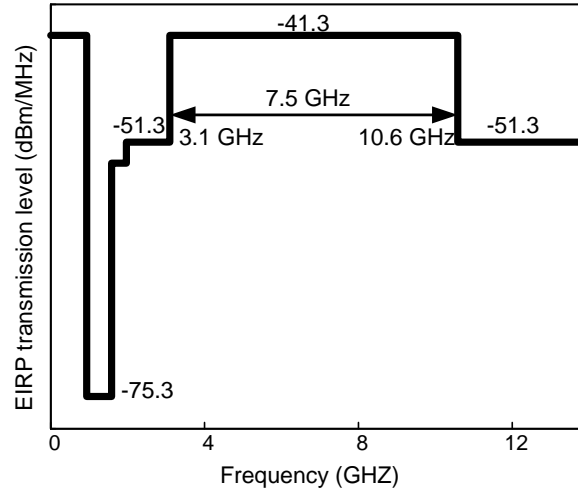


Figure 1.1: FCC spectral masks for indoor and outdoor communication applications [1].

range of a few meters and are limited within a room. This is a major drawback for practical applications of UWB.

To extend the range of UWB communications, pulse shaping techniques that use most of the available power under the FCC spectral mask are essential. Furthermore, fiber transport of UWB signals extend their reach from a few meters to several kilometers. Direct generation of UWB signals in the optical domain attracted a growing interest in recent years [5–11].

At Laval University, we have previously developed an optical pulse shaping method to precisely generate very efficient UWB pulses that closely respect the FCC spectral mask [11]. Our pulse shaping method is based on spectral shaping of a laser source using a fiber Bragg grating (FBG) .

Although optics is a favorable environment for transport of UWB signals, the ultimate goal is wireless transmission and error free reception. Highly efficient pulses result in a better signal-to-noise ratio (SNR) at the receiver. Better SNR will reduce errors and extend the reach for indoor communication purposes. Nevertheless, an efficient pulse shape does not guarantee the quality of the communication as there are many more challenges to the system. The wireless channel, for example, significantly affects the received signal. Realistic propagation scenarios need to be chosen to correctly model the received signals. The channel information will help us in choosing appropriate transmitter and receiver structures.

## 1.2 Objectives and Major Contributions

We propose three optical solutions for low cost generation of UWB signals. Our solutions are compatible with wavelength-division-multiplexed passive optical network (WDM-PON) distribution. We provide detailed simulation and experimental results of the optical pulse generators, as well as wireless transmission and receiver error performance analysis. We select pulse shaping components that promise future optical on-chip UWB transmitters.

Our first approach is based on using a Mach-Zehnder modulator to upconvert on-off keying (OOK) baseband pulses to the center of the FCC spectral mask. The optical pulses are produced by a gain switched laser. We show good power efficiencies for fiber distances between 15 km and 25 km. The optical fiber can be replaced by an FBG filter to make a compact optical UWB transmitter for applications that do not require fiber, i.e., not PON.

A continuous wave laser, a Mach-Zehnder modulator, and a photodetector are the only optical components we use in our second pulse generator. A combination of data and a sinusoidal signal are used to generate binary phase shift-keying (BPSK) UWB signals at 1.75 Gb/s. BPSK has a lower error rate at a given SNR compared to other binary digital modulation formats.

In the third case, we propose an integrated pulse generation solution; gain-switched laser pulses are spectrally filtered by a silicon micro-ring resonator. Single mode fiber propagation performs the frequency-to-time mapping and balanced photodetection removes the low frequency components of the generated RF signals. OOK UWB pulses generated by this method show good power efficiency.

Many possible transmitter and receiver structures exist, motivating us to develop a MATLAB simulator to investigate the performance of candidate solutions. The simulator uses multipath channels measured by Intel Corporation [4]. By exploiting the properties of the channel, it is possible to design receiver algorithms that achieve good performance. Our simulations investigate the significance of pulse shaping in improvement of bit error rate under multipath interference. We simulate a linear filter matched to the transmit waveform and also an energy detector.

In order to highlight the effect of pulse shaping and show the capability of our technique under different channel circumstances, we test the system with different UWB antennas. We seek antennas that not only function over the whole UWB bandwidth, but also show high omni-directionality in all the bandwidth. After fabrication of the antennas and designing the corresponding efficient pulses, the versatility of our technique is investigated experimentally.

To compensate the severe intersymbol interference at gigabit rates, we investigate the Viterbi algorithm (VA) with a limited number of states and the decision feedback equalizer (DFE). We examine the required number of states in the VA, and the number of taps in the DFE for reliable Gb/s UWB transmission for Intel channels. Bit-error-rate (BER) simulations confirm that equalization considerably improves the performance compared to symbol detection.

Implementation of a matched filter is a challenging task in RF. We evaluate experimentally a matched filter synthesized and fabricated in microstrip technology. We show that the output of the microstrip matched filter is close to an ideal matched filter response. BER simulations quantify the superior performance of the matched filter compared to a direct conversion receiver.

### 1.3 Structure of the thesis

Following the introduction in Chapter 1, which summarizes the motivation and the objectives of this research, Chapter 2 presents review of complete UWB systems. After some basic concepts about UWB communications, pulse shaping methods are discussed with emphasis on the optical domain techniques. We present UWB channel models and also briefly review UWB antenna properties. This chapter ends with a look at UWB receivers.

In Chapter 3 we present three optical UWB pulse generation methods. The first two methods use a Mach-Zehnder modulator to upconvert signals from baseband to the center of the FCC mask. The third method is an integrated solution based on a micro-ring filter in silicon.

In Chapter 4 we describe the fabrication and characterization of three UWB anten-



nas. We show the antenna impulse response can be used to improve the UWB pulse design. We simulate the effect of pulse shaping in multipath channels. BER curves are presented for various pulse shapes.

Equalization of UWB signals in multipath channel is discussed in Chapter 5. We compare the Viterbi algorithm with the decision feedback equalizer for a linear receiver. The linear receiver examined is fabricated as an electromagnetic bandgap structure. We characterize the linear filter and also compare its BER performance with a direct conversion receiver.

# Chapter 2

## UWB communication systems

Connectivity for everyone and everything at any place and any time is the vision of wireless systems beyond the third generation. Short-range wireless technology will play a key role in scenarios of ubiquitous communications over different types of links [12]. Novel devices based on ultra-wideband radio technology have the potential to provide solutions for many of today's problems in the area of spectrum management and radio system engineering.

This chapter is dedicated to a literature review of UWB systems. In section 2.1, basic UWB radio concepts are presented. Subsequently, in Section 2.2, we review UWB pulse shaping methods in both the electrical domain and in the optical domain, the latter in more detail. In Section 2.3, we present multipath channel models and channel measurements available for UWB. In Section 2.4, the main characteristics of UWB antennas are presented. Four UWB antenna designs are discussed in detail. In Section 2.5, we investigate UWB receiver structures. Possible modulation schemes are presented for each structure.

### 2.1 UWB basics

UWB technology has existed since the 1980s. It mainly has been used for radar applications because of the wideband nature of the signal that results in very accurate timing information. In the early days UWB was referred to as impulse radio, where

an extremely short pulse with no carrier was used instead of modulating a sinusoid to transmit information. These sub-nanosecond pulses occupy several GHz of bandwidth and are transmitted with very low duty cycles. In April 2002, the FCC issued its first report on UWB technology, thereby providing regulations to support deployment of UWB radio systems [1]. These regulations allowed the UWB radios to coexist with already allocated narrowband radio frequency (RF) emissions.

The band allocated to UWB communications is 7.5 GHz wide, by far the largest allocation of bandwidth to any commercial terrestrial system. The FCC UWB rulings allocated 1500 times the spectrum allocation of a single UMTS (universal mobile telecommunication system) license [13]. However, the available power levels are very low. If the entire 7.5 GHz band is optimally utilized, the maximum power available to a transmitter is approximately 0.5 mW. This effectively relegates UWB to indoor, short range, communications for high data rates, or very low data rates for substantial link distances. In principle, trading data rate for link distance can be as simple as increasing the number of pulses used to carry 1 bit. The more pulses per bit, the lower the data rate, and the greater the achievable transmission distance.

UWB devices are intentional radiators under FCC Part 15 Rules. For a radiator to be considered UWB the fractional bandwidth defined as

$$B_f = 2 \frac{f_H - f_L}{f_H + f_L} \quad (2.1)$$

must be at least 0.2. In the formula above,  $f_H$  and  $f_L$  are the higher and lower -10 dB frequencies, respectively. The radiation limits set by the FCC are presented in Figure 1.1 for indoor and outdoor data communication applications. These limitations are expressed in terms of equivalent isotropically radiated power (EIRP). EIRP is the product of the transmit power from the antenna and the antenna gain in a given direction relative to an isotropic antenna. Allowed UWB emission levels are less than or equal to the level allowed for unintentional radiators such as computers and other electronic devices (-41.3 dBm/MHz). Thus, UWB systems can coexist with other narrowband networks; the interference caused by a UWB transmitter can be viewed as a wideband interferer, and it has the effect of raising the noise floor of the narrowband receiver. A benefit to UWB of this low power constraint is preserving battery life. Another benefit of low power is low probability of detection which is a concern for both military and consumer applications. The weak UWB pulses are inherently short range which makes the operation of multiple independent links possible within the same house. The broadband property of the UWB signal makes it resistant to interference because any interfering

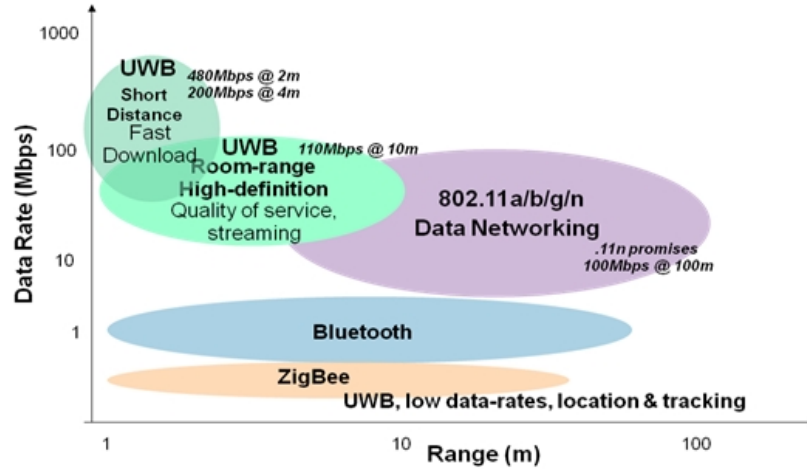


Figure 2.1: WiMedia landscape of UWB compared to Wireless local area networks (WLAN) [2]

signal is likely to affect a small portion of the desired signal spectrum.

UWB can provide very high speed but short distance communication links. Fig. 2.1 shows the WiMedia landscape of UWB services compared to IEEE 802.11 networks [2]. It can be seen that UWB is the fastest in close range while the IEEE 802.11 is more suitable for distances more than 10 m. The spatial capacity, an indicator of data intensity in a transmission medium, is over  $10^6 \frac{\text{bit}}{\text{s.m}^2}$  for UWB. No current commercial system is capable of reaching a spatial capacity as high as that of a UWB system. This can be explained by the Shannon channel capacity theorem [14]. The upper bound on the capacity of a channel grows linearly with the available bandwidth. Thus, the UWB systems occupying several GHz of bandwidth show great potential for the future high capacity wireless networks.

Some important issues attributable to UWB are discussed here.

a) Antennas: Antennas have a filtering effect on the UWB pulse. Good impedance matching over the entire UWB bandwidth is desired to reduce reflection losses from the antennas. The impulse response of the antenna changes with angles in azimuth and elevation. Therefore, the transmitted pulse is differently distorted at every angle.

b) Low noise amplifiers (LNAs): Design of amplifiers is another challenge for UWB applications. Due to the low power and wideband nature of the UWB signal, very low noise and wideband amplifiers are essential at the receiver side.

c) Modulation: For pulsed UWB systems, the widely used modulation schemes are pulse amplitude modulation (PAM), on-off keying (OOK), and pulse position modulation (PPM). The OOK scheme results in energy detection receivers of lower complexity, whereas the PPM shows better error performance but lower bit rates.

d) Multipath: In the indoor environment the signal bounces off objects located between the transmitter and receiver creating multipath reflections. If the delay spread of the echoes is smaller than the pulse width, the echoes can combine destructively leading to multipath fading. However, for an indoor UWB system with a range of 10 m, the delay spread is typically several nanoseconds, significantly more than a typical UWB signal pulse width. This makes UWB resistant to multipath interference. To maximize the received energy, one can use a RAKE receiver to combine the signals coming over resolvable propagation paths. However, combining many multipath components increases the complexity of the receiver.

### 2.1.1 UWB applications

Among recent applications of UWB are the following.

1. Cable replacement: Today, most computer and consumer electronic devices (everything from a digital camcorder and DVD player to a mobile PC and a high-definition TV (HDTV)) require wires to record, play or exchange data. UWB will eliminate these wires, allowing people to "unwire" their lives in new and unexpected ways [15]. A mobile computer user could wirelessly connect to a digital projector in a conference room. Digital pictures could be transferred to a photo print kiosk for instant printing without the need of a cable. An office worker could put a mobile PC on a desk and instantly be connected to a printer or a scanner.
2. Wireless Personal Area Networking (WPAN): A high speed wireless UWB link can connect cell phones, laptops, cameras, MP3 players. This technology provides much higher data rates than Bluetooth or 802.11. With UWB a portable MP3 player could stream audio to high-quality surround-sound speakers anywhere in the room.
3. Vehicle collision avoidance: UWB can provide enough resolution to distinguish cars, people, and poles on or near the road. This information can be used to

alert the driver and prevent collisions. UWB radar has the resolution to sense road conditions (i.e., potholes, bumps, and gravel vs. pavement) and provide information to dynamically adjust suspension, braking, and other drive systems.

4. Radar: UWB can provide centimeter accuracy in ranging because of its high time resolution. Improved object identification (greater resolution) is achieved because the received signal carries the information not only about the target as a whole, but also about its separate elements.
5. Other applications of UWB are public safety systems including motion detection applications, RF tag for personal and asset tracking, medical monitoring and so forth.

Our proposed optical UWB pulse generation techniques target applications 1 and 2. These applications require high speed wireless communications.

### 2.1.2 Impulse radio vs. multiband UWB

UWB systems can be either impulse radio (IR-UWB) or multiband (MB-UWB). The former method uses pulses that cover the whole spectral mask (Fig. 2.2a). The IR-UWB has the potential to alleviate the range problem by effectively utilizing most of the permitted power. In IR-UWB, pulse shaping techniques that use most of the available power are essential in extending the range of UWB pulses.

Sending very short pulses to cover all the bandwidth is not the only form of UWB communication. UWB does not have to be impulse or carrier-less. Multiband UWB (MB-UWB) provides a method where the FCC approved 7.5 GHz UWB bandwidth is split into several smaller frequency bands, each having a minimum of 500 MHz bandwidth (Fig. 2.2b). The signals do not interfere with each other because they operate at different frequencies. Each signal can be modulated using standard modulation techniques enabling very high bit rates.

There are several advantages associated with MB-UWB. Data rates are scalable in MB-UWB, more bands allow higher data rates while low data rates are accommodated in fewer bands. This also means scalable power consumption [16]. In MB-UWB the information can be processed over much smaller bandwidth, thereby reducing overall

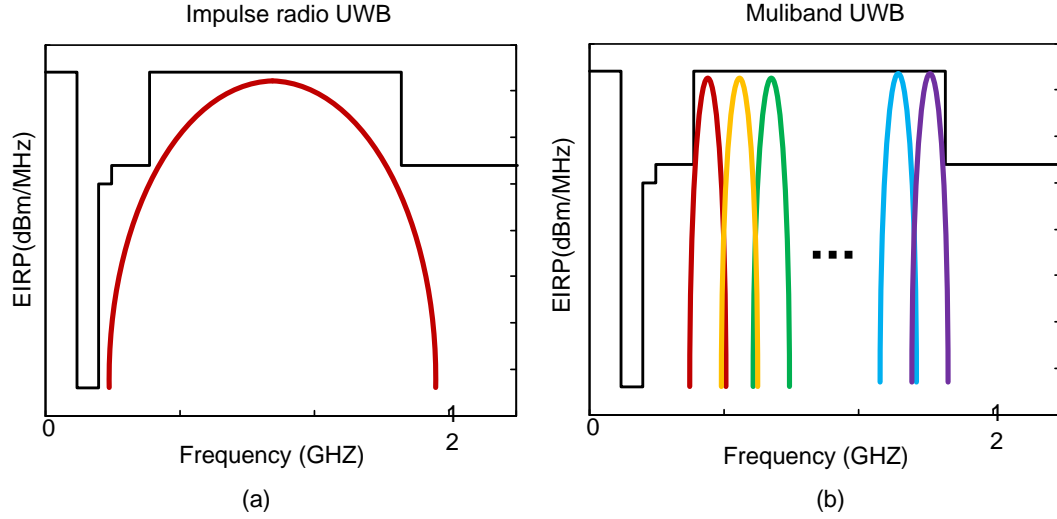


Figure 2.2: (a) impulse radio (IR-UWB), and (b) multiband (MB-UWB).

design complexity, as well as improving spectral flexibility and worldwide compliance. Multiband UWB facilitates coexistence with legacy systems and worldwide deployment by enabling some sub-bands to be turned off in order to avoid interference and comply with different regulatory requirements. In addition, multiband systems provide another dimension for multiple access via frequency division. Different users can use different pulses for multiple access, and frequency hopping can also be easily implemented by switching among those [17]. The major drawback of the MB-UWB systems is their shorter range compared to IR-UWB systems as each band accommodates only a portion of the permitted total power by the FCC mask. Thus, the IR-UWB is more suitable for extending the reach of UWB communication.

## 2.2 UWB pulse generation techniques

In UWB systems the conventional analog waveform, representing a message symbol, is a simple pulse that in general is directly radiated. These short pulses have typical durations in the picosecond range, and thus bandwidths of over 1 GHz. In the literature, the most common UWB pulses are Gaussian monocycles. Although traditionally employed for UWB systems, these shapes poorly exploit the permissible power under the FCC mask. The strict power limitations imposed by the FCC spectral mask necessitate spectral pulse shaping: designing spectrally efficient pulses that eke out most of the

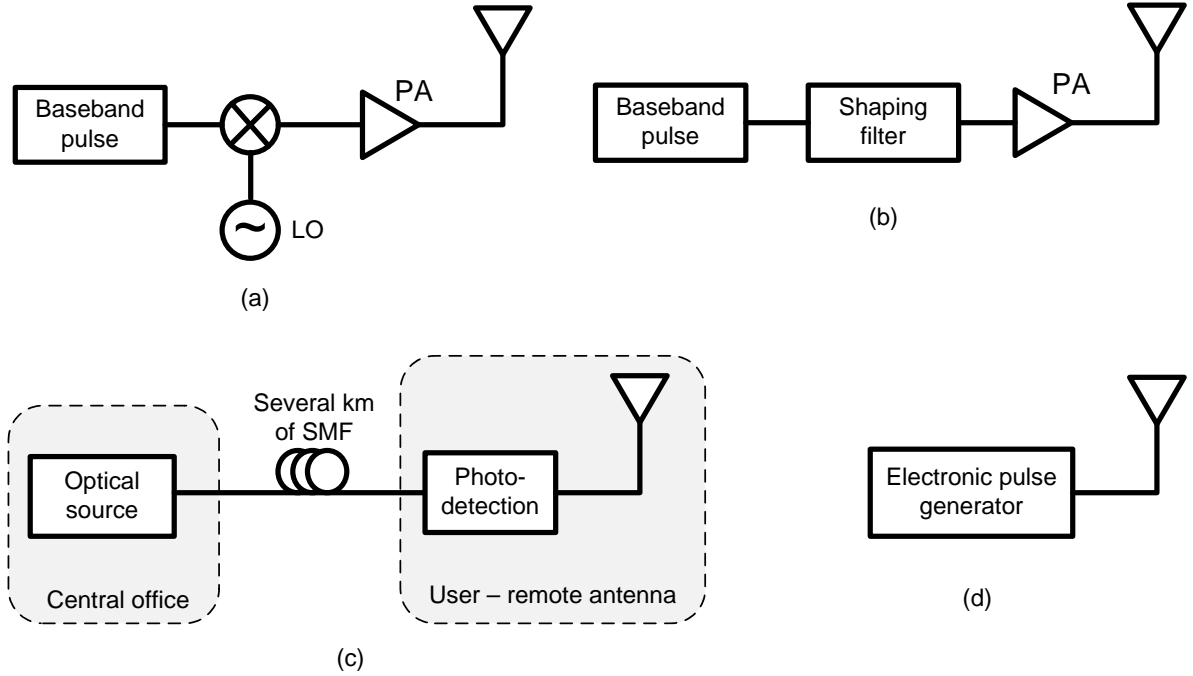


Figure 2.3: UWB pulse generation techniques. (a) upconversion of baseband pulses, (b) shaping baseband pulses using a filter, (c) optical generation/transport of UWB signals, and (d) electrical UWB pulse generation.

power available under the FCC mask. As with all communication systems, UWB system performance highly depends on the signal to noise (SNR) ratio. Therefore choosing efficient pulses for UWB communication systems is of critical importance.

Fig. 2.3 shows common UWB pulse generation methods. IR-UWB pulses can be generated by either upconversion of baseband pulses by mixing them with a local oscillator (LO), or by direct synthesis of pulses in the UWB frequency band without using an LO [6]. Furthermore, pulses can be generated either in electronics or in optics [5–11]. A brief review of these methods follows. We discuss some of the most popular methods. Our solutions are based in the optical domain and are covered in detail in Chapter 3.

### 2.2.1 Pulse generation in the electrical domain

Although in this thesis we only work with UWB transmitters in the optical domain, we briefly review some electronic generation methods to contrast with optical techniques.



Major advantages of electrical generation of UWB pulses are low-cost, possibility of integration on a single chip and support for various modulation formats. The major drawback is that the range of transmission of electrical UWB signals is very limited. Generating the signal in RF and converting it to the optical domain afterwards increases the range but requires additional electrical to optical (E/O) conversion. Another disadvantage is that the electrical methods normally do not cover all of the available bandwidth, which degrades the spectral utilization. Furthermore, typical imprecision of the generated pulses leads to violation of the FCC spectral mask. Although recent electronic methods are quite efficient vis-à-vis the FCC spectral mask, they are not appropriate for long distance distribution of the radio signals. To avoid further electrical to optical conversions, optical generation of IR-UWB pulses is highly desirable. Optical fiber distribution of UWB signals extends the reach of such systems to several kilometers.

Several methods have been proposed for electrical generation of UWB impulses. As shown in Fig. 2.3a upconversion of baseband pulses is one way of generating UWB waveforms. In a simple method, a sinusoidal monocycle pulse was generated by gating a sinusoidal signal with a rectangular signal in [18]. This scheme supported BPSK and PPM modulation formats and resulted in pulses with duration of 250 ps. The spectra of the pulses, however, did not respect the FCC spectral mask. In [6], UWB sub-bands were generated in a BiCMOS process. Baseband signals were formed and converted to upper frequencies by mixing with an LO. The chip also had a bandpass filter to reject out-of-band frequencies and a power amplifier before the antenna. The pulses had a center frequency of 5.355 GHz, a 10-dB bandwidth of 550 MHz and data rate of 50 Mb/s with BPSK modulation format.

UWB waveforms can be directly generated without using an LO by filtering baseband pulses (Fig. 2.3b). Generation of a Gaussian fifth order derivative pulse was achieved by a CMOS chip, based on combining square pulses through four delay and gain stages [19]. This design uses an input square pulse and a pulse-combinatorial method to generate an output pulse composed of six individual impulses, each independently adjustable in both amplitude and delay. The delays are adjusted by passing the square pulse through series and shunt delay stages. A bank of amplifiers provides the amplitude weights for each pulse. Each delay stage or gain amplifier is controlled independently by supplying control voltages, resulting in great flexibility. This method can produce pulses respecting the FCC UWB indoor frequency mask. Simulation results with data rates of up to 2 Gb/s and several types of data modulation are demonstrated

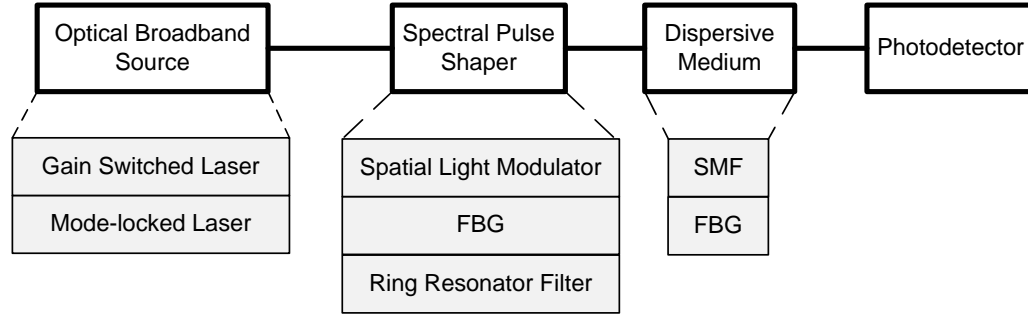


Figure 2.4: Schematic diagram of pulse generation by spectral pulse shaping. SMF: single-mode fiber, FBG: fiber Bragg grating.

with this configuration. The advantages of this method are the use of low cost CMOS technology, the programmability and the precision in generation of FCC-compliant UWB pulses. Similarly, BPSK Gaussian fifth order derivative generation was reported in [20] using the  $0.18\text{-}\mu\text{m}$  CMOS technology.

### 2.2.2 Pulse generation in the optical domain

There are numerous optical UWB pulse generator architectures; most focus on the widely adopted Gaussian, monocycle and doublet pulses. One of the most promising methods is spectral shaping and frequency-to-time mapping in a dispersive device. [10, 11, 21, 22]. Spectral shaping allows for precise shaping and also tunability of the generated signals. Fig. 2.4 illustrates the main concept of this technique. A broadband optical source provides adequate spectral width in the optical domain. It can be either a mode-locked laser or a gain-switched laser (GSL). GSL results in limited optical bandwidth but is a simpler source compared to a mode-locked laser. Subsequently, spectral pulse shaping is performed using an optical filter. Spatial light modulator, fiber Bragg grating or ring resonator (3.4) can be used for pulse shaping. Frequency-to-time mapping is needed to transfer the tailored spectral response to the time domain. Single mode fiber (SMF) or a chirped FBG in reflection can be used as dispersive devices for frequency-to-time mapping. UWB pulses are obtained by optical to electrical conversion in a photodetector.

An early work on spectral pulse shaping was [10] in which Jalali *et al.* showed an RF-photonics arbitrary waveform generator. A wide band optical pulse was spectrally

shaped by a spatial light modulator after being diffracted by a diffraction grating. The resulting shape in spectrum was mapped in time domain by frequency-to-time conversion using a certain length of SMF. The total amount of dispersion determines the pulse duration. The time domain pulse is generated by photodetection of the optical pulse. Although this arbitrary waveform generator offers tremendous flexibility, and can generate the desired UWB pulse, it cannot be used in many applications due to its large size and high optical loss.

To perform high precision pulse shaping with a compact setup an optical pulse shaping technique based on FBGs [11] was proposed at Laval University.<sup>1</sup> This approach resulted in UWB pulses that are FCC-compliant and maximize the transmitted power. We found efficient UWB pulses by a method described in [17]. This method is based on linearly combining Gaussian monocycle pulses to form an UWB waveform. Optimal UWB waveforms that closely match the spectral mask are obtained by an optimization procedure which finds the weights of combined Gaussian monocycles.

The setup is shown in Fig. 2.5. A mode-locked fiber laser or a gain-switched laser with large bandwidth is used as a coherent broadband source. FBG1 is used to flatten the mode-locked source spectrum over the desired bandwidth. The optical signal is then divided into two arms. In the first arm, we use a second chirped grating, FBG2, with a complex apodization profile optimized to imprint the desired pulse shape on the spectrum of the source. The spectral pulse shaper in this design is an FBG in transmission with a transfer function proportional to the desired pulse. An isolator was used to prevent back and forth reflections between the two FBGs. In the second arm, the optical delay line (DL) and the variable attenuator (ATT) are used to balance the amplitude and the delay of the two arms. We use an appropriate length of SMF as the dispersive medium to generate the total required dispersion for the frequency-to-time conversion.

The particular form of our embodiment is heavily influenced by the requirement to remove the undesired superimposed rectangular pulses imprinted on the desired pulse during conversion to the time domain. The unwanted additive rectangular pulse superimposed on the desired pulse shape lead to strong, unwanted spectral components that cannot be removed by a dc-block. We use a balanced photodetector (BPD) to completely remove unwanted low frequency components, as seen in Fig. 2.5.

---

<sup>1</sup>This work was done by a group of researchers at Laval University led by M. Abtahi. I contributed to this project as a Master's student.

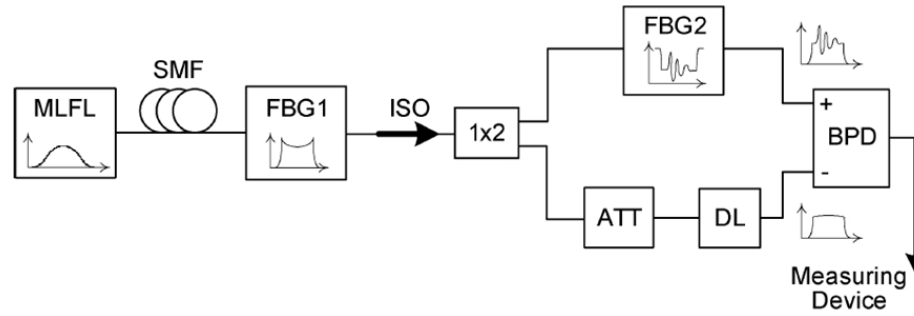


Figure 2.5: Block diagram of the UWB waveform generator.

We use a programmable variation of this pulse shaper to generate several UWB pulses and compare their resulting EIRP for three antennas in Chapter 4.

Among other existing optical UWB signal generation methods, we can mention the phase-modulation-to-intensity modulation conversion [23], microwave delay line filter to differentiate Gaussian pulse [24], monocycle pulse generation based on cross-gain modulation in a semiconductor optical amplifier [25].

An intensity modulator was biased at its nonlinear regime to generate a Gaussian doublet pulse [8]. A Gaussian pulse is applied to the modulator and the nonlinear transfer function of the modulator inverts a part of the Gaussian to shape a doublet. In another work, self-phase modulation in highly nonlinear fiber was used to spectrally broaden Gaussian pulses. Gaussian doublet pulses were generated by optical balanced detection [26]. A gain-switched laser (GSL) was used to generate Gaussian pulses [27, 28]. The pulses were photodetected and shaped in the electrical domain by a UWB bandpass filter. In [9, 29], UWB-over-fiber link compatible with wavelength-division-multiplexed passive optical networks (WDM-PON) was proposed. WDM-PON networks are capable of simultaneously providing end-users with wired and wireless services. The current PON networks are based on time-division multiple access (TDMA) but the networks are expected to evolve to WDM-PON to accommodate future traffic growth [30].

In Chapter 3, we propose three new optical pulse generation methods. These methods are developed with the intention of exploiting them in future passive optical networks for transport of UWB signals (Fig. 2.6). In a WDM-PON optical pulses are generated by laser sources at a central office. Optical intensity modulators add the

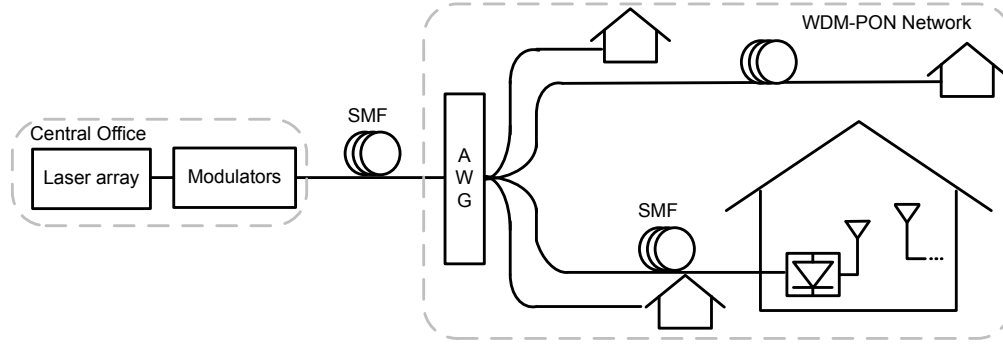


Figure 2.6: A WDM-PON network transporting UWB radio signals.

data on the optical intensity. Single-mode fiber links the central office with the end users. An arrayed waveguide grating is used to direct the data on each wavelength to its corresponding user. At the user side, we can have some optical processing before photodetection. An antenna after photodetection transmits wirelessly the UWB signals for high speed indoors communications. We briefly discuss our three novel UWB pulse generation techniques here. Chapter 3 gathers full description, simulation results and measurement data about these methods.

Our first approach, presented in Section 3.2, is based on using a Mach-Zehnder modulator to upconvert OOK baseband pulses to the center of the FCC spectral mask. We show good power efficiencies for fiber distribution distances between 15 km and 25 km.

Our second method also exploits upconversion but results in BPSK UWB pulses. A continuous wave laser, a Mach-Zehnder modulator, and a photodetector are the only optical components we use in this method. A combination of data and a sinusoidal signal are used to generate BPSK UWB signals at 1.75 Gb/s.

Our third approach is an integrated pulse generation solution where laser pulses are spectrally filtered by a silicon micro-ring resonator. Single mode fiber propagation performs the frequency-to-time mapping and balanced photodetection removes the low frequency components of the generated RF signals. OOK UWB pulses generated by this method show very good power efficiency.

Generation of UWB signals, either by optical means or in electronics, constitutes only half of a communications system, the other half being the receiver. Wireless

channel is a challenging environment sitting in between transmitter and receiver. The multipath UWB channel completely changes the waveforms by introducing intersymbol interference (ISI) and distortion. A good knowledge of the channel is essential in UWB system design. UWB channels are discussed in the next section.

## 2.3 UWB channel models and measurements

Having a good knowledge of the wireless channel is essential in designing receiver structures. Receivers can achieve better performances by having information from the channel. The channel induces some power loss on the signal, as well as multipath. In this section, we start by a path loss model for UWB propagation. We then discuss the multipath channel.

### 2.3.1 Path loss model

Electromagnetic waves radiated from an antenna are attenuated as they propagate. This path loss needs to be taken into account in the calculation of the link budget to ensure enough power is available at the transmitter. The propagation path loss in free space can be modeled by the Friis transmission formula [31]

$$\frac{P_R(f)}{P_T(f)} = G_T(f) G_R(f) \left( \frac{c}{4\pi df} \right)^2 \quad (2.2)$$

where  $P_R(f)$  is the received power density,  $P_T(f)$  is the transmitted power density,  $G_T(f)$  is the transmit antenna gain,  $G_R(f)$  is the receive antenna gain,  $c$  is the speed of light,  $d$  is the far field radial distance between the transmitter and the receiver and  $f$  is the frequency of operation. This model assumes a line-of-sight (LOS) link between the transmitter and the receiver, and no multipath components. In the presence of multipath, statistical path loss models are appropriate [32]. An adjustment to the Friis equation is to replace the quadratic term in 2.2 with a variable exponent that depends on the environment in which the system operates; it can be less than one in corridors with LOS, and as high as seven in severely blocked non-line-of-sight (NLOS) propagation. Typical values for LOS are on the order of 1.5, and for NLOS on the order on 3-4 [32].

### 2.3.2 Multipath model

Multipath means that the signal propagating in a wireless channel gets to the receiver via various paths. Multipath occurs due to three basic propagation mechanisms, namely, reflection, diffraction, and scattering of the transmitted signal. Depending on the path a multipath component (MPC) goes through, it has a certain delay and attenuation. Therefore, the channel impulse response can be approximately modeled as,

$$h(\tau) = \sum_{i=1}^N a_i \delta(\tau - \tau_i) \quad (2.3)$$

where  $N$  is the number of MPCs,  $a_i$  is the amplitude and  $\tau_i$  is the delay of the  $i$ th multipath component. Equation 2.3 assumes each MPC is a dirac delta function. This ignores the distortion of MPCs due to interaction with objects. The MPCs are also distorted by transmitter and receiver antennas. Complex antenna response introduces amplitude and phase changes in MPCs. This distortion depends on the angle the MPC departs or arrives at the antenna and is frequency dependent.

The parameters in (2.3) have been studied extensively, for example in [33]. A brief description of these parameters follows.

- Number of multipath components  $N$

$N$  is usually the number of MPCs within a certain loss of the strongest path. Measurement results show that  $N$  depends on the separation distance of the antennas and variance of  $N$  increases for large separations.

- The delay spread

The delay spread is a metric of how much the signal is diluted in time. It is usually expressed in root mean square (RMS) value [13]. The delay spread increases as the separation of the antennas increases. Measurements show a wide variation of the RMS delay spread for different environments and antenna separations. As a result the multipath model should consider a range of multipath delay spreads. The delay spread suggests if ISI would occur in the signal depending on the bit rate. If the RMS delay is much smaller than the symbol duration no ISI occurs. This is usually not the case for high bit rate systems.

- The amplitude distribution

Measurement results show that an exponentially (linear in dB) decaying multipath

intensity profile is a reasonable model [13]. The RMS delay spread is the standard deviation of the amplitude distribution. The delay spread can be utilized to find the decay factor of the amplitude distribution.

Intel corporation performed UWB channel measurements in a residential environment in 2002 [4]. The measurements were collected for both LOS and NLOS channels from 2 to 8 GHz in a typical house for numerous antenna locations. Based on these measurement results, it was observed that UWB channel shows a clustering effect that is not included in (2.3). Paths arrive in clusters rather than being uniformly spaced in time, partly as a result of the very fine resolution that UWB waveforms provide. The IEEE UWB channel model, assisted by the Intel measurements, is based on this clustering effect. In this thesis, we use Intel channel measurements in our simulations. Further information follows in Chapter 4.

At data rates where the channel delay spread is longer than the symbol period, significant ISI occurs at the receiver. The ISI is a limiting factor to increasing of data rate. Equalizers compensate for the ISI induced by the channel. In Chapter 5 we investigate equalization techniques for the Intel channel measurements.

## 2.4 UWB antennas

So far we have discussed pulse shaping and channel impulse response as they will affect the received waveform. The antennas also must be taken into account. In recent years, there has been a huge amount of research in UWB antenna design. An effective antenna is a critical part of the overall UWB system design. The following characteristics are desirable for UWB antennas.

- A UWB antenna is required to be capable of transmitting and receiving all frequencies from 3.1 to 10.6 GHz. This implies that the antenna should have a good matching in this band. The principle criterion in design of UWB antennas is the scattering parameter  $S_{11}$ .  $S_{11}$  corresponds to return loss and values lower than -10 dB ensure a good matching in the required bandwidth.
- The antenna is desired to be non-dispersive in order to radiate similar waveforms



in all directions. In this respect, small antennas are preferred over large scale antennas, e.g. log-periodic antenna.

- UWB indoor devices can be placed anywhere in the house. This means that the antennas should operate in all directions. Omni-directional antennas have this property. These antennas are small but they have low gain. A low gain is not a drawback for the transmitter antenna, as the permissible power is limited by the FCC regulations. However, at the receiver, more gain will increase the performance of the receiver. There is a trade off between the antenna omni-directionality and the gain. Moreover, the antenna should be omni-directional over all the UWB bandwidth. Therefore, another design criteria for UWB antennas is the stability of the radiation pattern for all frequencies.
- A UWB antenna is required to achieve good time domain characteristics. The UWB antenna acts like a band-pass filter and has significant impact on the input signal. As a result, a good time domain performance, i.e. minimum pulse distortion in the received waveform, is a primary concern of a suitable UWB antenna. If waveform distortion occurs in a predictable fashion it may be possible to compensate for it.
- Practical applications require the antenna to be very small and light weight.

Printed circuit board (PCB) antennas show most of the mentioned properties and are good candidates for UWB applications. In recent years, various designs have been proposed for microstrip monopole and slot type antennas. Most of the research papers present simulated and measured  $S_{11}$  and radiation patterns to characterize their antennas. In Chapter 4, we fabricate and characterize these antennas in order to investigate their effect on different UWB waveform transmission.

Given the power restrictions of UWB, the use of multiple antennas at the receiver could be a possible approach to obtain an array gain that improves the SNR at the receiver. The FCC mask limits the transmit power. Thus, if multiple transmit antennas are used, each should emit less power to respect the total power radiation limit. However, antenna arrays at the receiver end can provide improved gain via beam steering or diversity combining. In order to achieve diversity gain from multiple antennas, the channels should be uncorrelated. Measurements show that a 4-6 inch antenna separation gives reasonable channel decorrelation [4].

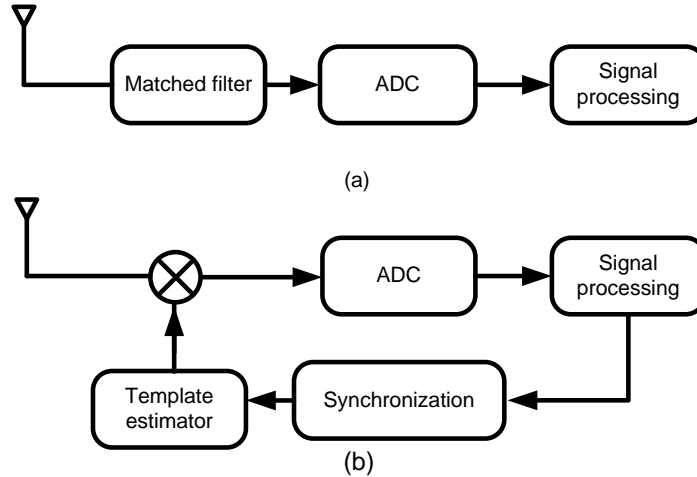


Figure 2.7: Coherent receivers: The matched filter receiver (a), and the correlation receiver (b). ADC: analog-to-digital convertor.

## 2.5 UWB receivers

Receivers can be classified as coherent or noncoherent, depending on whether they exploit the absolute phase of the received signal or not. The large bandwidth of UWB makes the implementation of conventional optimum receivers extremely complex. Noncoherent receivers, though suboptimal, are usually considered more feasible for UWB applications. Furthermore, because of intersymbol interference at high bit rates caused by multipath equalization techniques need to be investigated for UWB reception.

### 2.5.1 Coherent UWB receivers

Coherent receivers offer better performance but are extremely complex for implementation in UWB systems. The coherent receiver, either in the form of a matched filter or a correlation receiver, needs to digitize the signal (Figure 2.7). A fully digital receiver needs to sample the signal at the Nyquist rate which is about 20 GHz for UWB. Analog-to-digital convertors (ADCs) working at this rate are very expensive. Using parallel ADCs adds to the complexity of the system. In Chapter 5 we propose using an electromagnetic bandgap structure as a linear filter matched to the transmit pulse shape. By doing the filtering in the hardware, we can take the burden off the ADC by requiring lower speeds.

Because of the high resolution of UWB pulses, synchronization algorithms are very complicated. Furthermore, the receiver signal is a summation of many multipath components. A rake receiver will need a large number of fingers to capture most of the power, and rapidly becomes too complex to implement. Channel estimation to find the amplitude and delay of each path makes coherent receivers even more complicated.

Due to all these complications, UWB noncoherent receivers, discussed next, receive more attention. However, it is well known that a noncoherent receiver does not perform as well as its coherent counterpart in terms of BER performance.

### 2.5.2 Noncoherent UWB receivers

A noncoherent receiver only exploits the amplitude of the received signal. Noncoherent receivers are suboptimal but more feasible for UWB because of their lower complexity. These techniques do not require channel estimation and allow capturing a large amount of the received energy, despite distortions and multipath propagation. Noncoherent receivers are sub-optimal solutions, if compared to coherent receivers, because of the adoption of a noisy signal as a reference waveform for the demodulation process.

The energy detector (ED) is a classical noncoherent receiver (Figure 2.8a). A square-law device computes the signal power and an integrator accumulates this energy at the sampling time. The ED receiver collects the energy from all MPCs within its integration time. A good choice of the integration time improves the receiver performance. The integration window has to be aligned to the signal to capture the symbol energy. However, this synchronization is done at the symbol rate and does not need to be as precise as the synchronization in coherent receivers. The ED receivers typically lose 5 dB or more of SNR compared to optimal receivers [34] but significantly reduce the complexity and sampling requirements. Energy detectors are especially effective in processing lower bit-rate data as long as no significant ISI is present.

ED receivers can work with on-off keying (OOK) and pulse position modulation (PPM) but they can not detect the phase shift keying (PSK) format since they are insensitive to phase change. A bit estimate is made by comparing the received sample to a threshold. In OOK format, the threshold needs to be computed based on the signal and noise levels. It has been shown that optimization of the threshold and the integration interval,  $T$ , significantly improves the receiver BER in multipath channels

[35].

In PPM modulation format, the signal is sent either in the first half or in the second half of the symbol period. The PPM modulated signal can be detected by comparing the energy of the first half of the bit to the energy in the second half (Figure 2.8b). Thus, the decision can be made by a zero threshold, reducing some complexity. PPM modulation, however, has a 3 dB performance degradation compared to OOK for an additive white Gaussian noise (AWGN) channel.

A differential PSK (DPSK) receiver uses a delay element and a multiplier instead of the square-law device of the ED (Figure 2.8c). The data is modulated differentially at the transmitter and the receiver uses two consecutive pulses to detect the phase change between the two pulses. The second pulse serves as a noisy template. The threshold for DPSK receivers can be set to zero.

To avoid the differential scheme necessary to receive DPSK signals, one can use the transmitted reference (TR) scheme. In this format, an unmodulated pulse is sent before every data pulse. The TR scheme has low efficiency because half of the signal energy is not allocated to data. The performance of TR signaling is equivalent to PPM, for an AWGN channel and is 3 dB worse than the DPSK modulation format [34].

In the following chapters of this thesis we exploit various UWB receivers to evaluate the performance of our optical UWB transmitters. In Section 3.2 we compare an energy detector with a linear receiver matched to the transmit pulses. The transmit signal is OOK UWB generated by our novel optical pulse shaper. The received signal is captured by a real time oscilloscope after the multipath channel. Simulation results show that at close range the linear receiver and the energy detector have a similar performance, but the linear receiver outperforms the energy detector after 2 m of wireless propagation.

In Section 3.3 we once again use a linear receiver matched to the transmit pulses to evaluate our optical pulse generator. Because of high intersymbol interference the performance of the receiver deteriorates badly by increasing the wireless distance. Therefore, we use the MMSE equalizer to achieve the FEC threshold for the received BER.

In Section 4.5 we consider the receiver as a linear filter matched to the transmit pulse. Simulation are performed to investigate the advantages of pulse shaping at the receiver for both AWGN channel and Intel multipath channel measurements. Simulation results

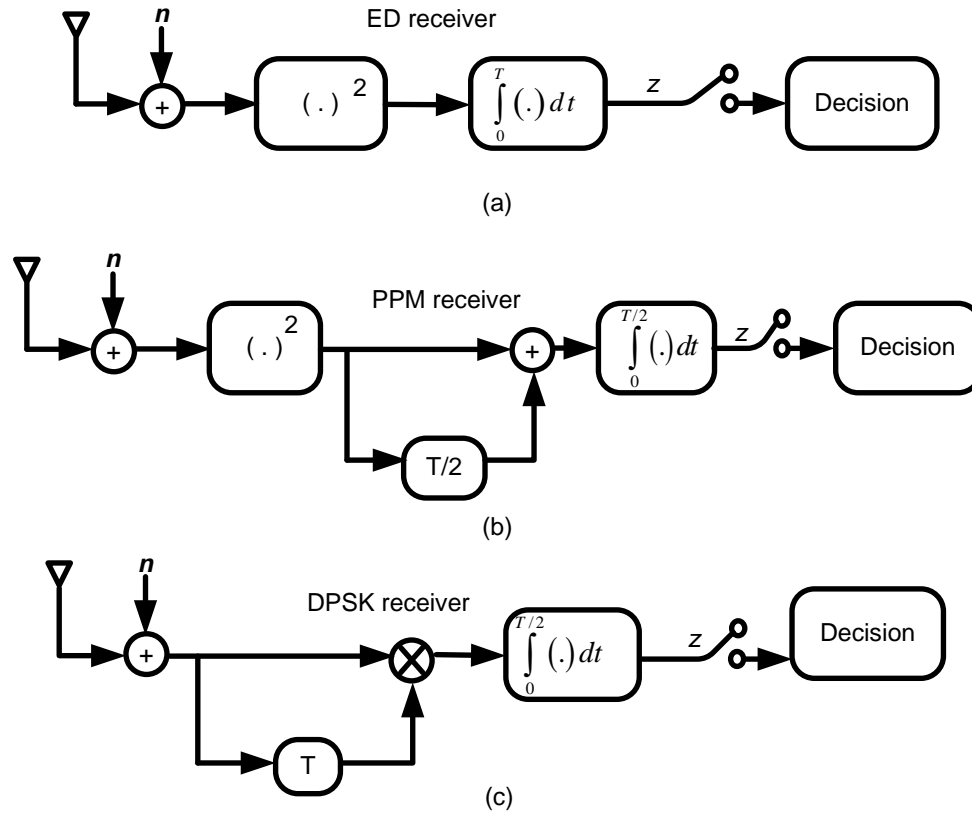


Figure 2.8: Generic noncoherent UWB receiver structures: the energy detection (ED) for OOK receiver(a), the ED receiver for PPM modulation, and the DPSK noncoherent receiver.

confirm that pulse shaping hugely improves the BER performance of the receiver by increasing the received SNR.

Chapter 5 is dedicated to UWB receivers. In Section 5.1 we, in collaboration with McGill University, propose using an electromagnetic bandgap structure as a linear filter matched to the transmit UWB pulse shape. We evaluate experimentally the filter synthesized and fabricated in microstrip technology. BER simulations show the superior performance of the matched filter compared to a direct conversion when the receiver is placed back-to-back with the transmitter.

Finally in Section 5.2 to compensate the severe intersymbol interference at gigabit rates, we investigate the Viterbi algorithm with a limited number of states and the decision feedback equalizer. BER simulations confirm that equalization considerably improves the performance compared to symbol detection.

## 2.6 Conclusion

In this chapter we presented a literature review of a complete UWB system, from transmitter to receiver. The short time duration of UWB makes Gb/s speeds possible but the power limitation of the pulses reduces the propagation distance to a few meters. Optical fiber is good medium for transmission of UWB signals to extend their reach to several kilometers, therefore the interest in optical generation of UWB signals. In the next chapter, we will introduce three novel optical UWB pulse generation methods compatible with PON-WDM. We use simple elements such as a Mach Zehnder modulator or a ring resonator for pulse shaping, allowing for integration in silicon. Two of the proposed methods are based on upconversion and the third method uses a microring resonator for spectral shaping. The EIRP from all three transmitters respects the FCC spectral mask and the pulses possess reasonable power efficiencies.

We use the programmable optical UWB pulse shaping setup based on FBGs to generate high precision FCC-compliant UWB pulses in Chapter 4. The high power efficiency of the pulses results in better SNR at the receiver. We will investigate antenna distortions and multipath channel effects on UWB pulses using the programmable pulse shaper. We simulate the system using the Intel channel measurements and compare BER performance of several pulse shapes.

The multipath channel causes ISI at the receiver. Equalization techniques are important to combat the destructive effects of the ISI on the system performance. To compensate the severe ISI at gigabit rates, we investigate the Viterbi algorithm (VA) with a limited number of states and the decision feedback equalizer (Chapter 5). We will examine both LOS and NLOS channels for a receiver with a linear filter matched to the transmit waveform.

# Chapter 3

## UWB Pulse generation techniques

In this chapter we propose three optical UWB pulse generation techniques. Our solutions are compatible with WDM-PON distribution. We provide detailed simulation and experimental results of the optical pulse generators, as well as wireless transmission and receiver error performance analysis. The solutions proposed in this chapter are low cost and each has EIRP that completely respects the FCC mask when using the Sky-Cross commercial UWB antenna. Power efficiency of UWB pulses obtained by optical methods introduced in this chapter is lower than that of the pulse shaping using FBGs presented in Section 2.2.2. The advantage, however, is using simpler optical setups which offer possibility of integration in silicon technology.

In Section 3.1 we define EIRP and find a formula to express it as a function of the transmit power spectrum and the channel frequency response. In Section 3.2 we generate OOK UWB pulses by upconversion of gain switched optical pulses using a Mach-Zehnder modulator. We achieved 42% of power efficiency and reached the FEC limit after 3.5 m of wireless propagation. Instead of a gain switched laser, we use a continuous wave laser in our second pulse generation method (Section 3.3). We show that upconversion of optical signal by a combination of data and local oscillator results in UWB waveforms supporting OOK and PSK modulation formats. A continuous wave laser, a Mach-Zehnder modulator, and a photodetector are the only optical components used. BER is within the FEC limit after 2.5 m of wireless propagation when using an MMSE equalizer. Our third pulse generation method, presented in Section 3.4, is based on filtering gain switched laser pulses by an integrated silicon microring resonator. Balanced detection ensures FCC compliant pulses with 52% of power efficiency. This



method does not need an LO in contrast to the two methods based on upconversion. This saves electrical power at the transmitter. The drawback is high coupling loss of optical fiber to silicon chip, and polarization dependent loss of silicon waveguides.

### 3.1 EIRP calculation method

The FCC spectral mask regulates the spectral radiation of UWB pulses using the EIRP. EIRP depends on the pulse power and also the antenna gain. For an isotropic antenna the gain is identical in all directions, so that

$$G_T(f, \phi, \theta) = G_T(f) \quad (3.1)$$

where  $G_T$  is the transmit antenna gain,  $\phi$  is the zenith angle and  $\theta$  is the azimuth angle in the spherical coordinate system. The radiated power of an isotropic antenna at a reference distance  $d_{ref}$  is

$$IRP(f) = P_T(f) G_T(f) \quad (3.2)$$

where  $P_T(f)$  is the transmit power density. For an arbitrary antenna, not necessarily isotropic, the FCC requires that on any point of the sphere at  $d_{ref}$ , the radiated power should not exceed that of an isotropic antenna, hence the term EIRP.

$$EIRP(f) = \max_{\phi, \theta} P_T(f) G_T(f, \phi, \theta) \quad (3.3)$$

$$= P_T(f) G_T(f, \phi_0, \theta_0) \quad (3.4)$$

where  $(\phi_0, \theta_0)$  represents the direction of maximal gain. For simplicity we will write  $G_T(f)$  for the maximal gain of frequency  $f$  for any direction, hence

$$EIRP(f) = P_T(f) G_T(f) \quad (3.5)$$

A general procedure for determining the EIRP per unit bandwidth is the use of the Friis power transmission formula in its simple form where antennas are assumed to be both impedance and polarization matched [31]. The Friis equation, (2.2), is valid for antenna separation  $d$  larger than  $2D_{max}^2/\lambda$ , where  $D_{max}$  is the maximum dimension of the transmit antenna and  $\lambda$  is the free space wavelength. When  $D_{max}$  is much greater than the wavelength, the far field criterion becomes very large and the field strength that must be measured at the far field location is less than the receiver noise floor. In such cases, the near field measurement techniques should be used for EIRP determination.

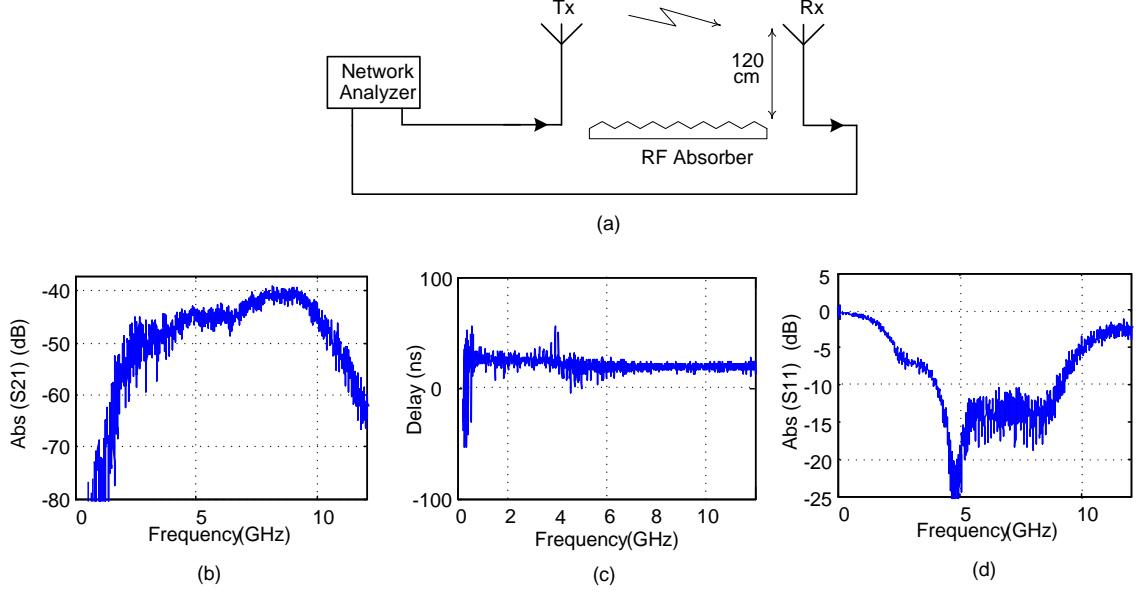


Figure 3.1: (a) The experimental setup for measuring the antenna frequency response, (b) antenna frequency response, (c) antenna link delay, and (d) antenna reflection response.

The dimensions of antenna and the maximum frequency of interest (10 GHz) in our case result in a reasonable far field distance where (2.2) is still valid, hence we apply it in the following.

To obtain the EIRP, we use similar transmit (Tx) and receive (Rx) antennas and measure, using a network analyzer, the total frequency response of system,  $H_{CH}(f) = P_R(f)/P_T(f)$ . This channel response,  $H_{CH}(f)$ , includes free space propagation and transmit and receive antennas responses. The orientations of antennas are carefully adjusted so that they face each other with the same angle. Thus, for similar transmit and receive antennas (identical models),  $G(f) = G_T(f) = G_R(f)$  and from the definition of EIRP and (2.2) we have

$$EIRP(f) = P_T(f) \sqrt{H_{CH}(f)} \left( \frac{4\pi df}{c} \right). \quad (3.6)$$

Fig. 3.1a shows the experimental setup to measure the antenna frequency response. We use a network analyzer (VNA-N5230A) to capture 6401 points across a span of 0.2 to 14 GHz and average 16 times to improve the dynamic range. We perform LOS transmission in a lab environment over a distance of 65 cm and a height of 120 cm off the ground. In our experiment we chose 65 cm to facilitate making measurements in

our somewhat confined laboratory environment. Please note that the distance between antennas plays no role in calculating EIRP from 3.6. Therefore, while any distance between antennas is possible, a closer range is preferable to reduce multipath reflections. The multipath was also attenuated by placing RF isolators around the antennas within the confines of our laboratory.

The antennas are placed in their peak radiation direction in the azimuth plane. Note FCC regulations require peak EIRP measurements over all directions, not only azimuth, however rotational antenna mounts were not available for our experiment.

Fig. 3.1b is the amplitude of the antenna frequency response ( $S_{21}$ ). We can see that the response is not completely flat in the radiation bandwidth of the antenna and this will obviously introduce differences between the transmitted and the received pulse shapes. The delay is fairly constant over the bandwidth of interest (Fig. 3.1c), a fact resulting from linear phase response of the antenna. Note the average delay value which comes from the distance between the antennas and the measuring equipment path delay. Therefore, all the frequency components of the transmitted pulse from the antenna undergo a certain delay while propagating in the channel, reducing temporal distortion of the pulse. Fig. 3.1d shows the reflected power from the antenna,  $S_{11}$ . This low reflection is an indication of the wide bandwidth of the antenna. Observation of the channel over longer periods of time shows no differences in the response and we conclude that the channel is non-varying.

The smoothed antenna frequency response is plotted in Fig. 3.2a. Fig. 3.2b plots the impulse response of the antenna obtained from the inverse Fourier transform of the frequency response. The inset figure shows the presence of several weak multi-path reflections from the indoor environment, in addition to main line-of-sight (LOS) response. These are mainly due to reflections from walls, ceiling, floor and lab equipments. Use of an RF absorber placed on the ground between the two antennas reduces the multi-path reflection by 75%, obviating the use of an anechoic chamber. We eliminate the remaining multipath reflections by truncating the measured impulse response.

We use a power amplifier (PA) before transmitting the pulses from the Tx antenna. Fig. 3.3 shows the frequency response of this amplifier measured using the vector network analyzer (VNA). The amplifier has an average gain of about 25 dB. We consider the gain response of the PA in the EIRP calculation.

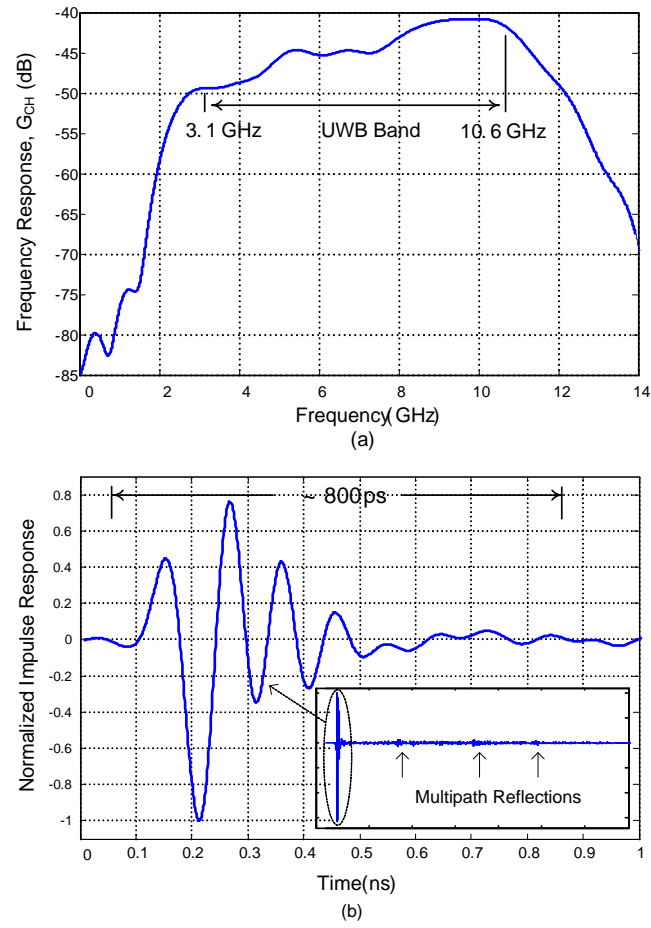


Figure 3.2: (a) Smoothed antennas frequency response, (b) normalized time response.

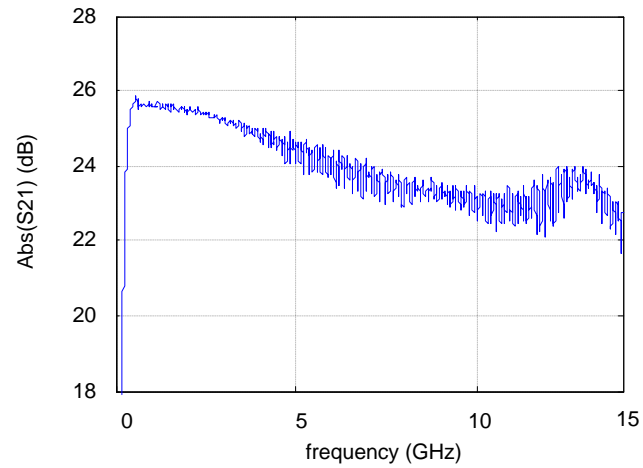


Figure 3.3: PA frequency response.

In this thesis we calculate the EIRP for all UWB waveforms we generate by the method explained in this section. We pay attention to the limits imposed by the FCC spectral mask and to power efficiency of pulses.

## 3.2 Upconversion of Gain-Switched Laser Pulses for Generation of UWB Signals

### 3.2.1 Introduction

We propose a simple method to generate UWB pulses by using an MZM to upconvert Gaussian-like pulses generated by a gain-switched laser. In contrast to our previous pulse shaping for UWB (Section 2.2.2), this design results in pulses with lower power efficiency, but is simpler and allows for an integrated, low cost implementation.

Fig. 3.4 shows the key idea of the proposed pulse generator. In our new approach, a DFB laser is gain switched to generate optical pulses. The pulses are modulated by the data stream in an optical intensity modulator. The GSL pulses are very short in duration and correspondingly very broad in spectrum. To generate UWB pulses we need to confine the spectral content of the pulses to less than 7.5 GHz. This can be done by dispersion in a length of SMF to temporally broaden the optical pulses. The optical fiber is also used to distribute the UWB signals from the central office to users. In Section 3.2.3 we will see how the SMF length influences the UWB pulse power spectral density. Another way to narrow the frequency response of the GSL pulses is using an optical filter. We design and fabricate a fiber Bragg grating (FBG) filter for this purpose. Using an FBG results in a compact solution for a stand alone in-home UWB transmitter.



Figure 3.4: Simplified block diagram of the proposed UWB waveform generator. GSL: gain switched laser, FBG: fiber Bragg grating, SMF: single-mode fiber.

After either SMF propagation or the FBG filter, the GSL pulses are mixed by a 6.85 GHz sinusoidal signal in a second optical modulator to upconvert their spectrum to the center of the FCC mask [36]. Finally, differential detection ensures good FCC compliance by removing low-frequency components. This design is compatible with WDM-PON distribution. Measurements show that pulses show good power efficiencies for distribution distances between 15 km and 25 km. The pulses generated by our technique have a power efficiency as high as the Gaussian fifth derivative and completely respect the FCC spectral mask. The Gaussian fifth derivative is a commonly adopted UWB pulse in electronics with power efficiency much higher than that of the monocycle.

Power efficiency is an important factor for transmit UWB pulses but the receiver bit error rate is the most significant criteria to evaluate a communication system. We consider, via simulation, a linear receiver and an energy detector to compute BER performance of our pulses. The linear filter response is matched to the transmit pulse resulting in a sub-optimal matched filter in an ISI channel. Pulses are transmitted and received by omnidirectional UWB antennas in the lab environment. The received bit sequence is saved using a realtime oscilloscope and later analyzed by offline signal processing. Various wireless distances are considered. We show that the system can achieve the forward error correction (FEC) BER requirement of  $10^{-3}$  in a 3.5 m wireless channel without equalization.

Upconversion is key in our proposed transmitter for UWB pulse generation. However, note that in contrast to common optical upconversion methods, we do not upconvert an electronically generated UWB pulse, but rather generate a UWB waveform in the 3.1 to 10.6 GHz band by optical upconversion. Previously, several optical approaches used an LO with an intensity modulator to upconvert various types of electronically generated UWB pulses to millimeter-wave bands for radio-over-fiber applications [37–40]. For instance, in [40] upconversion of monocycle pulse to the 24 GHz band for vehicular radar applications was demonstrated using a Mach-Zehnder modulator. As another example, optical frequency upconversion of orthogonal frequency division multiplexing OFDM-UWB signals to 60 GHz band was shown in [38], where two cascaded MZMs were used. The first MZM converted the orthogonal frequency-division multiplexing OFDM-UWB signals to optical domain and the second MZM performed the upconversion by using a 30 GHz LO.

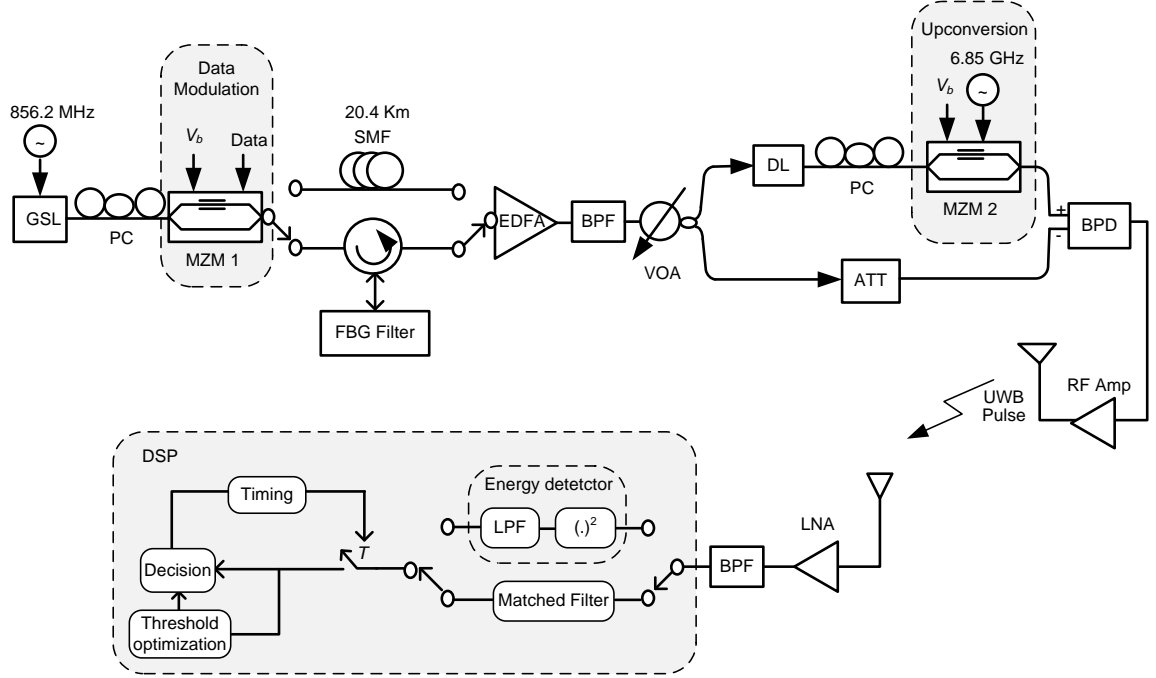


Figure 3.5: The schematic diagram of the proposed UWB waveform generator, and the receiving schemes. GSL: gain-switched laser, PC: polarization controller, MZM: Mach-Zehnder modulator, SMF: single-mode fiber, FBG: fiber Bragg grating, EDFA: erbium-doped fiber amplifier, BPF: bandpass filter, VOA: variable optical attenuator, DL: delay line, ATT: attenuator, BPD: balanced photodetector, LNA: low-noise amplifier.

### 3.2.2 Experimental setup

Fig. 3.5 shows the block diagram of the UWB pulse generator. A continuous wave (CW) distributed feedback (DFB) laser is gain-switched by applying a bias current below the lasing threshold in addition to a 856.25 MHz sinusoidal signal (chosen for experimental convenience). In the lab, we use a 6.85 GHz sinusoidal source to supply both the GSL and MZM 2 using a 1/8 frequency divider (Centellax TD40MCA). The laser output pulses are around 25 ps at full-width half-maximum (FWHM), measured with an autocorrelator and assuming a Gaussian pulse shape. These pulses are modulated using MZM 1. The modulator is biased at quadrature to produce OOK modulation of the optical pulses. The operating bit-rate is 856.25 Mb/s.

The short pulse duration of GSL pulses corresponds to a very wide spectrum. To produce pulses that fit within the FCC spectral mask limits, we need pulses with narrower power spectral densities. This can be achieved by employing a length of single

mode fiber or by an FBG filter. The fiber dispersion temporally broadens the optical pulses. The optical spectrum of the pulses remains unchanged after SMF dispersion (due to phase changes undergone). However, the electrical power spectral density (PSD) of the pulses after optical to electrical conversion (O/E) is narrowed due to the Fourier transform properties. This scheme is suitable for transport of the UWB pulses over WDM-PON. However, a fiber roll is too bulky if the UWB transmitter is to be used as a stand-alone device at home without a fiber distribution network.

While SMF in a PON provides the necessary dispersion for pulse broadening, our method could also be used in other settings. We examine a second implementation using an FBG filter to achieve a compact transmitter. The filter is a 40 mm long uniform weak reflection FBG used with a circulator. The strength of the refraction index modulation is Gaussian apodized to improve the side-lobe suppression. Its central wavelength is at 1556.36 nm with 0.08 nm bandwidth at 10 dB reflection. We fabricate the FBG using a standard phase mask scanning technique with a 244 nm ultraviolet (UV) beam. Fig. 3.6 shows the simulated and measured response of the FBG.

An erbium-doped fiber amplifier (EDFA) is used to amplify the pulses and compensate for the insertion loss of the modulator and the fiber length or FBG filter. Note that a semiconductor optical amplifier could be used for an integrated solution. The amplified spontaneous emission (ASE) from the EDFA is suppressed using a 1.2 nm optical bandpass filter. A variable optical attenuator is used to change the optical power of the pulses, in order to measure the BER curves presented later in Section IV.

A 3 dB coupler is used to divide the optical signal. The pulse shaping section of the setup consists of two branches. At the upper branch, there is a delay line (DL), a polarization controller (PC), and a 10 GHz Mach-Zehnder modulator (MZM 2). The only component in the lower branch is an attenuator (ATT). MZM 2 is biased at the quadrature point to perform the upconversion. The attenuator and the delay line are used to balance the power and the delay of the two branches. The two branches are connected to a 10 GHz (DSC-710) balanced photodetector (BPD).

The relative phase of the electrical sinusoidal signal to the laser pulses determines the pulse shape after MZM 2. To avoid phase drifts over adjacent pulses, the frequency of the sinusoidal signal applied to the MZM should be a multiple of the RF signal frequency supplied to the GSL. The use of a frequency divider to provide the sinusoidal input signals to the GSL and the MZM from a common local oscillator (LO) is practical



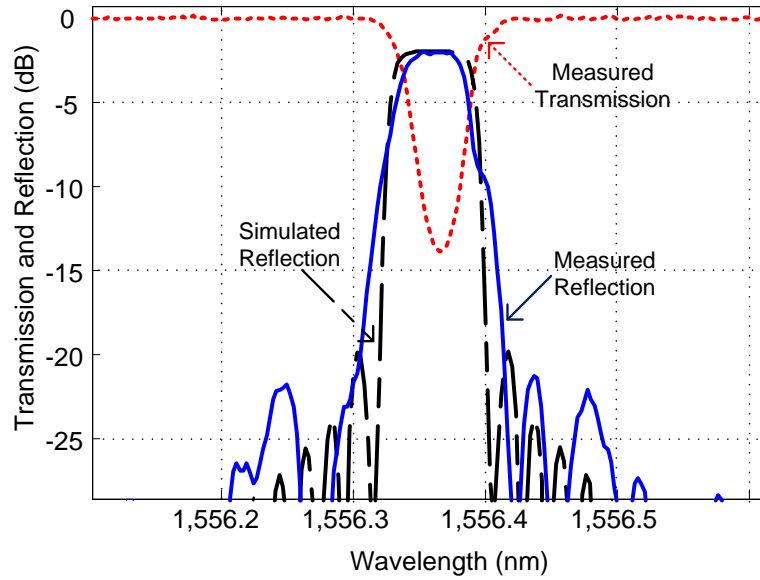


Figure 3.6: The simulated and measured response of the FBG at transmission and reflection.

for a compact transmitter. When fiber transmission of the signals is intended, using a phase-locked-loop (PLL) is the likely solution to generate stable UWB pulses. The PLL should retrieve a clock from the pulses arriving at MZM 2 (at 856.25 MHz in our experiment).

The relative phase of the sinusoidal signal applied to MZM 2 with the optical pulses can be adjusted by either using a delay line on the optical path or by changing the temperature of the DFB laser. The laser wavelength can be tuned by controlling the temperature, resulting in tunable phase shift between the laser pulses and the sinusoidal signal. Similar operation can be accomplished by placing an RF phase-shifter on the path of the 6.85 GHz electrical signal. We choose to tune the temperature of the laser as this facility was readily available in the lab.

Upconversion and data modulation can be achieved with only one MZM if an electrical mixer multiplies the data with the sinusoidal signal and the resulting waveform is applied to MZM 2. Unfortunately, such an approach is incompatible with PON distribution. Hence, MZM 1 is placed at central office for data modulation and MZM 2 does the upconversion at the user side (Fig. 3.5).

The UWB waveforms generated by this method are reconfigurable by adjusting the GSL current, MZM 2 bias point and by changing the relative phase of the modulation

signal to the optical pulses. In particular, tuning the GSL pulse shape, adjustable by the laser current, varies the spectral bandwidth of the generated pulses [41]. This control over the pulse spectral bandwidth can be used to counter the effect of accumulated dispersion from optical fiber propagation on pulses. Therefore, the UWB pulses are adjustable according to the SMF length, leading to good power efficiency for a range of distances.

The generated IR-UWB pulses are amplified by an RF amplifier before wireless transmission. We use a pair of the commercially available 3.1-10 GHz omni-directional SkyCross SMT-3TO10MA antennas. The antennas are placed at a height of 150 cm off the ground. They are adjusted in their peak radiation direction in the azimuth plane. At the receiver, the pulses are amplified by a low-noise amplifier (LNA, Mini-Circuits ZVA-183+). The out-of-band noise is rejected via a bandpass filter. The output from the bandpass filter (BPF) is captured using a PC-controlled 10 GHz realtime oscilloscope. The rest of the receiver, consisting of the linear filter or the energy detector, the timing acquiring unit and threshold optimization, is implemented in MATLAB. Note that in practical systems, an all digital receiver would sample at the Nyquist rate, which for UWB can be power inefficient and costly. Careful design of the analog front-end of the receiver can address this problem and reduce the sampling rate requirement to the symbol rate.

### 3.2.3 Simulation and Experimental Results

The main component in our setup is MZM 2. The transfer function of an MZM is given by

$$\frac{P_{out}}{P_{in}} = \frac{1}{2} \left\{ 1 + \cos \left( \frac{\pi}{V_{\pi}} (V_b + V_m \cos(\omega t + \phi)) \right) \right\}. \quad (3.7)$$

This equation can be expanded using the Bessel functions,

$$\begin{aligned} \frac{P_{out}}{P_{in}} = & \frac{1}{2} \left( 1 + \cos \left( \frac{\pi}{V_{\pi}} V_b \right) J_0 \left( \frac{\pi}{V_{\pi}} V_m \right) \right. \\ & - \sin \left( \frac{\pi}{V_{\pi}} V_b \right) J_1 \left( \frac{\pi}{V_{\pi}} V_m \right) \cos(\omega t + \phi) \\ & \left. - \cos \left( \frac{\pi}{V_{\pi}} V_b \right) J_2 \left( \frac{\pi}{V_{\pi}} V_m \right) \cos(2\omega t + \phi) \right). \end{aligned} \quad (3.8)$$

The first term in (3.8) forms a positive-definite pedestal observed in optical pulse generation techniques [42]. This undesired pedestal produces low frequency compo-

nents in the PSD of the signal, violating the FCC spectral mask. We suppress this pedestal by subtracting a copy of the gain-switched optical signal from MZM 2 output in a balanced photodetector, as previously demonstrated in [43]. In another method, balanced detection of two polarizations with complementary intensity modulation was proposed to eliminate the pedestal [44].

To generate maximum power at the fundamental frequency of the modulating signal, and to suppress the higher harmonics, (3.8) yields

$$V_b = V_\pi/2 \quad (3.9)$$

and

$$V_m = 3.6V_b/\pi. \quad (3.10)$$

We use a 6.85 GHz sinusoidal signal to modulate the optical pulses. From (3.9), at the quadrature point, MZM 2 output is mainly at the fundamental frequency of the electrical modulation signal. The available bandwidth under the FCC spectral mask is 3.1 to 10.6 GHz, centered around 6.85 GHz. Therefore, a 6.85 GHz modulating sinusoidal signal upconverts the pulses to the center of the FCC mask, resulting in a good FCC compliance. Setting the amplitude of sinusoidal modulating signal according to (3.10) maximizes the power of the upconverted signal.

It is worth noting that biasing the MZM at its maximum or minimum transmission points results in an output mainly at the second harmonic of the modulation signal. Thus, a 3.425 GHz modulating signal will upconvert the pulses to 6.85 GHz. Other bias points will produce both the fundamental and the second harmonics.

The optical pulses after SMF propagation are measured using a sampling oscilloscope (Agilent 86100A) and have a FWHM of about 100 ps (Fig. 3.7a). We use this measurement to simulate the two branches and the balance-detection scheme in Fig. 3.5. The simulation is compared to the measurement of the signal at the output of MZM 2 (Fig. 3.7a). The phase of the modulating signal is adjusted in simulation to result in the best match with the measurement. This is done by finding the autocorrelation maximum of the simulated waveform and the measured pulse at MZM 2 output, when sweeping the phase between 0 and  $2\pi$ .

After balanced detection, the UWB waveform and the simulation show a close match (Fig. 3.7b). The pulse has a duration of about 450 ps. The normalized PSD of the pulse,

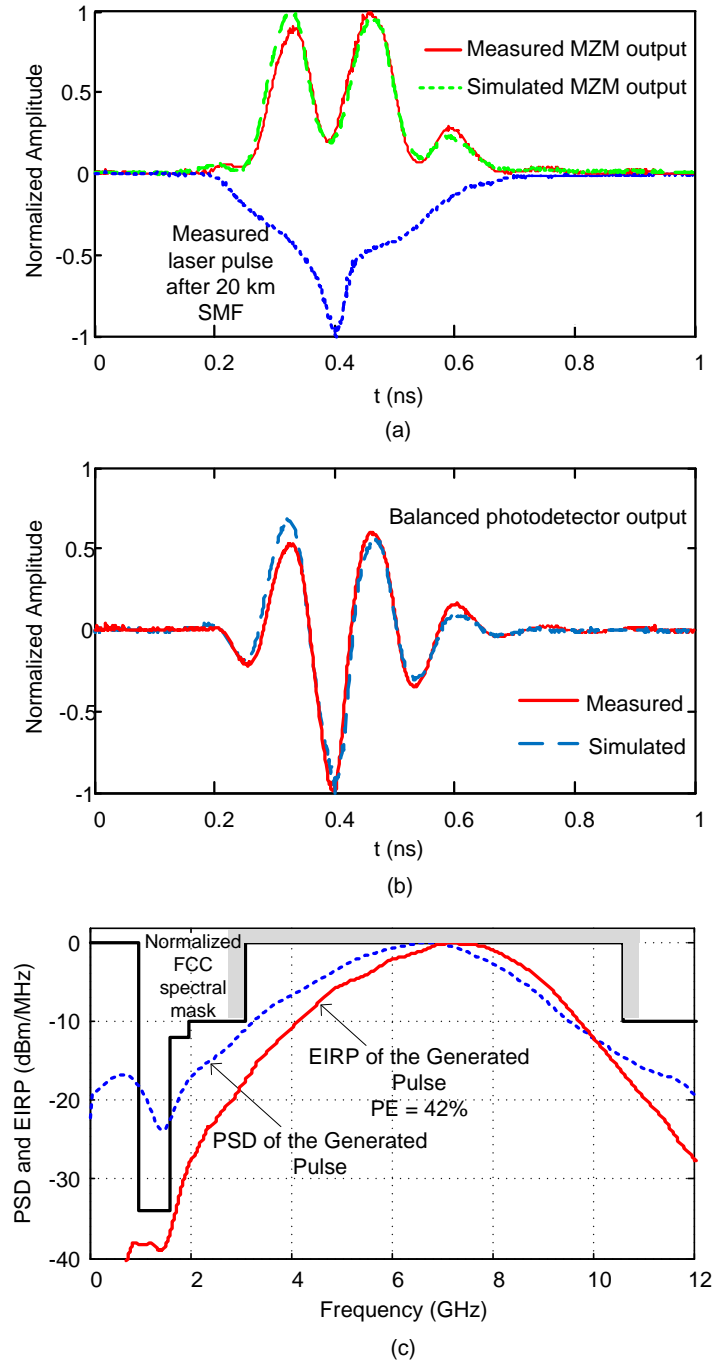


Figure 3.7: (a) the simulated and measured response at the MZM output (from the positive input of the BPD), and the measured GSL pulse after 20 km fiber propagation (from the negative input of the BPD). (b) the simulated and measured UWB waveforms. (c) The normalized PSD and EIRP of the UWB pulse.

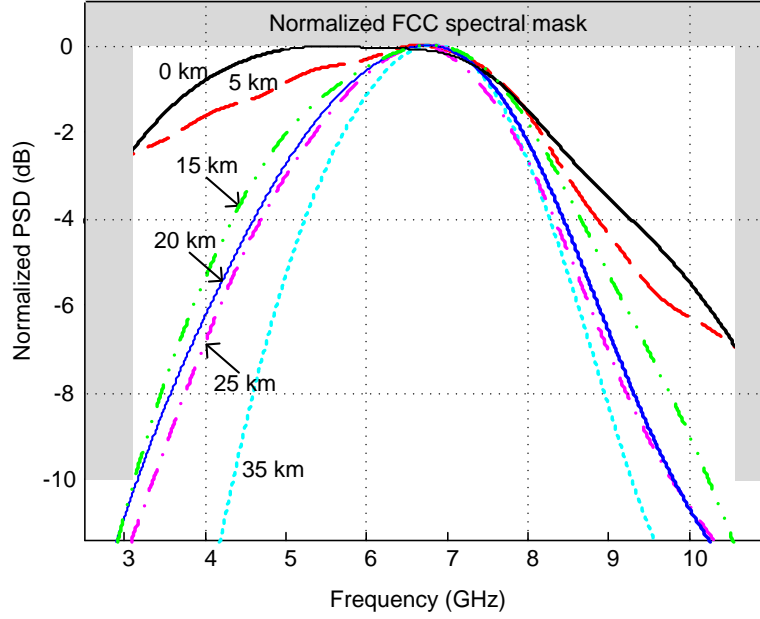


Figure 3.8: The normalized PSD of UWB waveforms for various optical fiber lengths plotted against the 3.1-10.6 GHz band of the FCC spectral mask.

obtained from the Fourier transform of the time domain pulse, is plotted in Fig. 3.7c. We can see that the PSD is maximum at 6.85 GHz and has a good FCC spectral mask compliance. Some of the loss at higher frequencies is due to the frequency response of the BPD inflicting around 3 dB of loss at 10 GHz compared to the DC level.

The normalized EIRP of our pulse is simulated and shown in Fig. 3.7c. The EIRP fully respects the FCC mask. The power efficiency is defined as

$$\text{PE} = \frac{\int_{BW} \text{EIRP}(f) df}{\int_{BW} S_{FCC}(f) df}, \quad (3.11)$$

where  $S_{FCC}$  is the FCC spectral mask. The PE is calculated over the 3.1-10.6 GHz band (see grey shading of the FCC mask in Fig. 3.7c). The power efficiency for the pulse shown in Fig. 3.7b is 42%. Using the same antenna, the power efficiency of the Gaussian monocycle and the Gaussian fifth-derivative would be 4% and 40%, respectively [45].

The pulse shown in Fig. 3.7b was obtained after 20 km of SMF fiber. When the length of fiber changes, the pulse duration varies because of dispersion. The GSL pulse shapes depend on the DC bias current of the laser. We tune the DC bias current between 5 mA and 9 mA and find pulses that result in the best PSD. Fig. 3.8 shows that a good mask coverage is possible for distances between 15 km and 25 km. The extra dispersion at 35 km results in a narrow PSD and decreases the PE.

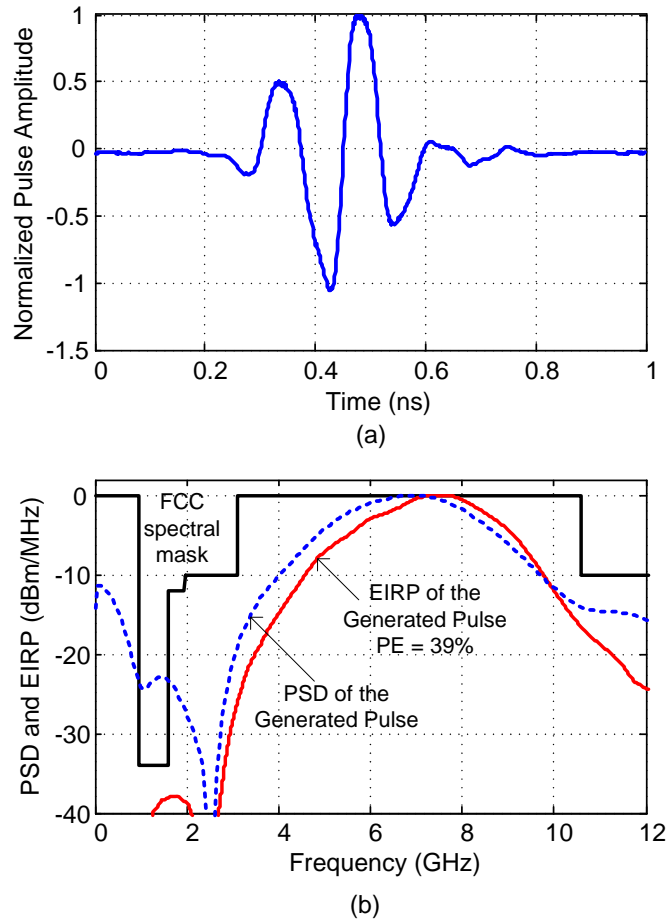


Figure 3.9: (a) UWB waveform generated using the FBG filter at the transmitter, (b) The normalized PSD and EIRP of the UWB pulse.

With no fiber dispersion, the pulse is very short and the PSD too wide (Fig. 3.8). While in Fig. 3.7a we used SMF to disperse the pulse, in Fig. 3.9a we report on the use of an FBG filter to slice the spectrum and fit it to the limits of the FCC mask. Fig. 3.9a shows the waveform generated using the FBG and measured by the sampling scope with 16 averages. Fig. 3.9b shows the PSD, obtained from Fourier transform, and the EIRP of this pulse. The PE is 39% in this case, when the FCC mask is perfectly respected.

Table 3.1: Link budget

Parameter	Value
Bit rate	856.25 Mb/s
Transmit power	-6.5 dBm
4 m path loss	59.3 dB
Antenna gain	0 dB
Noise figure	4 dB
BER	$10^{-3}$
Link margin	5 dB

### 3.2.4 BER performance of the receiver

In this section, we investigate wireless propagation of the UWB pulses. The average power of the transmitter is set to the maximum permissible by the FCC spectral mask. This power is -6.5 dBm for a pulse with PE = 40%. The transmit pulses are modulated by a pseudorandom bit sequence (PRBS) of length  $2^7 - 1$ . To achieve a BER of  $10^{-3}$  for OOK data,  $E_b/N_0$  should be 10 dB, where  $E_b$  is the energy per bit and  $N_0$  is the noise power spectral density. From [4], the channel loss is estimated as

$$L = 20 \log(4\pi \sqrt{f_l f_u} d / c) \quad (3.12)$$

where  $f_l$  and  $f_u$  are the lower and upper frequency band, respectively.  $c$  is the speed of light, and  $d$  is the antenna separation. Table I shows the link budget analysis of the UWB wireless link.

The receiver sensitivity [31], defined as

$$S_{min} = -174 + R + NF + E_b/N_0 + Margin, \quad (3.13)$$

where  $R$  is the bit rate, can be calculated according with values from Table I and equals -65.6 dBm. Maximum 4 m of wireless propagation is possible with this sensitivity. For farther transmission, we need an LNA with better noise figure (NF), or some receiver antenna gain. Since omnidirectional antennas are preferred for indoor UWB systems, receive antenna arrays with beam steering can provide this gain. More efficient modulation formats, such as BPSK, reduce the required  $E_b/N_0$ . Lowering the bit-rate will also increase the range of communication.

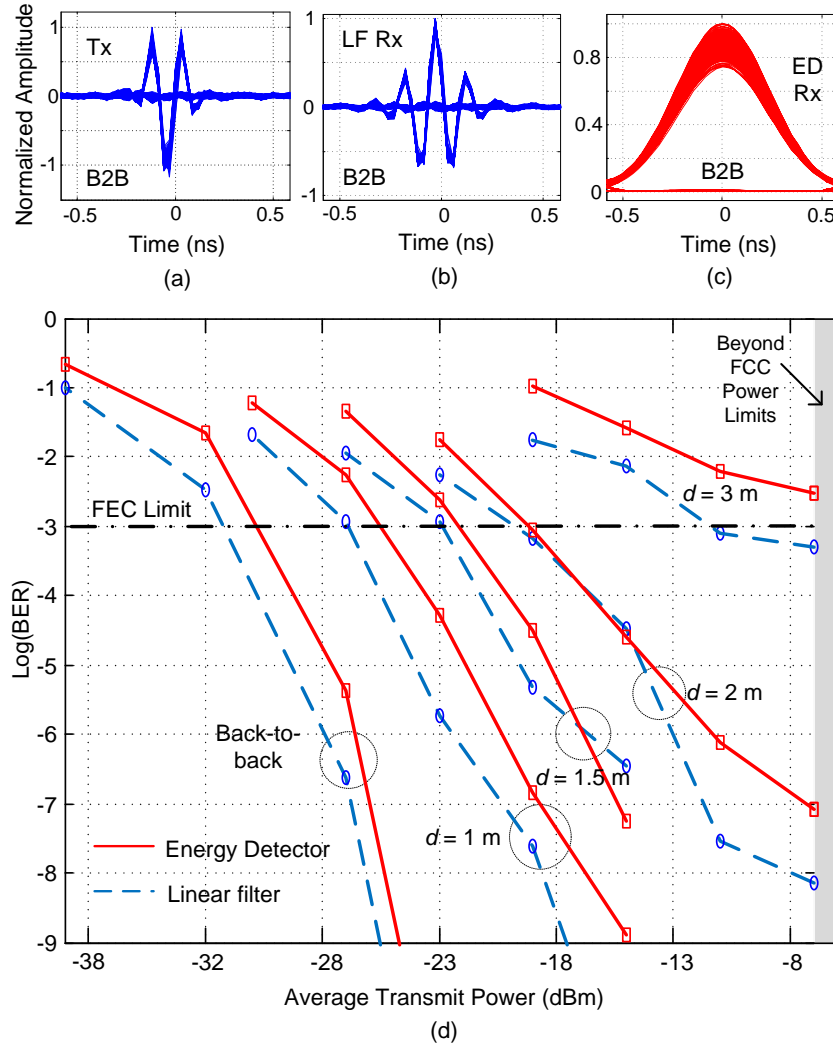


Figure 3.10: UWB transmitter with 20 km of SMF, (a) eyediagram of the transmit pulse, (b) eyediagram of the linear filter output, (c) eyediagram of the energy detector output, (d) BER versus average transmit power plotted for various wireless distances.



We consider a linear receiver matched to the transmit pulse and an energy detector receiver. Both are implemented in MATLAB by processing the captured data from the scope. The scope takes a maximum of  $2^{20}$  samples at 40 Gsamples/s. We match the captured bit sequence with the PRBS data and perform the timing acquisition to find the sampling time. A threshold optimization stage follows. At each SNR, the threshold value that minimizes the number of decision errors is chosen as the optimal threshold. This threshold value exactly corresponds to the middle of the received signal eye diagram opening. Detection is based on hard decision of the samples versus the threshold. Because of the low number of bits, we calculate the BER from Q-factor approximation.

Note that the linear filter is a matched filter in back-to-back tests but in an ISI channel the received pulse can significantly differ from the transmit waveform. Matching to the transmit pulse is not optimal, but its implementation is straight forward. We do not examine equalization, however several techniques are suggested in the literature [46, 47].

Fig 3.10a shows the eyediagram of the transmit signal captured at maximum allowed power, after 20 km of SMF. Fig 3.10b depicts the eyediagram at the output of the linear filter, and Fig 3.10c corresponds to the output of the energy detector. We can see that the eye is much narrower in case of the linear receiver, thus requiring more precise synchronization.

Fig 3.10d shows the BER performance of the linear and the energy detector receivers. The antennas are placed in LOS and their distance is varied between 1 m and 3 m, at the lab environment without using any RF absorbers for reducing ISI. At close range the linear receiver and the energy detector have a similar performance, but the linear receiver outperforms the energy detector by almost 5 dB, in terms of  $E_b$ , after 2 m of wireless propagation. We observe error floors in the BER curves at 3 m, resulting from ISI. The lab environment can be considered as a severe ISI channel as it contains many metal instruments. Equalization techniques to combat the ISI are necessary to further increase the range of error-free communication. These methods are extensively covered in the literature [46, 47].

Fig 3.11a, Fig 3.11b, and Fig 3.11c show, respectively, the eyediagram of the transmit pulse, the linear filter output, and the energy detector output, when using the FBG filter at the transmitter. Wireless propagation up to 2.5 m is considered. The BER

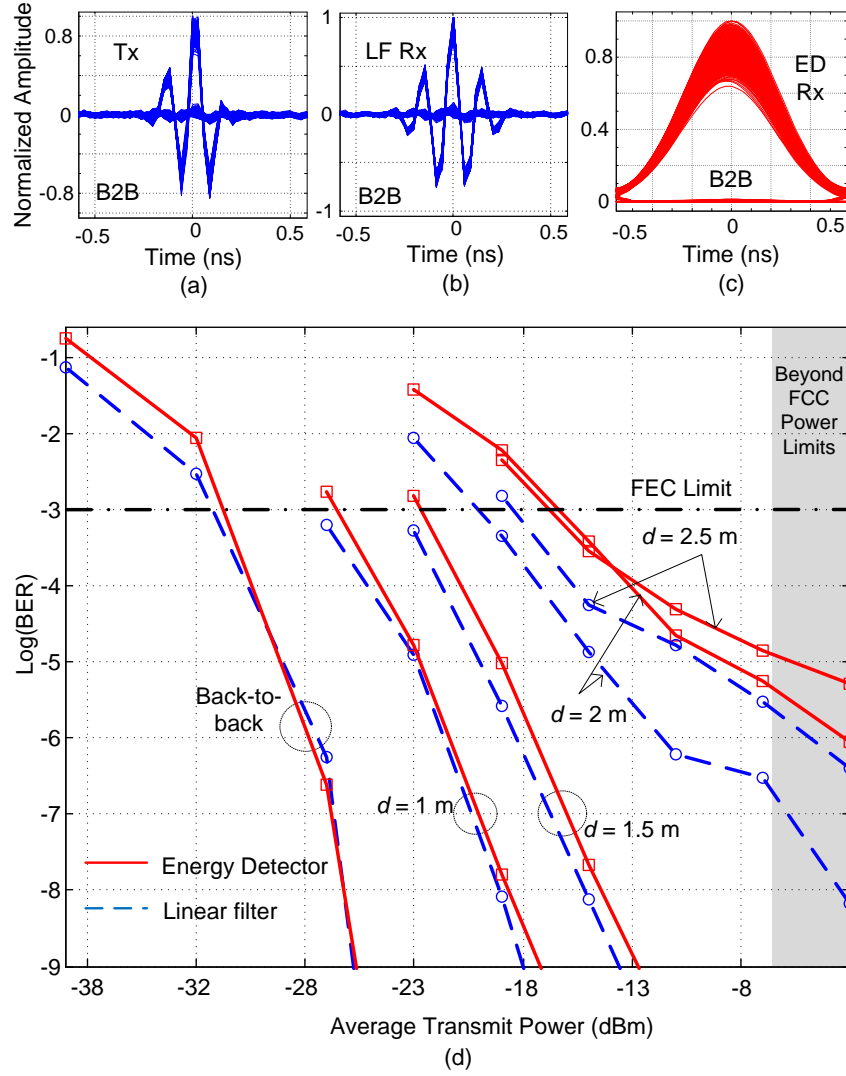


Figure 3.11: UWB transmitter with FBG filter, (a) eyediagram of the transmit pulse, (b) eyediagram of the linear filter output, (c) eyediagram of the energy detector output, (d) BER versus average transmit power plotted for various wireless distances.

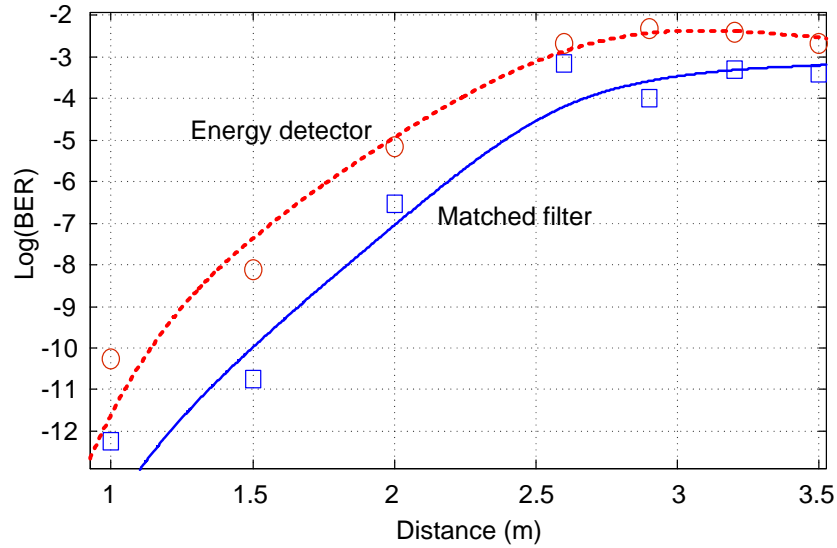


Figure 3.12: (a) BER versus wireless transmission distance. The average transmit power is set to -6.5 dBm for the transmitter with the FBG filter.

curves versus  $E_b$  are plotted in Fig 3.11d. The BER performance of the transmitter with the FBG filter follows the same pattern as that of the transmitter with the SMF.

In a real scenario, the UWB transmitter always works with the maximum allowed power and it is the received power that changes with wireless propagation. We perform this experiment for the transmitter with the FBG filter in Fig 3.12, in which the average transmit power is set to -6.5 dBm and the wireless propagation distance varies between 1 m and 3.5 m. The linear receiver satisfies the FEC threshold for all the distances, whereas the energy detector is limited to 2.5 m.

### 3.3 Low Complexity generation of BPSK UWB signals

#### 3.3.1 Introduction

In this section, we show a very cost-effective method of UWB pulse generation by only using an optical source, an external modulator and a photodetector. In contrast to our previous pulse generator (Fig. 3.4), the new setup uses a continuous wave

laser, a single intensity modulator and does not require balanced detection. Our new method is easily applicable to PON. The data is added to a sinusoidal waveform and the summation modulates the light intensity using a MZM (Section 3.3.2). We will show that with proper choice of data amplitude, sinusoidal signal amplitude and MZM bias point, OOK or BPSK UWB signals can be generated within the UWB frequency band (Section 3.3.3). Optical signals are converted to RF and transmitted wirelessly. In Section 3.3.4 we experimentally investigate this method, using a realtime oscilloscope to capture the RF signal at the receive antenna following wireless propagation via two UWB antennas. We investigate the EIRP of transmitted wireless signals. The received signal is equalized in MATLAB using a minimum-mean-square-error (MMSE) algorithm [48] to reduce the intersymbol interference. BER performance of the system is investigated.

While our method resembles setups for upconversion of UWB signals using an MZM, our approach is quite different. In [39], a UWB monocycle pulse was upconverted using the summation of the pulse and a local oscillator to modulate a laser diode via an MZM. Similarly, upconversion of OFDM-UWB signals was demonstrated in [37]. Note that in our approach we generate UWB pulses rather than upconverting previously generated UWB waveforms.

An advantage of this method compared to our other pulse shaping techniques is its support for BPSK modulation format. It is well known that BPSK signals lead to better BER performance compared to OOK modulation format. Generation of OOK UWB signals is convenient in the optical domain by using a Mach-Zehnder modulator. However, BPSK signal generation is more challenging in optical domain.

Bi-phase modulation of Gaussian monocycle pulses was shown in [49] based on a phase modulator and an asymmetric Mach-Zehnder interferometer. In [50], a 781.25-Mb/s binary BPSK UWB transmission system exploited relaxation oscillations of a DFB laser. BER results showed that 30 km of fiber transmission introduced almost no penalty, however, the pulses in [49, 50] were not FCC compliant.

In another work an arbitrary waveform generator was used in [51] to transmit 2 Gb/s BPSK UWB signals over a one meter wireless channel. A digital coherent receiver was employed to detect the pulses, involving a local oscillator laser beating with the signal in a 90° optical hybrid. Two pairs of balanced photodiodes converted the signal to the electrical domain. Digital signal processing was performed afterwards to compensate

fiber chromatic dispersion. They reported 1.4 dB penalty without dispersion compensation after 23 km of SMF. In Section 3.3.4 we show around 1 dB penalty after 20 km of SMF propagation in our pulse shaper.

### 3.3.2 Experimental Setup

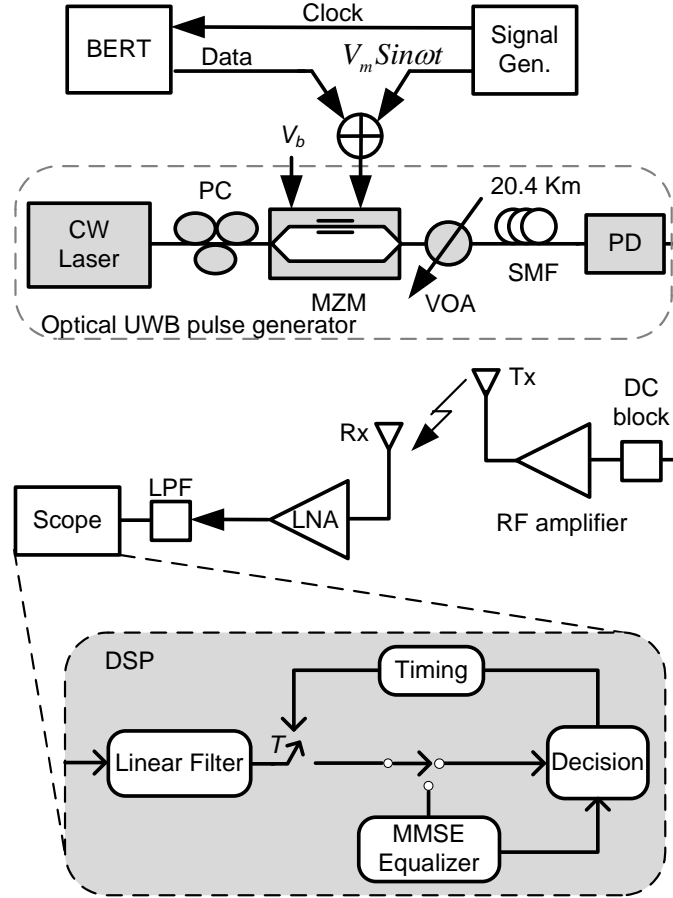


Figure 3.13: The schematic diagram of the experimental setup. PC: polarization controller, MZM: Mach-Zehnder modulator, VOA: variable optical attenuator, SMF: single-mode fiber, PD: photodetector, LNA: low-noise amplifier, LPF: lowpass filter.

Fig. 3.13 shows the block diagram of the UWB signal generator and the receiver structure. A continuous wave (CW) laser biased above threshold is used as the source. A polarization controller (PC) followed by a 10 GHz Mach-Zehnder modulator (JDSU OC-192) perform the data modulation. A power combiner (Marki PD-0010) combines the data coming from a bit error tester (BERT) with a 7 GHz sinusoidal signal generated from the signal generator. Note that the sinusoidal signal also serves as the BERT clock

input. A variable optical attenuator is used to change the optical power of the pulses, in order to measure the BER curves presented later. Single-mode fiber can be placed after the VOA to study the effect of fiber transportation on the UWB pulses.

A photodetector (PD) performs the optical-to-electrical (O/E) conversion. A DC-block eliminates the DC value of the electrical signal. The resulting UWB pulses are amplified and transmitted using the SkyCross SMT-3TO10MA antennas. The received waveforms are amplified using a low noise amplifier (LNA, Mini-Circuits ZVA-183-S) and captured by a PC-controlled 10 GHz realtime oscilloscope. Detection and BER calculation is performed by offline digital signal processing (DSP) in MATLAB (Section IV).

### 3.3.3 Theoretical Study

The transfer function of the MZM, configured as shown in Fig. 3.13, is expressed as

$$\frac{P_{out}}{P_{in}} = \cos^2 \left( \frac{\pi}{2V_{\pi}} (V_b + D(t) + V_m \sin \omega t) \right) \quad (3.14)$$

where  $P_{in}$  and  $P_{out}$  are the input and output optical powers,  $V_{\pi}$  is the MZM half-wave voltage,  $V_b$  is the bias voltage,  $D(t)$  is the data signal, and  $V_m$  is the amplitude of the sinusoidal signal. This transfer function can be expanded using the Bessel functions

$$\begin{aligned} \frac{P_{out}}{P_{in}} = & \left\{ \frac{1}{2} + \frac{1}{2} J_0 \left( \pi V_{\pi} / V_m \right) \cos \left( \frac{\pi}{V_{\pi}} (V_b + D(t)) \right) \right. \\ & - J_1 \left( \pi V_{\pi} / V_m \right) \sin \left( \frac{\pi}{V_{\pi}} (V_b + D(t)) \right) \sin \omega t \\ & \left. + J_2 \left( \pi V_{\pi} / V_m \right) \cos \left( \frac{\pi}{V_{\pi}} (V_b + D(t)) \right) \cos 2\omega t + \dots \right\}. \quad (3.15) \end{aligned}$$

The second and higher order harmonics in (3.15) are out of the UWB band and are filtered out by the bandpass response of the UWB antennas. The DC term in (3.15) should be data independent so that it can be removed using a DC block. In particular we will find values of oscillator amplitude  $V_m$ , and data amplitude for logical zero and one ( $D^0$  and  $D^1$ , respectively) such that the DC term equals  $0.5P_{in}$ .

Clearly for  $\cos \left( \frac{\pi}{V_{\pi}} (V_b + D) \right) = 0$  we meet our requirement, yielding  $D^0 = -V_{\pi}/2 - V_b$ , and  $D^1 = V_{\pi}/2 - V_b$ . Thus, The data amplitude is  $V_{\pi}$  while  $V_b$  and  $V_m$  are not

constrained. With this choice for the data amplitude, (3.15) can be expressed as

$$P_{out} = \begin{cases} -P_{in} J_1(\pi V_\pi/V_m) \sin \omega t & D(t) = D^1 \\ P_{in} J_1(\pi V_\pi/V_m) \sin \omega t & D(t) = D^0 \end{cases} \quad (3.16)$$

We can see that a BPSK modulation format is achieved with an amplitude depending on  $V_m$ .

Another solution to having a data independent DC results in OOK modulation format [52]. In (3.15) we can choose  $J_0(\pi V_\pi/V_m) = 0$ , resulting in the sinusoidal signal amplitude  $V_m = V_\pi/\pi J_0^0$ ,  $J_0^0$  being the first zero of the Bessel function of the first kind. In OOK modulation, the signal should be zero for logical data zero, *i.e.*,  $D(t) = D^0$ . Therefore, from (3.15),  $\sin\left(\frac{\pi}{V_\pi}(V_b + D^0)\right) = 0$ , leading to  $D^0 = V_\pi/2 - V_b$ . With these conditions fulfilled, (3.15) simplifies to

$$P_{out} = \begin{cases} -P_{in} J_1(\pi V_\pi/V_m) \sin \omega t & D(t) = D^1 \\ 0 & D(t) = D^0 \end{cases} \quad (3.17)$$

The result is an OOK modulation format.

### 3.3.4 Experimental Results and Discussion

In this section, we use the setup shown in Fig. 3.13 along with the mathematical expressions developed in Section 3.3.3 to generate UWB pulses with OOK and PSK modulation formats, and also multiband-UWB signals. The modulator we used has  $V_\pi = 3.2$ .

#### OOK modulation

We generate the sinusoidal signal with frequency of 6.85 GHz to center the UWB pulses in the middle of the FCC spectral mask. The BERT generates bits at 6.85 Gb/s with a pattern of ‘1100 0000’ for logical one and ‘0000 0000’ for logical zero. The UWB bit rate is therefore 850 Mb/s. The modulator  $V_\pi$  of 3.2 results in  $V_m = V_\pi/\pi J_0^0 = 2.5$  V.

Fig. 3.14a shows the generated UWB pulse after adjusting the MZM bias and data amplitude. The pulse has a duration of about 400 ps which is more than the 300 ps duration of ‘11’, due to filtering the data with a 7.3 GHz lowpass filter (LPF). We

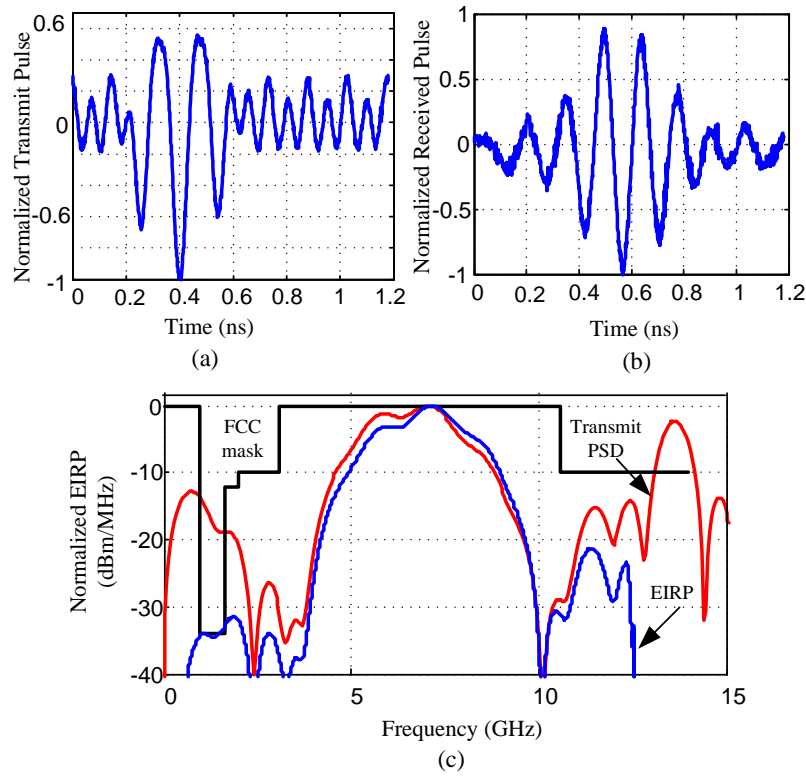


Figure 3.14: (a) The normalized transmit UWB signal, (b) the normalized received waveform, and (c) the power spectral density of the transmit pulse (red) and the EIRP (blue).

observe a rapidly oscillating signal when the data is zero. This is the residual second harmonic in (3.15). This oscillation, however, is insignificant at the receiver as it is effectively filtered by the bandpass behavior of the UWB antenna. Fig. 3.14b shows the normalized measured received pulse after antenna transmission over a distance of about 70 cm in the lab environment.

The normalized EIRP is calculated and shown in Fig. 3.14c (blue line). Comparing the EIRP with the transmit pulse spectrum (Fig. 3.14c, red line), the second harmonic has been eliminated by the antenna and the EIRP respects the FCC spectral mask. Note that wider spectrum could be expected if the signal and data generators worked at different frequencies, allowing for more precise adjustment of the pulse duration.



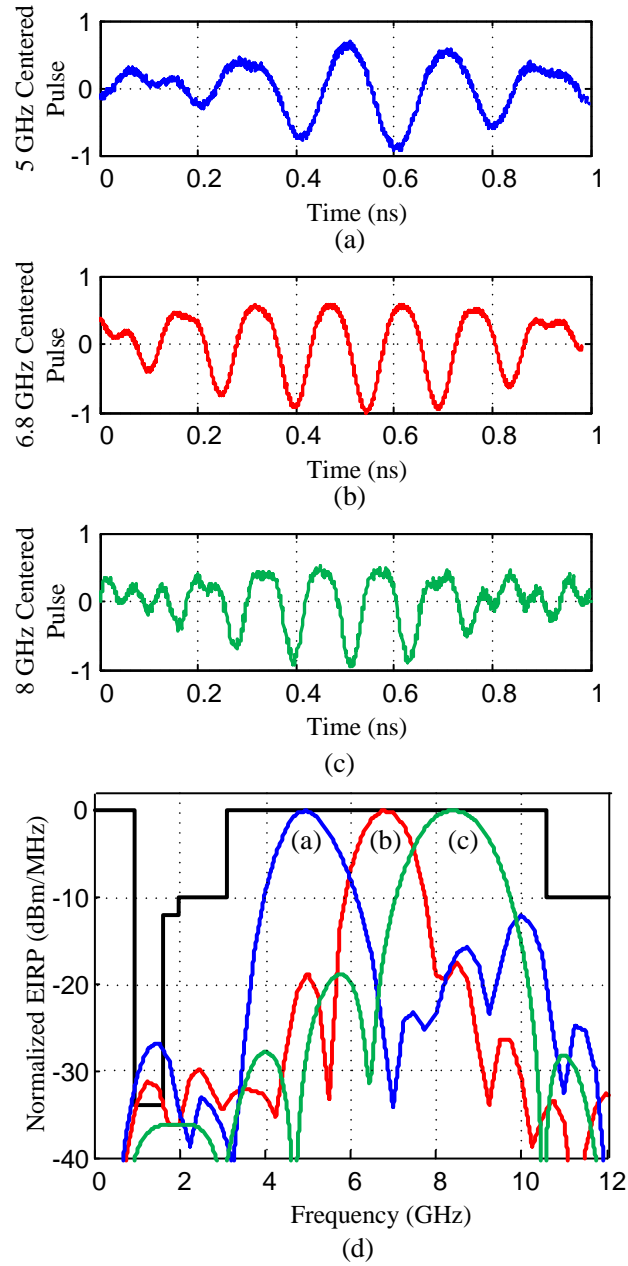


Figure 3.15: The multiband-UWB signals centered around (a) 5 GHz, (b) 6.8 GHz, and (c) 8.5 GHz. (d) The corresponding EIRP plots.

## Multiband-UWB

We focus predominantly on IR-UWB, however this pulse generation method could also be applied to MB-UWB (see Section 2.1.2). The MB-UWB can be generated similarly to the OOK pulses. The data pattern is set to ‘1111 1100’ to generate pulses with longer time durations. The center frequency of the band is set by the frequency of the sinusoidal signal. A 933 MHz LPF is used to narrow the spectral width of the pulses. From the Fourier transform properties, the longer the time duration of the pulse, the narrower its frequency content.

Fig. 3.15a, Fig. 3.15b, and Fig. 3.15c show pulses centered at 5 GHz, 6.8 GHz, and 8.5 GHz, respectively. We can see that the pulses have different durations because the duration of the pattern changes depending on the BERT bit rate. The solution would be using an independent clock signal for the BERT. Fig. 3.15d plots the calculated EIRP for each of the multiband-UWB signals superimposed in one figure. It is observed that the pulses do not have the same spectral bandwidth, which can be attributed to their difference in the time duration. The second harmonic for the pulse centered around 5 GHz falls at 10 GHz, which makes it difficult to filter as it is in the UWB band.

## PSK modulation

We bias the MZM at its quadrature point. The data changes the operating point of the modulator between the positive and negative slopes of the modulator transfer function. The peak-to-peak of the sinusoidal signal was around 4 V. This value does not maximize the output power, but was chosen experimentally by examining the output signal eyediagram.

The 7 GHz sinusoidal signals ensures generation of UWB signals at the center of the FCC spectral mask. We generate the data bit 1 with the pattern ‘1111’ and a data bit 0 with the pattern ‘0000’, corresponding to a symbol rate of 1.75 Gb/s. The choice for this data duration was made to achieve reasonable bit-rate and signal bandwidth for high speed UWB applications. The patterns ‘1111’ and ‘0000’ generate out-of-phase pulses with the same duration.

Fig. 3.16a shows the generated PSK UWB pulses. The pulse duration is about 0.6 ns. Fig. 3.16b plots the measured received signals after antenna transmission. The

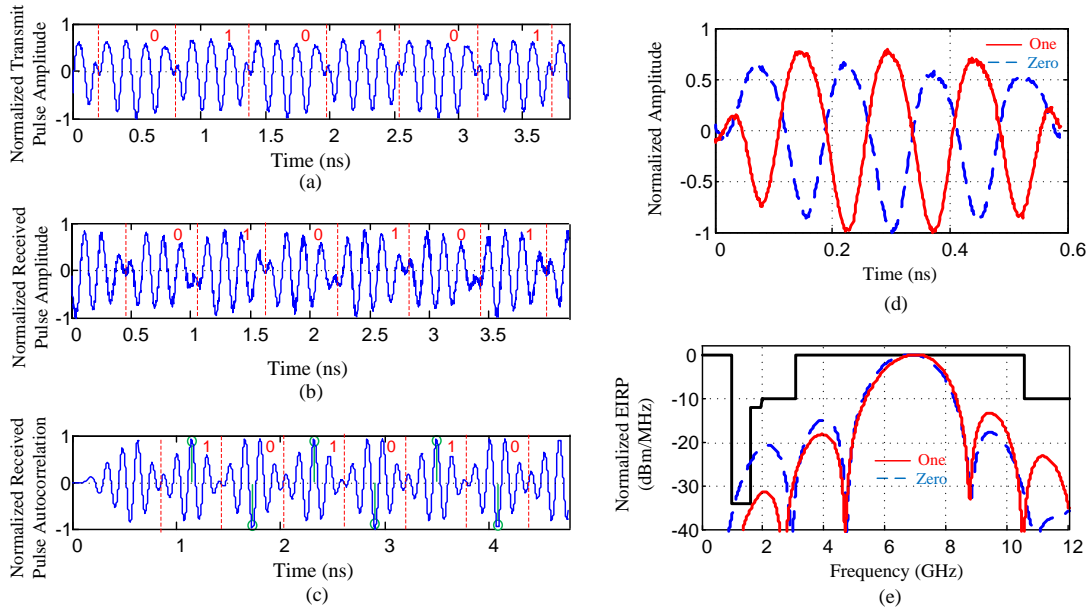


Figure 3.16: The PSK scheme. (a) The transmit UWB pulses, (b) the received waveforms, (c) the autocorrelation function of the received waveform, (d) superposition of a 1 and a 0, and (e) the EIRP of the 1 and 0 pulses.

autocorrelation function of the received signal (Fig. 3.16c) shows that a correlator or matched filter receiver can easily decode the PSK signal by employing a zero threshold. The sampling times are pointed by green circles in Fig. 3.16c. Superposition of a zero and a one is shown in Fig. 3.16d. Fig. 3.16e shows the EIRP for the zero and one signals. The spectral bandwidth can be tuned by changing the data pattern.

Fig. 3.17a shows the measured eyediagram of the generated PSK UWB pulses for a PRBS of length  $2^7 - 1$ . Fig. 3.17b plots the measured received signals after 50 cm of wireless transmission in the lab. Although the eye is open before transmission, the ISI caused by the multipath reflections severely distorts the received signal at the very high speed (1.75 Gb/s). The non-return-to-zero (NRZ) nature of the generated UWB pulses exacerbates the ISI.

Fig. 3.17c (gray) shows the PSD of the generated PRBS UWB sequence measured using an electrical spectrum analyzer. The normalized EIRP is calculated and shown in Fig. 3.17c (blue/dark). Comparing the EIRP with the PSD of transmit waveform (Fig. 3.17c, gray), the second harmonic, centered at 14 GHz, has been eliminated by the antenna and the EIRP respects the FCC spectral mask. The fractional bandwidth

of the waveform is 30%.

We consider a linear receiver matched to the transmit pulse implemented in MATLAB by processing the captured data from the scope. The scope takes a maximum of  $2^{20}$  samples at 40 Gsamples/s. We match the captured bit sequence with the PRBS data and perform timing acquisition to find the sampling time. This is achieved by finding the peak of correlation function between the PRBS and the received signal. The threshold is set to zero. Detection is based on hard decision by comparing the samples with the threshold. Because of the low number of bits, we calculate the BER from the Q-factor using a Gaussian noise approximation.

Fig. 3.17d plots the BER versus the average optical power. The penalty from SMF propagation is less than 1 dB, making the system suitable for use in passive optical networks. This penalty can be attributed to chromatic dispersion. In [51], it was shown that applying dispersion compensation reduces the penalty to less than 0.5 dB, even for longer SMF. No significant change on the PSD was observed after adding the SMF. Fig. 3.18 shows the BER performance of the receiver after several wireless distances. With no equalization the system is limited to 1.5 m when respecting a FEC limit of  $10^{-3}$ . Error floors are caused by the ISI. We employ an MMSE equalizer to combat the ISI. The equalizer is trained with the PRBS data bits for an overhead of about 15% to compute the cross-correlation between received sequence and input sequence and the autocorrelation of the received sequence. Adaptive MMSE can be used to lower the overhead. Fig. 3.18 shows much better BER performance after equalization, where the BER at 2.5 m is well within the FEC range.

## 3.4 UWB waveform generation using a microring resonator

### 3.4.1 Introduction

Although the optical domain is favorable to generation of UWB signals, the high cost and bulkiness of the optical components have been major drawbacks in commercialization of these UWB systems. Integration of optical components on silicon is highly interesting for UWB, and in general for microwave photonics applications, because of

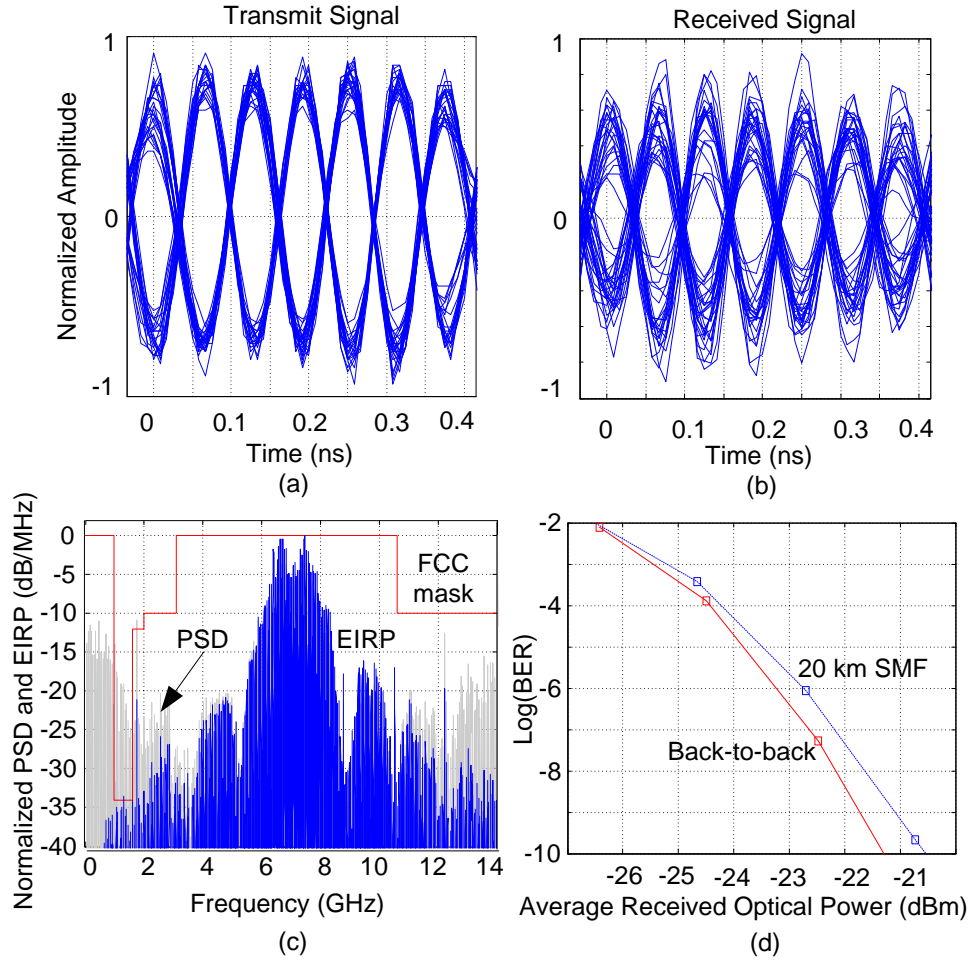


Figure 3.17: The PSK signals. (a) The eyediagram of the UWB signal at the transmitter, (b) The eyediagram of the received signal after 50 cm of wireless propagation, (c) the power spectral density of the transmit pulses obtained from the electrical spectrum analyzer (gray), the normalized EIRP (blue), vs. the FCC mask (red). (d) the BER performance for back-to-back and 20 km SMF.

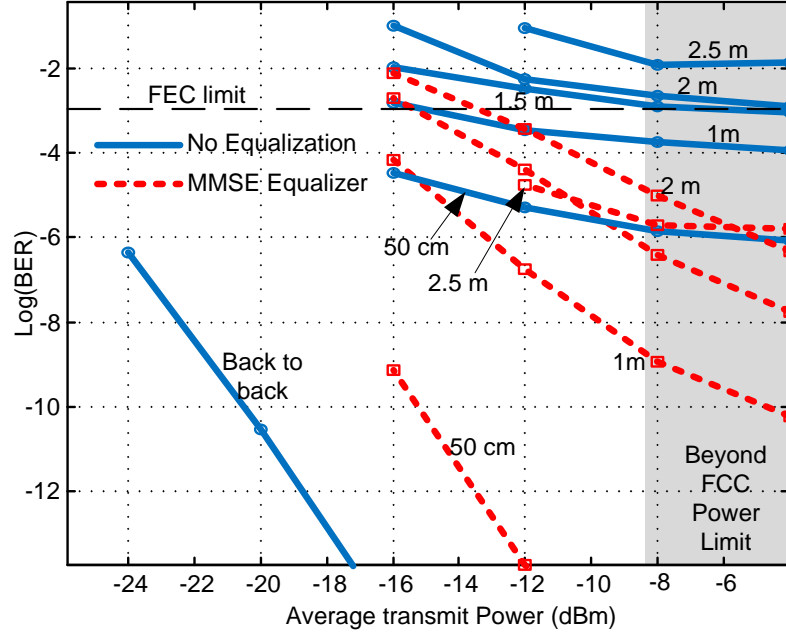


Figure 3.18: BER performance of the receiver with no equalization (solid blue), and with MMSE equalizer (dashed red) are compared for several wireless distances.

small footprint, low cost, and compatibility with electronics fabrication.

In this section, we focus on generation of power-efficient FCC-compliant UWB pulses. Our method is based on frequency-to-time mapping discussed in Section 2.2.2. A generic setup for spectral pulse shaping was presented in Fig 2.4. Instead of using FBG filters we use a silicon-integrated filter. We design a race-track ring resonator (RTR) in silicon-on-insulator (SOI) as a notch filter to shape the output pulses of a gain switched laser. Chromatic dispersion of optical SMF is used for frequency-to-time mapping, under the premise of propagation in a PON [53]. We build an on-chip power splitter and combine the filtered pulses with unfiltered laser pulses in a balanced detection scheme similar to the technique showed in Fig. 2.5. The major difference is replacing the FBG filter with a microring filter. The ring resonator response offers much less tunability compared to the FBG but allows for integration on SOI.

We simulate the microring frequency response in MATLAB after finding the coupling coefficients in a mode-solver (Section 3.4.2). Because of frequency-to-time mapping, the UWB pulse shape depends on the microring spectral response, making the FWHM of the ring filter the main design parameter. We find the ring dimensions from simulation and sketch the chip layout which is later fabricated by UV lithography in a foundry. We use off-the-shelf photodetectors to convert the optical signal to the electrical do-

main. Measured UWB waveform shows good FCC spectral mask compliance and power efficiency when used with a UWB antenna.

Previously reported silicon solutions for UWB pulse generation led to pulses with low power efficiency when respecting FCC regulatory requirements (e.g. monocycle pulse). Silicon photonics solutions include [54], where a laser was phase modulated by an electrical Gaussian pulse and PM-IM conversion was obtained by using the linear resonance region of a micro-ring resonator. Differentiation through the PM-IM process generated Gaussian monocycle pulses with fractional bandwidths of 150%. Exploiting the same principle, three micro-rings were used to obtain the second derivative of the Gaussian pulse, i.e., doublet pulse [55]. Unfortunately, the pulses in [54, 55] were not shaped for power efficiency under FCC regulations. In [56], a laser is modulated by non-return-to-zero data in an intensity modulator. A ring resonator with resonance wavelength tuned to the laser wavelength produces intensity dips and overshoots, depending on the phase of the modulated signal at the input of the ring. Monocycle pulses were obtained by adjusting the ring coupling coefficients.

In another technique, UWB pulses were generated with minimum wavelength dependency using two photon absorption in a silicon waveguide in [57]. The two photon absorption process in the waveguide results in an inversely modulated probe. The pulse pump and the modulated probe are combined after adjusting their relative amplitude and delay. Gaussian monocycle pulses with fractional bandwidth of 154% were generated. Both techniques generated monocycle pulses that are not power efficient vis-à-vis the FCC frequency mask [45].

On-chip optical spectral shaping for arbitrary RF signal generation was shown in an excellent paper in [58]. The spectrum of a mode-locked laser was coupled to a silicon chip with 8 cascaded micro-ring resonators. The resonance wavelength of each ring was controlled by temperature. Building Mach-Zehnder couplers in the through ports of the rings allowed for thermal tuning of the coupling coefficients, and therefore the amplitude of each resonance dip, i.e., the resonance wavelength. This design permits full control over the resonance wavelength and the depth of the resonance dip for the 8 ring resonators. RF pulses were obtained after frequency-to-time mapping and photodetection. The proposed structures allows for generation of highly tunable RF signals, however, the authors did not use their pulse shaper for UWB.

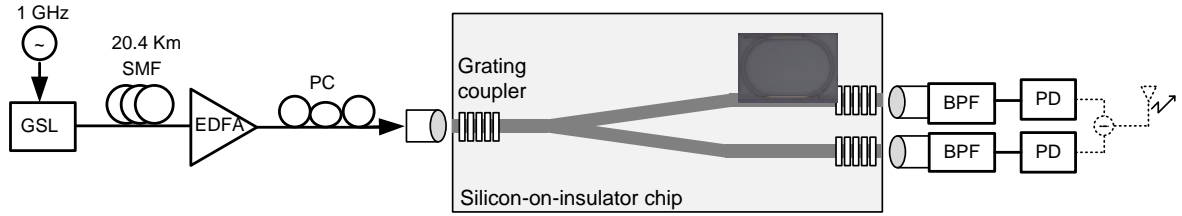


Figure 3.19: The schematic diagram of the experimental setup. Gain-switched laser: GSL, SMF: single-mode fiber, polarization controller: PC, erbium-doped fiber amplifier: EDFA, bandpass filter: BPF, photodetector: PD.

### 3.4.2 Principle of Operation and RTR design

In our method, the pulses are generated directly in the optical domain at the central office for optical transport and the silicon-on-insulator chip is located at customer premises where the signal is converted to the electrical domain after photodetection. Fig. 3.19 shows the block diagram of the proposed UWB pulse generation system.

The central office laser is gain switched by applying a bias current below the lasing threshold in addition to a 1 GHz sinusoidal signal resulting in short pulses, around 25 ps, with a repetition rate of 1 GHz. To overcome coupling losses of our prototype, we amplify pulses after fiber propagation before coupling to the chip. Although we used an erbium-doped fiber amplifier (EDFA) in the lab, in a PON a semiconductor optical amplifier (SOA) is suitable for amplification either as a booster at the central office or as an in-line amplifier.

The state of polarization after fiber propagation is random resulting in polarization dependent loss in silicon wire. Polarization diversity in the chip is necessary to eliminate this loss by splitting the polarization in the fiber into two orthogonal polarizations which can be processed in two identical circuits [59].

Inside the chip, the input is divided into two equal length branches using a power splitter. The splitter was simulated in Lumerical FDTD Solutions. Fig. 3.20a shows the layout of the design. Power profile versus position at the input and output of the splitter is plotted in Fig. 3.20b. We can see that the power at the two output branches are nearly equal.

At the output of the splitter, one of the branches couples to the RTR, whereas the



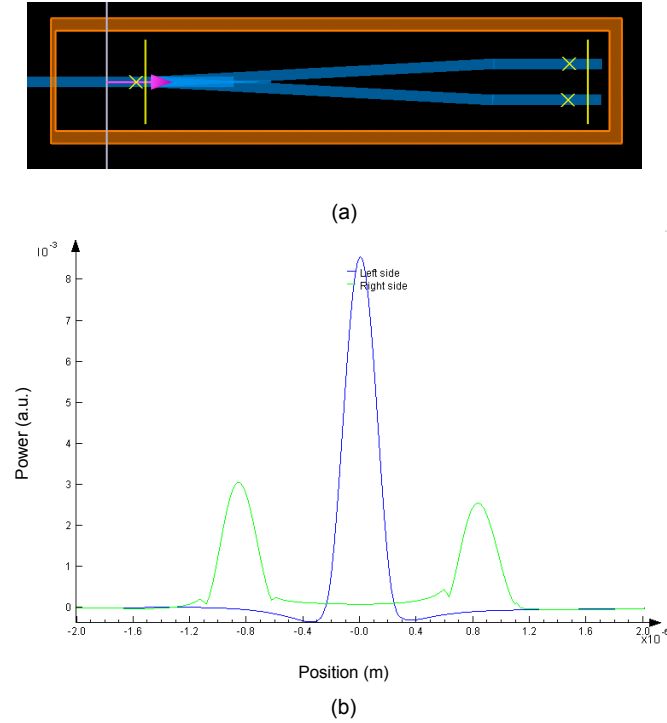


Figure 3.20: Y-splitter. (a) Lumerical layout (b) power versus position, blue curve is at the input and the green is at the output.

second branch connects directly to the output. The resonance wavelength of the RTR is tuned to the center wavelength of the laser. The spectral shape of the pulse at the output of the ring depends on the Q-factor of the RTR, making the Q-factor our main design parameter. Optical intensity being always positive results in pulses with strong low-frequency content. We employ a two-branch structure and balanced photodetection to remove the positive pedestal of the waveform [11].

The output from the chip is filtered by an optical bandpass filter to reduce the amplified spontaneous emission. A photodetector performs the optical-to-electrical (O/E) conversion. Because of experimental difficulty in simultaneously coupling the light out of the two waveguide branches, the output of each branch was separately measured by a sampling scope. In an integrated receiver the photodetectors would be on chip.

The frequency-to-time mapping is a function of the amount of dispersion, which can be introduced by PON transport over fiber and/or by other methods, e.g., by a chirped fiber Bragg grating. Tunable dispersion has been shown in silicon photonics [60]. The length of fiber in PON networks varies by a few kilometers. This variable dispersion changes the duration of the pulse at the antenna. To compensate, we can either use

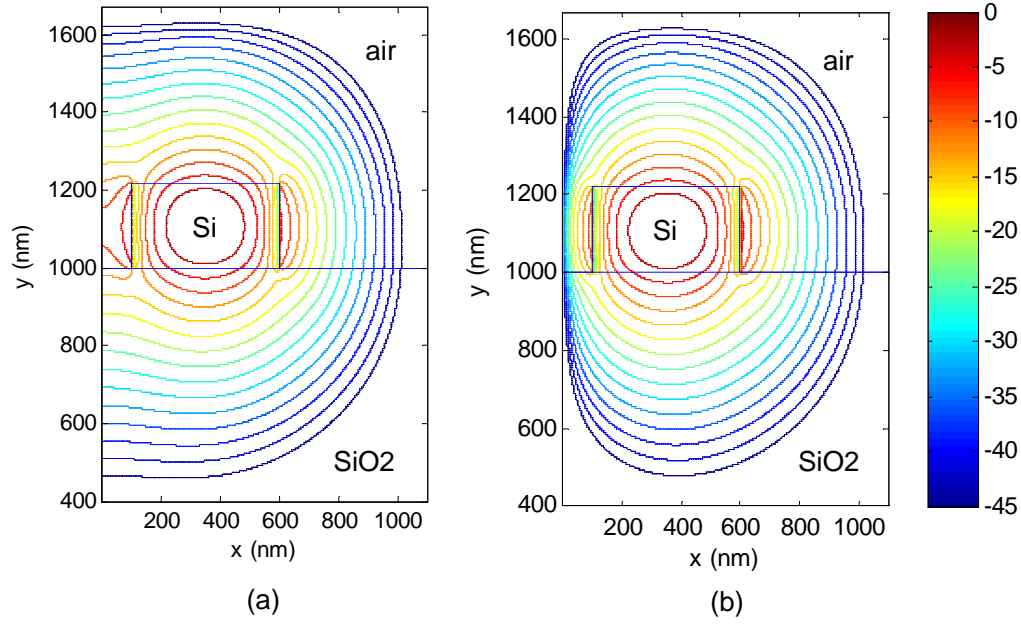


Figure 3.21: The amplitude of the electric field. (a) symmetric supermode, and (b) the anti-symmetric supermode.

dispersion compensation [60], or change the bandwidth of the source to some extent by controlling the current of the laser.

To simulate the transfer function of the RTR, we followed the method presented in [61] and neglected the temperature dependence. The effective indices of the symmetric and antisymmetric supermodes of the coupled waveguides need to be calculated. We simulated the cross section of the waveguides in the WGMODES to find the guided modes [62]. This method is based on 2D finite difference by solving the Maxwell equations on a meshed cross section. Fig. 3.21a shows the amplitude of the electric field symmetric supermode for a waveguide width of 500 nm and a gap width of 200nm. The mesh grid size was set to 2.5 nm by 2.5 nm for a good accuracy. The anti-symmetric supermode is shown in Fig. 3.21b. The mode analysis also result in the effective indices of the guided modes. Fig. 3.22a plots the effective indices of the symmetric and anti-symmetric modes versus the wavelength. The difference of the two indices is plotted in Fig. 3.22b. The crossover length,  $L_{CR}$ , is the length where all the power from one waveguide is transferred to the coupled waveguide. The crossover length can be found

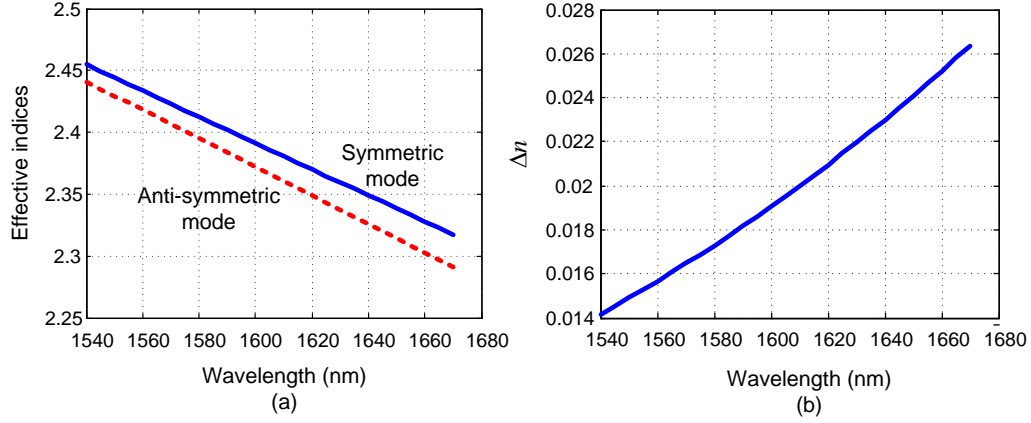


Figure 3.22: (a) the effective indices of the symmetric and antisymmetric supermodes, and (b) the difference of the two indices.

from the difference between the effective indices of the two supermodes,  $\Delta n$ ,

$$L_{CR} = \frac{\lambda}{2\Delta n} \quad (3.18)$$

$$= \frac{\pi}{2C(\lambda)} \quad (3.19)$$

where  $C$  is the coupling coefficient and  $\lambda$  is the wavelength. The coupling coefficient shows a strictly exponential behavior as a function of the coupler gap [61]

$$C(\lambda) = B(\lambda)e^{-A(\lambda).L_{gap}} \quad (3.20)$$

where  $L_{gap}$  is the space between the waveguides in the coupler. Parameters  $A$  and  $B$  are found by solving a nonlinear least squares problem in MATLAB to best fit the exponential function to  $C(\lambda)$  in a certain gap width range. Having  $A$  and  $B$ , we can use (3.20) to find the coupling coefficient for any gap width  $L_{gap}$ .

The field transmission coefficient,  $t(\lambda)$ , between the two coupled waveguides is

$$t(\lambda) = \cos(B(\lambda).L_c e^{-A(\lambda).L_{gap}}) \quad (3.21)$$

where  $L_c$  is the coupler length. The round trip phase shift in the RTR is

$$\delta(\lambda) = 2\pi \frac{n_{eff}.L_{RTR}}{\lambda} \quad (3.22)$$

where  $L_{RTR}$  is the circumference of the RTR. We have considered a constant effective index throughout the RTR by neglecting the index change in the bent segments. The through port power transmission function of the RTR can be expressed as

$$S_{21}(\lambda) = \frac{t_1 - t_2 a e^{j\delta}}{1 - t_1 t_2 a e^{j\delta}} \quad (3.23)$$

Table 3.2: Design Parameters

Parameter	Value
loss coeff.	10 dB/cm
Gap width	200 nm
Coupling length	20 $\mu m$
Ring radius	20 $\mu m$
$t_1$	0.82
$t_2$	0.82
L	21 km

where  $t_1$  and  $t_2$  are the transmission coefficients of the add and drop ports, respectively, and  $a$  is the round trip field loss coefficient. The drop port is not used in our pulse shaper and is tapered down to dissipate its power. We adjust the resonance bandwidth by adjusting the through port gap width, the drop port gap width, and the coupling length. The resonator is designed near the critical coupling condition to have a good extinction ratio.

To determine proper RTR dimensions, we simulate our setup (Fig. 3.19) and find the output pulses to be

$$p_1(t) = \left| \mathcal{F}^{-1} \left\{ s(\omega) S_{21}(\omega) e^{-j\beta_2 \omega^2 L/2} \right\} \right|^2 \quad (3.24)$$

$$p_2(t) = p_1(t)|_{S_{21}(\omega)=1} \quad (3.25)$$

where  $p_1(t)$  and  $p_2(t)$  are the photodetector output pulses at filtered and unfiltered branches, respectively. The angular frequency is  $\omega$ ,  $s(\omega)$  is the source spectrum,  $\beta_2$  is the group velocity dispersion (GVD) parameter,  $L$  is the SMF length, and  $\mathcal{F}^{-1}$  is the inverse Fourier transform. The UWB pulse is  $p(t) = p_1(t) - p_2(t)$ .

We assume a loss coefficient of 10 dB/cm in the waveguide and vary the dimensions of the micro-ring to find  $p(t)$  with best spectral response under the FCC mask. The design parameters chosen to generate a UWB pulse are waveguide width of 500 nm, 20  $\mu m$  ring radius, 20  $\mu m$  coupler length, and 200 nm gap width, resulting in  $t_1 = t_2 = 0.82$  at the laser wavelength. Table I lists the simulation parameters chosen to generate a UWB pulse.

Fig. 3.23 shows the simulated PSD of the gain-switched laser before and after the

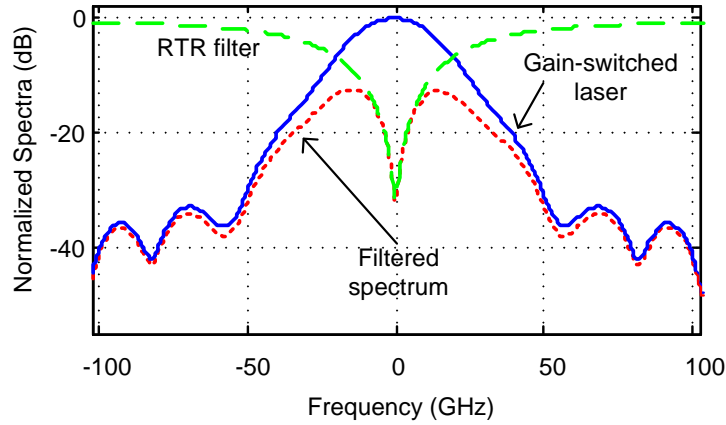


Figure 3.23: Simulation result for filtering the gain-switched laser with the RTR notch filter.

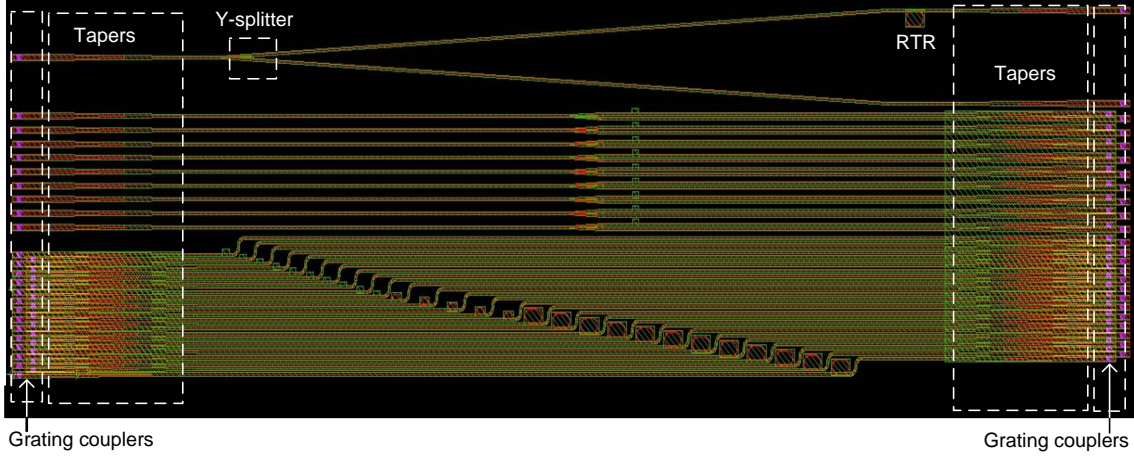


Figure 3.24: The design layout from DW-2000 software.

RTR filter. The frequency chirp of the source is mostly linear and can be compensated by adjusting the fiber length [41]. We do not consider the chirp of the laser pulse in the simulation. The Q factor of the RTR determines the spectral shape of the through port (dotted red). The resonance frequency is tuned to the center of the laser frequency.

The physical layout of the device was sketched using the DW-2000 (Fig. 3.24). We fabricated 36 RTRs with varying dimensions, given the uncertainties in the fabrication process. The chip was fabricated with 193 nm photolithography by ePIXfab at IMEC. It featured a 220 nm thick Si film on top of 2000 nm of buried oxide, SiO<sub>2</sub>. A picture of the fabricated chip is shown in Fig. 3.25a. The region allocated to our design is highlighted by a red box. Fig. 3.25b shows a scanning electron microscope (SEM)

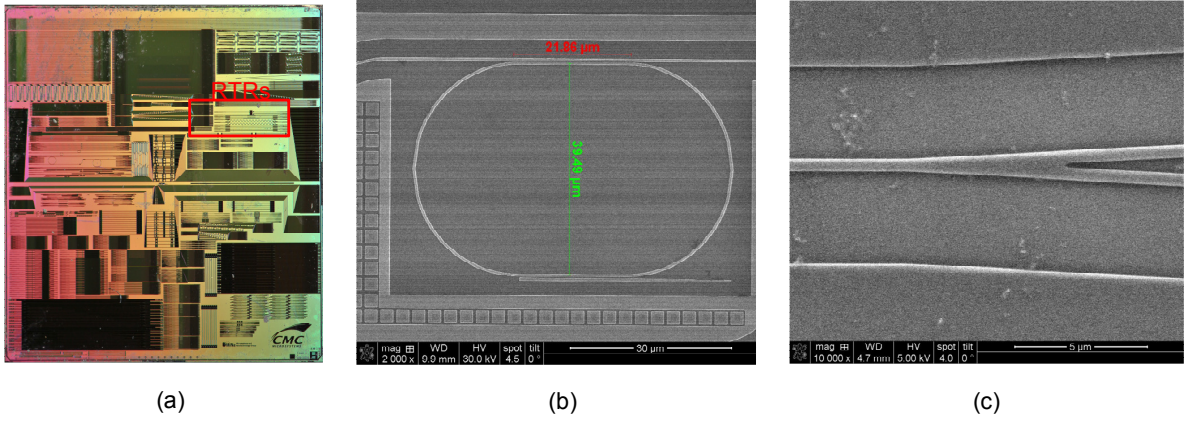


Figure 3.25: (a) picture of the fabricated chip; the portion dedicated to our design is indicated by a red box, (b) a scanning electron microscope (SEM) image of an RTR, and (c) the SEM image of the Y-splitter.

image of an RTR and Fig. 3.25c shows an SEM image of the splitter.

### 3.4.3 Experimental Results and Discussion

The light is coupled in and out of the chip by vertically holding the fiber with a  $10^\circ$  tilt, allowing for better coupling. We observed around 20 dB of coupling loss. Instead of putting a heater on the chip to tune the RTR resonance, for experimental convenience we tune the laser emission wavelength with a temperature controller.

Fig. 3.26 shows the measured transmission response of the RTR as captured by optical frequency-domain reflectometry (OVA Luna Technologies). There is some mismatch between measurement and simulation due to fabrication imperfections. For a better match, we readjust the design parameters to gap width of 230 nm and waveguide width of 450 nm. This can be the result of decreased wire width due to proximity effects during lithography [63]. The simulation (dotted blue) closely follows the measurement (solid red) after making these parameter adjustments (Fig. 3.26). The free spectral range (FSR) is 3.2 nm and the calculated Q-factor  $\sim 5000$ .

Fig. 3.27a plots the waveforms after frequency-to-time mapping and O/E conversion by photodetection. We observe that the filtered pulse shows a notch in its temporal shape, i.e., the spectral notch has been mapped to the time domain. The unfiltered gain-switched laser, passing only through the silicon waveguide, is also photodetected

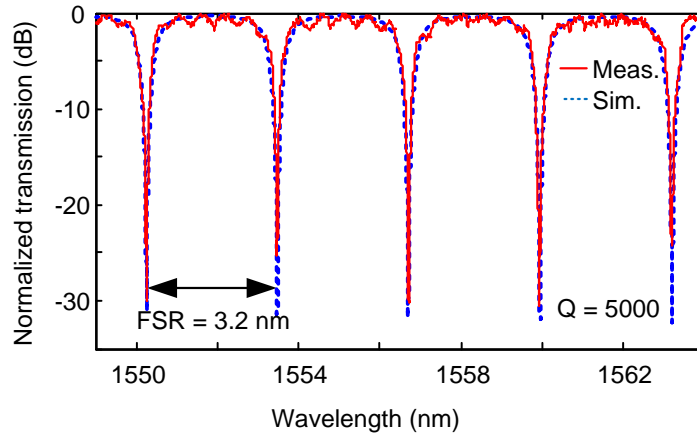


Figure 3.26: Simulated (dotted blue) and measured (solid red) transmission response of the RTR.

and plotted in Fig. 3.27a. We obtain the UWB pulse by subtracting the two waveforms with proper amplitudes. The simulation result and the measurement closely match.

Fig. 3.27b shows the PSD of the UWB pulse versus the FCC spectral mask. To find the EIRP, we consider the SkyCross SMT-3TO10MA UWB antenna. The antenna gain is measured and multiplied by the PSD of the pulse to obtain the EIRP. The EIRP of the simulated and measured UWB waveforms have good compliance with the FCC spectral mask (Fig. 3.27b). The power efficiency of the pulse is 52%, which is significantly higher than the 40% efficiency reported for the Gaussian fifth derivative [45].

## 3.5 Conclusion

In this chapter we proposed and demonstrated experimentally three low-cost optical UWB pulse generation methods.

First, a gain-switched laser was used at a repetition rate of 856 MHz. The pulses were dispersed by propagation through a length of fiber. An MZM was used at its quadrature bias point to multiply the pulses with a 6.85 GHz sinusoidal signal, upconverting the pulses to the center of the FCC spectral mask. A differential photodetection scheme removed the low-frequency components. The optical fiber was replaced by an FBG filter to make a compact optical UWB transmitter. The generated UWB pulse showed



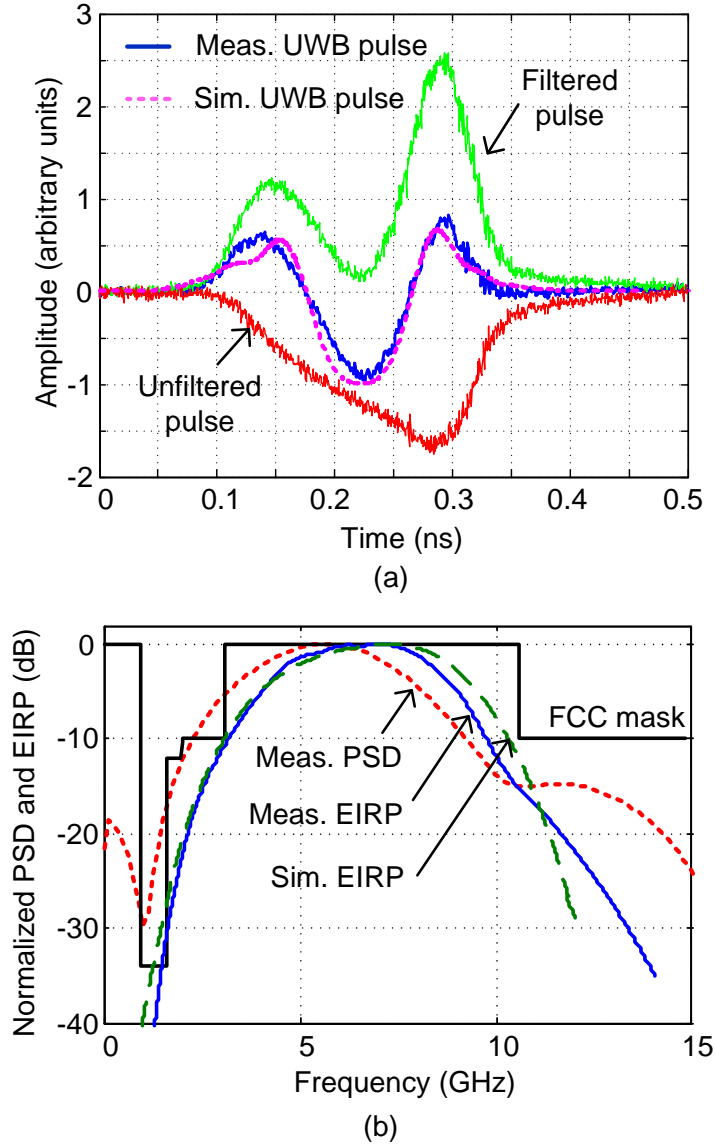


Figure 3.27: The generated UWB waveforms. (a) The time domain waveforms for the filtered and unfiltered branches, and the resulting UWB pulse. (b) The PSD and the calculated EIRP of the UWB pulse. Simulation results match the experiment.



a good FCC spectral mask compliance, with a power efficiency of 42%. We showed good power efficiencies for distances between 15 km and 25 km. Moreover, the use of an MZM as the pulse shaping device promises future optical on-chip silicon UWB transmitters.

Wireless propagation of the UWB impulses was investigated by offline signal processing. A linear receiver and an energy detector were implemented. The linear filter showed a better BER performance, particularly in distant channels. We could still reach the FEC limit of  $10^{-3}$  after 3.5 m of wireless propagation.

Secondly, a combination of data and a sinusoidal signal was used to generate BPSK UWB pulses at a bit-rate of 1.75 Gb/s. A CW laser, a Mach-Zehnder modulator, and a photodetector were the only optical components in this technique. Fiber propagation caused no significant degradation to the pulses, validating use of such systems in PONs.

Antenna transmission measurements and EIRP calculations were reported. Bit error rate performance of a linear receiver was investigated by offline signal processing. We could reach the FEC limit of  $10^{-3}$  after 2.5 m of wireless propagation by employing an MMSE equalizer.

Finally, gain-switched laser pulses were spectrally filtered by a micro-ring resonator. SMF propagation performed the frequency-to-time mapping and balanced photodetection removed the low frequency components of the generated RF signals. UWB pulses generated by this method showed good power efficiency (52%) while respecting the FCC spectral mask. Further integration of a modulator and photodetectors on the same chip can result in a practical compact UWB transmitter for high speed indoors data communication.

# Chapter 4

## UWB pulse shaping: bypassing the limitations of the monocycle

The most common UWB pulses discussed in the literature are the Gaussian monocycle and its higher order derivatives. Although traditionally employed for UWB systems, these shapes poorly exploit the permissible power under the FCC mask. Among many examples of monocycle pulse generation techniques in the literature, we can refer to recent works in [64] and [65], as electrical and optical ways of UWB pulse generation. A common argument is that when a Gaussian monocycle pulse is transmitted by a UWB antenna, the passband behavior of the antenna will modify the pulse spectrum and improve somewhat its power efficiency vis-à-vis the FCC mask.

In this chapter, we show that even in case of the Gaussian 5<sup>th</sup> derivative pulse, inherently superior to the Gaussian monocycle pulse in terms of meeting the FCC mask, the power efficiency is less than that of optimally designed pulses. Another way of improving the efficiency of the monocycle is filtering it with a highpass filter (HPF). While a HPF improves monocycle power efficiency it still under performs compared to shaped pulses. Moreover a HPF with a fast roll-off results in longer temporal pulses, causing more intersymbol interference at high bit-rates.

We briefly discussed a UWB waveform generator based on FBGs in Section 2.2.2. In this chapter we use a similar but more versatile setup, programmable by temperature tuning for efficient and high precision pulse shaping [3]. We use this method to produce all pulse shapes examined experimentally in this chapter.

Ultra-wideband antenna design has been an active area of research for the antenna community. Many different antenna structures, mainly on PCB, have been proposed. The impulse response of any antenna distorts the UWB pulses. In order to highlight the advantage of pulse shaping over using monocycle pulses and to investigate challenges imposed by antennas, we consider three antennas with different bandpass characteristics: the commercial SkyCross UWB antenna, the circular monopole antenna [66], and the monopole antenna with two steps [67].

The evaluation in realistic systems is important, as there is the perception that failings in the pulse shape (especially for the monocycle) can be compensated by simple highpass filter and the bandpass nature of the UWB antenna. We fabricate and characterize two UWB antenna designs available in the literature, as well as one commercial antenna. We use our optical pulse shaping device to experimentally investigate three different pulse shapes and measure their transmitted power spectral density with each of the UWB antennas. We find that the monocycle is significantly less power efficient than the others. Combining the monocycle with a highpass filter is efficient, but transmit power is still several dB below that of shaped pulses. The fine pulse shaping available in optical processing provides 1.7 to 2.9 dB gain over the electrical processing methods, depending on the antenna used. Electrical and optical pulse shaping techniques offer significant opportunities to improve over the monocycle.

In [11], the gain response of the SkyCross antenna was incorporated into an optimization process, resulting in very efficient pulses in terms of EIRP. The limitations existing in the linear optimization method, however, do not allow optimal pulse design in the general case where the antenna may introduce severe distortion (one of the three cases we will examine). To treat these cases, we use a hybrid optimization process of the genetic algorithm and a sequential quadratic program (SQP) [45]. In this method, we build the UWB waveforms by combining the Gaussian monocycle and its higher order derivatives. In contrast to the linear optimization method, we optimize not only the weights, but also the delays, the FWHM pulse width and the derivation order.

While we optimize the transmit power, ultimately BER is key. BER advantages of UWB pulse design was examined in [68] for multiple access UWB systems. It was shown that a sinc pulse optimizes the signal-to-noise-plus-interference ratio of the UWB system and achieves better BER performance when corrupted by multiple access interference. Generation of the pulse and antenna distortion was not addressed in this work. Simulation results in [69] showed that UWB waveforms with high power efficiency have

improved the BER performance, especially for small distances. We consider a linear receiver and compare the BER performance of our designed pulse with the Gaussian fifth derivative and the Gaussian monocycle. Simulation results show significant pulse shaping advantage is observed under both AWGN and multipath channel conditions.

## 4.1 UWB Pulse Design

In this section, we design efficient UWB waveforms that achieve high spectral efficiency values while their EIRP respects the FCC spectral mask.

To obtain transmitted EIRP we use similar antennas at transmitter and receiver and measure the channel frequency response using a network analyzer. Using the Friis free space transmission formula (2.2) an effective spectral mask can be defined for a given antenna [11]. The power spectral density of the UWB pulse should respect the effective mask instead of the FCC mask. Note that the effective mask is antenna dependent. We use two different optimization methods to maximize the total average power under the newly defined mask for each of the three antennas we will examine.

A linear optimization method was proposed in [17] for use with the FCC mask, and was later used with the effective spectral mask in [11]. The optimal pulse is synthesized using a digital finite impulse response (FIR) filter structure. In [11], the optimization problem was solved using the Matlab SeDuMi optimization tool [70].

In general, the linear optimization method finds a better fit to the mask by increasing the number of taps. However, being limited to optimizing only the weights of the monocycle pulses, this method does not necessarily result in a best fit. In [45], we used a hybrid optimization based on the genetic algorithm and SQP. We synthesize a pulse as

$$x(t) = \sum_{k=0}^{L-1} w[k] g_k(t - T_k), \quad (4.1)$$

where  $\{w[k]\}_{k=0}^{L-1}$  are the filter tap coefficients and  $g_k$  can be the Gaussian monocycle pulse or one of its higher order derivatives. Each Gaussian pulse can have a different FWHM ( $\tau(k)$ ). The delay between the Gaussian pulses,  $T_k$ , is also a variable. Therefore, the pulse is synthesized with many more degrees of freedom compared to the linear optimization method. The use of higher order derivatives is significant in the

optimization as differentiating a Gaussian pulse shifts its spectrum towards the higher frequencies. Intuitively, different derivation orders in the summation (4.1) explore different frequency regions over the UWB bandwidth.

The optimization problem is stated as

$$\begin{aligned} & \max \int_{F_p} |X(f)|^2 df, \quad f \in F_p \\ & \text{subject to } |X(f)|^2 \leq M(f), \quad f \in F_p \end{aligned} \quad (4.2)$$

where  $X(f)$  is the Fourier transform of  $x(t)$ . This problem leads to a nonlinear, non-convex optimization with many variables. This type of optimization problem is generally difficult to solve, and we turn to the genetic algorithm (GA). The fitness function is the integral in (4.2). The population size is set to 200 and the algorithm continues subject to a certain error tolerance. The output from the GA is used as the initial point in the SQP in the MATLAB optimization toolbox. This nonlinear constrained optimizer improves the results obtained from the GA. In the next section we will use this method to find optimal pulses under different effective masks (*i.e.* different antennas).

## 4.2 Common UWB pulse shapes

Traditionally the Gaussian pulse and its derivatives are adopted as UWB waveforms. The commonly used Gaussian monocycle, the filtered monocycle and the Gaussian fifth derivative are shown in Fig. 4.1. The amplitude of the pulses are adjusted so that their spectra comply with the FCC mask. To obtain the filtered monocycle, a highpass filter attenuates the low frequency contents of the monocycle pulse. We simulate the filter as a perfect bandpass for frequencies larger than 3.1 GHz and a Gaussian filter with 30 dB insertion loss in 1 GHz offset (*i.e.* at 2.1 GHz) for frequencies smaller than 3.1 GHz. Before antenna transmission, the power efficiency of the Gaussian monocycle, the filtered monocycle, and the Gaussian fifth derivative are 1%, 12% and 40%, respectively. While common wisdom is that a Gaussian monocycle combined with a passband antenna response can boost the power efficiency of the monocycle over the FCC mask, this approach is far from optimal. Even when using the Gaussian fifth derivative pulse, the passband antenna cannot provide the same level of power efficiency as a pulse shaped to adapt to the antenna response and sculpted to match the FCC mask.

In the next section we design unique UWB pulses for three different UWB antennas

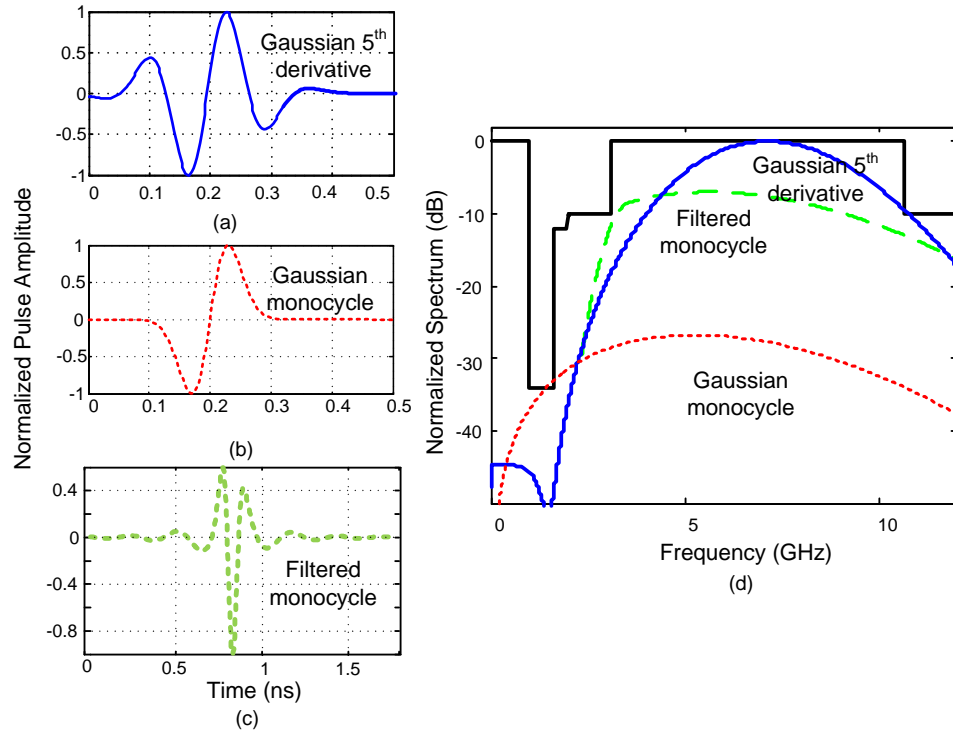


Figure 4.1: Commonly used UWB pulses. (a) the Gaussian 5th derivative, (b) the Gaussian monocycle, (c) a highpass filtered gaussian monocycle pulse, and (d) the corresponding spectra with respect to the normalized FCC spectral mask.

that efficiently exploit the FCC spectral mask. We show that these pulses achieve much higher power efficiencies than the Gaussian derivatives.

### 4.3 Antennas and Efficient UWB Pulses

For high data-rate indoor applications the antennas are required to be omni-directional and small. Printed circuit board (PCB) antennas are great candidates for UWB antennas. Ideally, a UWB antenna should have a flat frequency response from 3.1 to 10.6 GHz but unfortunately this is not attainable. The frequency response of the antenna distorts UWB pulses.

To measure the antenna frequency response, two similar antennas are used for LOS transmission in a lab environment over a distance of 65 cm and a height of 120 cm. The antennas are placed in their peak radiation direction in the azimuth plane. For these

antennas, the azimuth was the direction of greatest gain. The channel response,  $S_{21}(f)$ , is measured by a vector network analyzer. The VNA captured 6401 points across a span of 0.2 to 12 GHz and averaged 16 times to improve the dynamic range. Observation of the channel over longer periods of time showed no variations in the response [45].

Prior to transmission we use a power amplifier with an average gain of 25.7 dB over the bandwidth of interest. The frequency response,  $S_{21}(f)$ , is measured for antenna plus amplifier using the VNA. This response is used to compensate for the distortion caused by the amplifier. EIRP of the transmit pulse is calculated using the method explained in 3.1.

In this section, we choose three typical UWB antennas. We use the same technique to characterize each antenna and present results from the characterization in the following sections, each devoted to a separate antenna. An efficient pulse is designed for each antenna after finding the corresponding effective masks. We will compare the performance of these optimally designed pulses with the Gaussian monocycle and the Gaussian 5<sup>th</sup> derivative pulse.

### 4.3.1 The SkyCross Antenna

The commercial 3.1-10 GHz omni-directional SkyCross SMT-3TO10MA antenna is shown in Fig. 4.2a. This antenna has small size and is azimuth omni-directional, with a -10 dB bandwidth from 3.7 to 9 GHz. Fig. 4.2b shows the measured frequency response of the antenna. The antenna passes the entire UWB bandwidth, but has a non-flat response. Based on the measured frequency response, the effective mask is calculated and shown in Fig. 4.2c. An efficient UWB pulse is designed using the linear optimization method [45]. We use 8 taps in (4.1), and  $T_0$  and  $\tau$  are 38.5 and 58.5 ps, respectively. The nonlinear optimization program results in a similar pulse for this antenna. The EIRP closely respects the FCC spectral mask (Fig. 4.2c). The power efficiency is 70%. The pulse in the time domain is plotted in Fig. 4.2d.

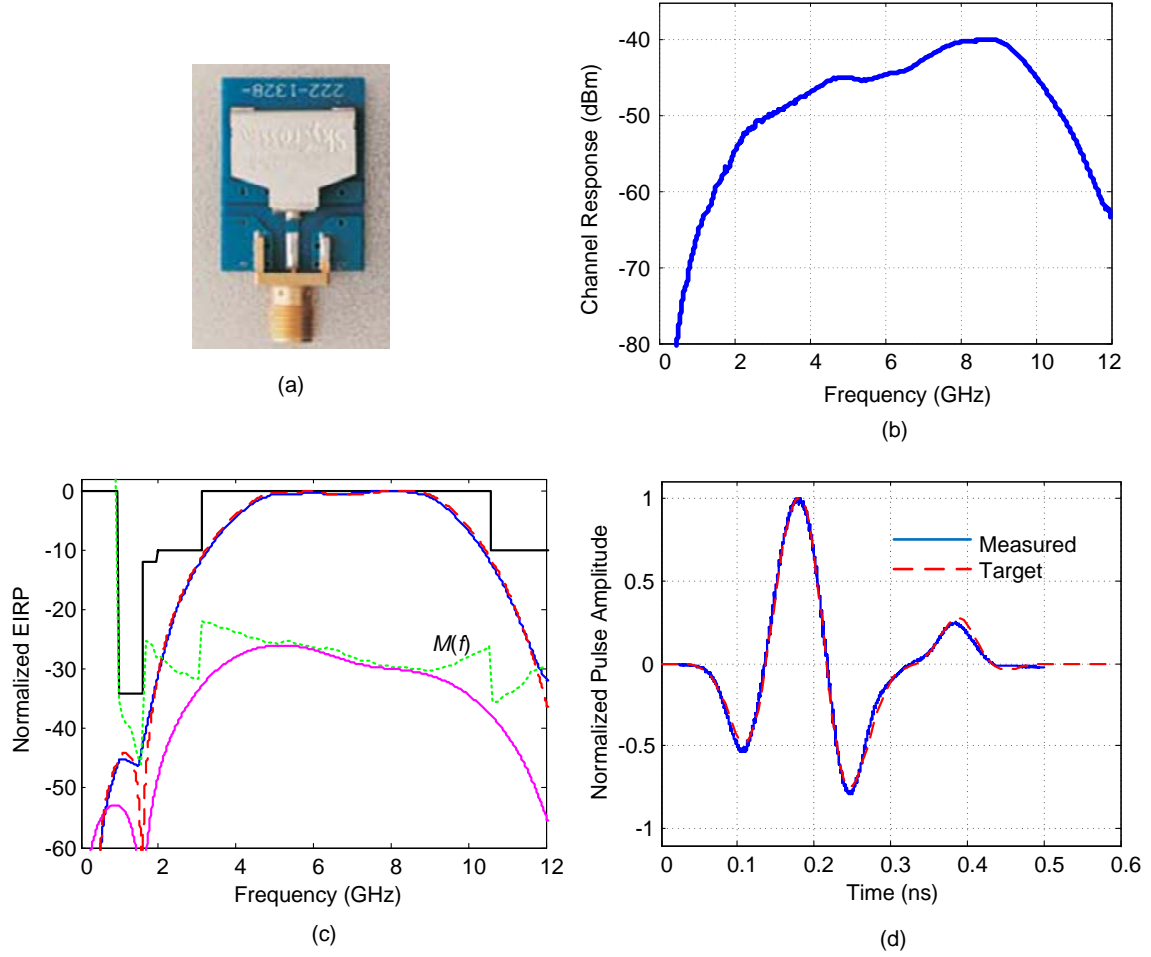


Figure 4.2: (a) The SkyCross antenna structure, (b) the measured channel frequency response, (c) the effective mask (dotted, green), the normalized EIRP-optimized pulse spectral density (target in dashed red, and measured in solid blue), and (d) the normalized EIRP-optimized pulses in the time domain (target in dashed red, and measured in solid blue).

### 4.3.2 The circular monopole antenna

The circular disc monopole antenna was first proposed in [71]. It is a printed antenna fed by a  $50\ \Omega$  microstrip line. The antenna is fabricated on the FR4 substrate with a thickness of 1.5 mm and has a dimension of  $50 \times 42$  mm. The antenna is designed with a partial ground at the opposite side of the monopole. The length of the ground plays a crucial role in matching of the antenna and has to be carefully optimized. The transfer function of this type of antenna was studied in [66], and at boresight it has a notch at high frequencies due to degradation of the antenna pattern.



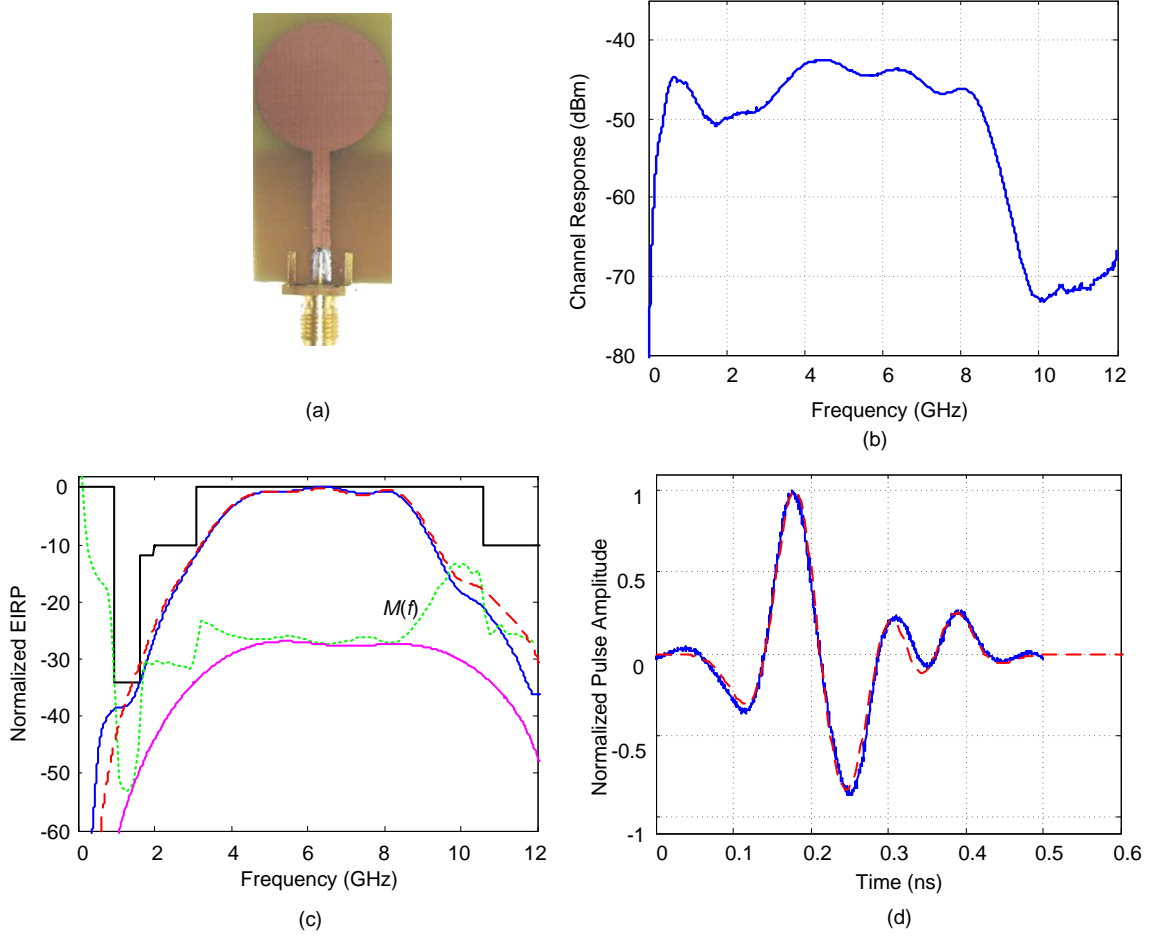


Figure 4.3: (a) the circular monopole antenna, (b) the measured channel frequency response, (c) the effective mask (dotted, green), the normalized EIRP-optimized pulse spectral density (target in dashed red, and measured in solid blue), and (d) the normalized EIRP-optimized pulses in the time domain (target in dashed red, and measured in solid blue).

In [66] reducing the size of the substrate is proposed to leave only a small gap between the radiator and the substrate edges. This smaller antenna shows more omnidirectionality at high frequency and does not have the mentioned notch. We fabricated an antenna to these specifications. The antenna is shown in Fig. 4.3a. Fig. 4.3b shows the measured frequency response of the antenna. The frequency response covers up to 9 GHz. The effective mask is found and the nonlinear optimization program is used to design an efficient UWB pulse [45]. The pulse is shown in the frequency domain (Fig. 4.3c) and in the time domain (Fig. 4.3d). We achieve  $PE = 58\%$ . Higher power efficiencies are possible by increasing  $L$  in (4.1), but imply more complicated pulses in the time domain.

### 4.3.3 The monopole antenna with two steps

The monopole antenna with two steps and a circular slot, proposed in [67], follows the same principles as the circular monopole antenna, and was fabricated in house. The antenna is shown in Fig. 4.4a. The antenna has a return loss less than -10 dB from 3 to 11.4 GHz. Fig. 4.4b shows the measured frequency response of the antenna. We can see that the frequency response is limited to below 7 GHz and does not cover the entire UWB bandwidth. This is due to pattern degradation at high frequencies.

The effective mask for this antenna is shown in Fig. 4.4c. The effective mask emphasizes the response from 7 to 10 GHz, where the antenna suffered a notch in the frequency response. The nonlinear optimization program is used to find a power efficient UWB pulse for  $L = 8$  in (4.1). The optimization results in a combination of two monocycles, five doublets and a fourth-order derivative of the Gaussian pulse [45]. The Gaussian monocycle  $\tau$  varies between 60 to 77 ps. The delay coefficients,  $T_k$ , vary from 10 to 37 ps. The spectrum of the resulting pulse is plotted in Fig. 4.4c. The obtained power efficiency is 60%.

Note that the linear optimization program is not capable of following the effective mask for this antenna. The linear optimizer only reaches  $PE = 47\%$ . The results for the linear optimizer do not improve even by increasing the number of taps,  $L$ , to 100, whereas we can enhance the result of the nonlinear optimizer by increasing  $L$ . Therefore, the nonlinear optimization is a powerful tool to find efficient UWB pulse under sever distortion. The resulting pulse in the time domain (Fig. 4.4d) has an acceptable complexity.

## 4.4 Experimental Validation

### 4.4.1 Pulse Generation

One of the main reasons of wide use in the literature of simpler UWB waveforms is that generation of the custom designed waveforms is complex and costly. To generate the designed UWB waveforms for each antenna, we use the programmable version of the optical pulse shaper introduced in Section 2.2.2.

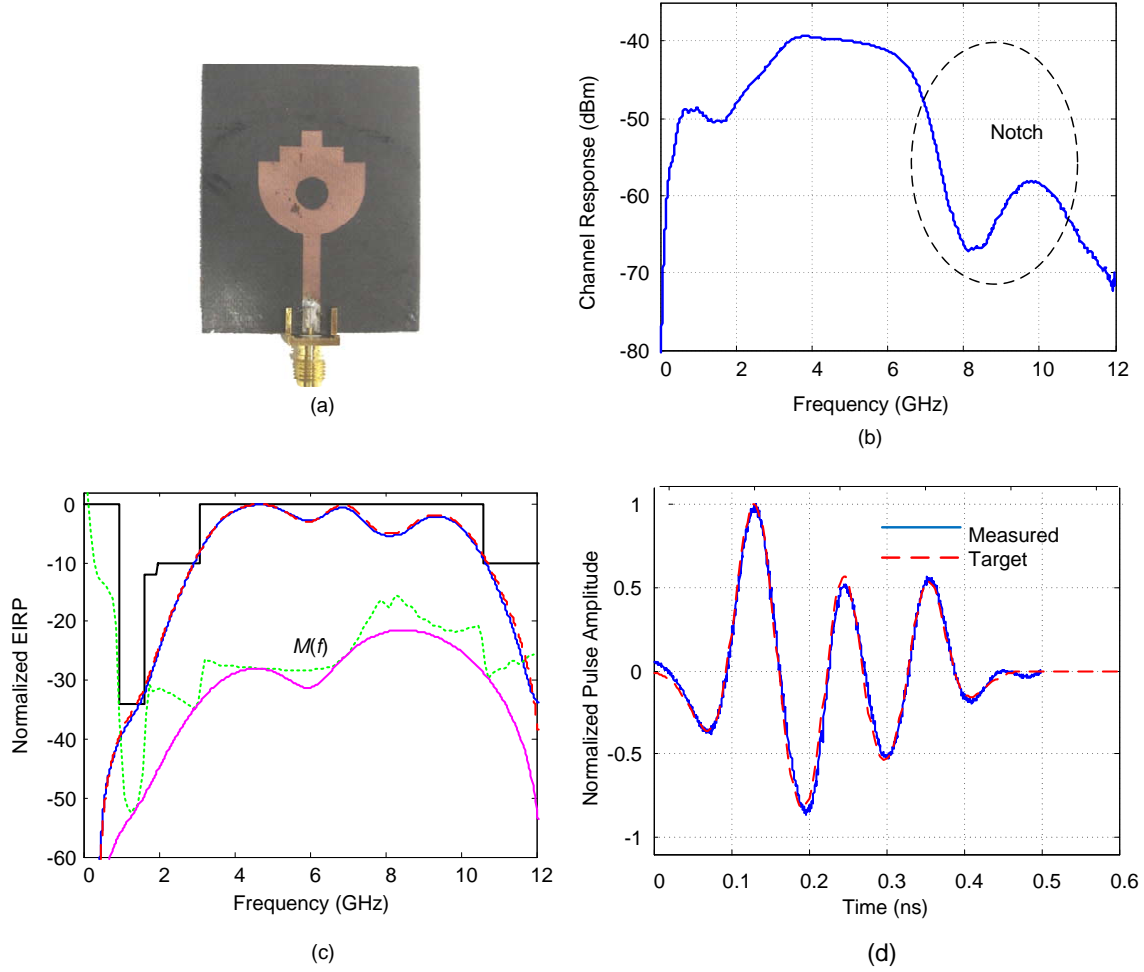


Figure 4.4: (a) the monopole antenna with two steps, (b) the measured channel frequency response, (c) the effective mask (dotted, green), the normalized EIRP-optimized pulse spectral density (target in dashed red, and measured in solid blue), and (d) the normalized EIRP-optimized pulses in the time domain (target in dashed red, and measured in solid blue).

Fig. 4.5 shows the block diagram of the programmable UWB pulse generator designed by M. Abtahi at Laval University [3, 11]. The UWB pulses are generated in the optical domain using spectral pulse shaping and frequency-to-time conversion and then converted to RF using a balanced photodetector. A DFB source gain-switched by a sine wave forms our GSL source of short pulse. Our pulse shaping device consists of two fiber gratings with constant transmittivity placed in contact with two series of resistive heating elements (HEs). The temperature perturbations by the HEs along the chirped FBG (CFBG) elevate the refractive index and change the grating period, which results in a change in the FBG transmittivity, *i.e.* spectral shape [3]. The spectrally shaped

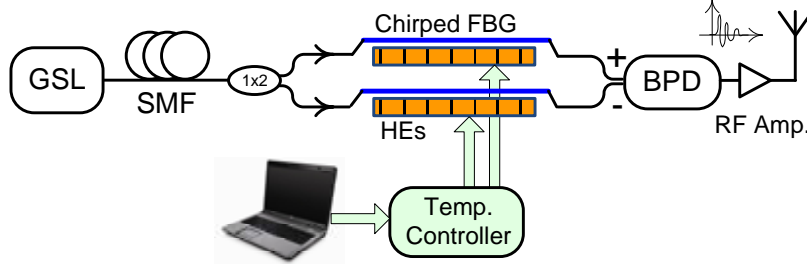


Figure 4.5: The schematic diagram of the arbitrary UWB waveform generator. GSL: gain switched laser, SMF: Single mode fiber, BPD: balanced photodetector, FBG: fiber Bragg grating, HE: Heating element, [3].

pulse is sent to a length of SMF, to perform frequency-to-time mapping.

We sought a temperature set to achieve a target UWB waveform. We first simulate the FBG behavior due to the temperature perturbations using coupled-mode theory. The optimum temperature set is then found via a genetic algorithm minimizing the total error between target waveform and simulation. Using the temperature sets corresponding to each desired UWB waveform, a processor activates the temperature control unit and applies the appropriate voltage to HEs. The generated UWB signal is then amplified and transmitted via the wideband antenna.

The repetition rate in our setup was set to 1 Gb/s. We used 21 HEs in each arm with 2.5 nm width and 0.5 nm separation. We used about 17 km of SMF to disperse the generated short pulse to the required length.

#### 4.4.2 Pulse characterization

The time domain waveforms are measured by a 40 GHz sampling scope (Agilent 86100A). Comparing the designed pulse (dashed line) with the measured pulse (solid line) in Fig. 4.2c, Fig. 4.3c, and Fig. 4.4c, we see an almost perfect match for all three antennas. The EIRP calculated from the measurements is plotted solid blue. The EIRP from each of the antennas fully respects the FCC spectral mask and closely follows the target EIRPs (dashed red). The high precision and controllability of our pulse generation method is apparent in the experimental results.

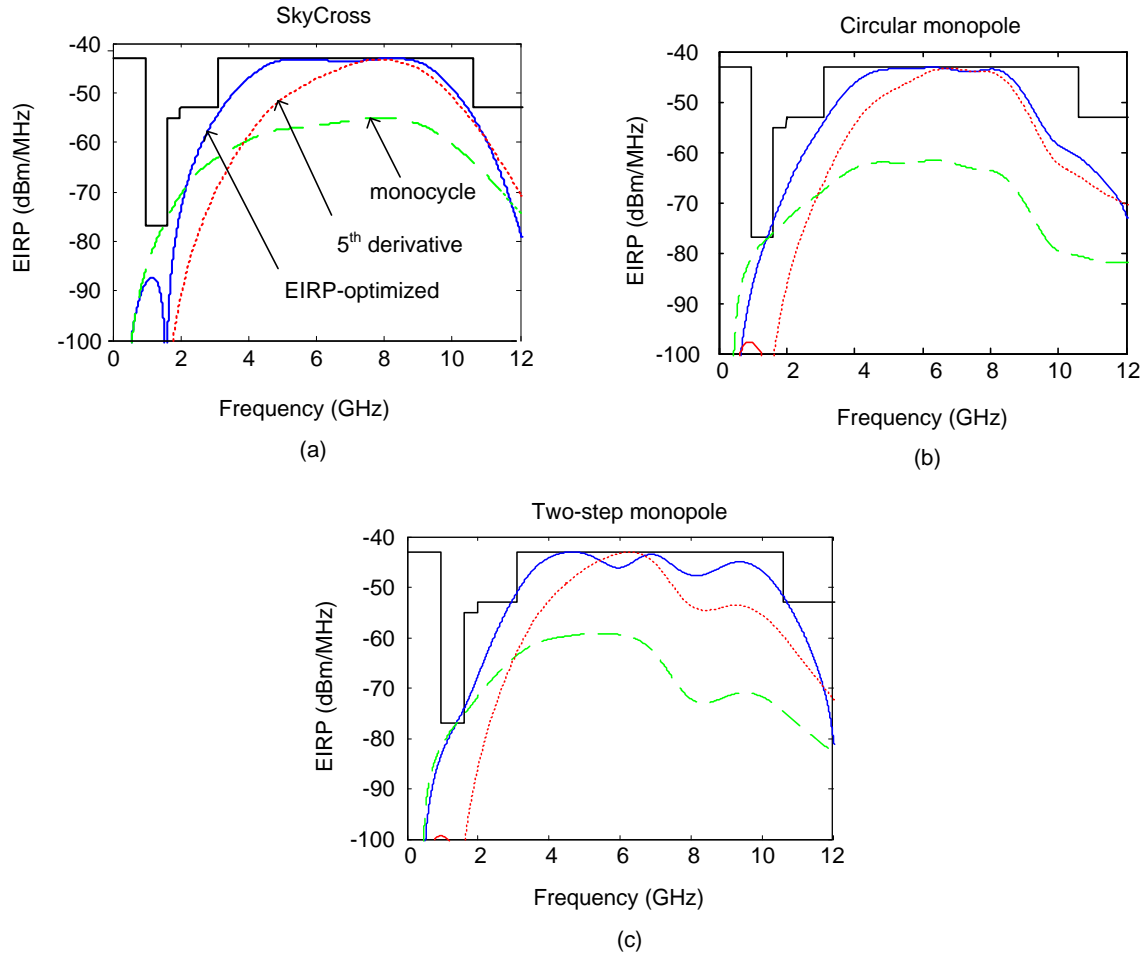


Figure 4.6: The EIRP-optimized pulse (solid, blue) and the Gaussian 5<sup>th</sup> order derivative (dotted, red) (3), and the Gaussian monocycle pulse (dashed, green); for (a) the SkyCross, (b) the circular monopole, and (c) the monopole antenna with two steps.

## 4.5 Simulation Results and Discussion

Fig. 4.6 compares the Gaussian monocycle, the Gaussian 5<sup>th</sup> derivative and the EIRP-optimized pulses vis-à-vis the FCC spectral mask for each of the three antennas. We can see that the monocycle pulse has to be greatly attenuated to respect the FCC mask. Consider the SkyCross antenna (Fig. 4.6a) which has good out-of-band rejection and a passband within the FCC limits (Fig. 4.2a). When this antenna filters the Gaussian monocycle pulse, the EIRP of the transmit pulse has just 4% power efficiency. This clearly illustrates that the antenna is not an effective filter for the Gaussian monocycle pulse transmission. In this case, adding a UWB passband filter improves the PE [72].

Table 4.1: Relative power efficiency of antennas under study; Ant. 1: the SkyCross, Ant. 2: the circular monopole, and Ant. 3: the monopole antenna with two steps.

		Ant. 1	Ant. 2	Ant. 3
Gauss. monocycle	PE	4%	1.04%	1.2%
	Power (dBm)	-18.2	-24.1	-23.5
Filtered monocycle	PE	32%	20%	12%
	Power	-9.1	-11.2	-13.2
Gauss. 5 <sup>th</sup> der.	PE	40%	38%	30%
	Power (dBm)	-8.2	-8.4	-9.3
EIRP- optimized pulses	PE	71%	59%	60%
	Power (dBm)	-5.7	-6.7	-6.4
	gain over mono. (dB)	12.5	16.8	17.7
	gain over filtered mono.	3.4	4.5	6.8
	gain over 5 <sup>th</sup> der.	2.5	1.7	2.9

The EIRP of the Gaussian 5<sup>th</sup> derivative respects the FCC spectral mask for all three antennas, with no need for additional attenuation (Fig. 4.6). Although respecting the FCC mask, the spectrum of the Gaussian 5<sup>th</sup> derivative has much lower power efficiency compared to the EIRP-optimized pulses.

Table 1 shows numerical values of the power efficiency and the absolute power for the Gaussian monocycle, the filtered monocycle, the Gaussian 5<sup>th</sup> derivative and the EIRP-optimized pulses. The filtered monocycle is much more efficient than the Gaussian monocycle, but still has a transmit power between 3.4 to 6.8 dB less than those of EIRP-optimized pulses, depending on the antenna used. Among all the pulses, the pulse designed for the SkyCross antenna has the highest power efficiency. The highest pulse shaping gain goes to the monopole antenna with two steps with 17.7 and 2.9 dB improvement over the Gaussian monocycle and the Gaussian 5<sup>th</sup> derivative, respectively. The latter antenna, although worse than the circular monopole antenna in terms of bandwidth, results in a higher power efficiency. Therefore, the nonlinear pulse shaping method is effective in compensating severe antenna distortion.

BER simulations are performed to investigate the advantages of pulse shaping at the receiver. We consider the receiver as a linear filter matched to the pulse received in an AWGN channel. Thus, the filter impulse response is the convolution of the pulse shape and the antennas impulse response. Fig. 4.7a shows the simulation results for the AWGN channel at 512 Mb/s. The energy of each pulse is set to its maximum under the FCC regulations. The noise power spectral density,  $N_0$ , is changed to obtain different SNR values. The pulse power levels are set according to the values shown in Table 1 for the SkyCross antenna. In Fig. 4.7a, the energy of the EIRP-optimized pulse is taken as the reference. Therefore, the BER curve for this pulse is equal to  $Q(\sqrt{SNR})$ . We observe that the higher energy of the FCC-optimized pulse results in improved BER performance. The gaussian monocycle and fifth-derivative show worse BER performances compared to the FCC-optimized pulse, with energy penalties almost equal to the 2.5 dB and 12.5 dB mentioned in Table 1.

For a more realistic evaluation of performance, we use residential channel measurements from the Intel corporation [4], available at [http://ultra.usc.edu/uwb\\_database/](http://ultra.usc.edu/uwb_database/) instead of the AWGN channel. These measurements were collected for both LOS and NLOS channels from 2 to 8 GHz covering most of the FCC spectral mask. Fig. 4.7b shows the simulation results averaged over 52 LOS channels. We observe that the EIRP-optimized pulse has an even greater advantage over the Gaussian fifth derivative

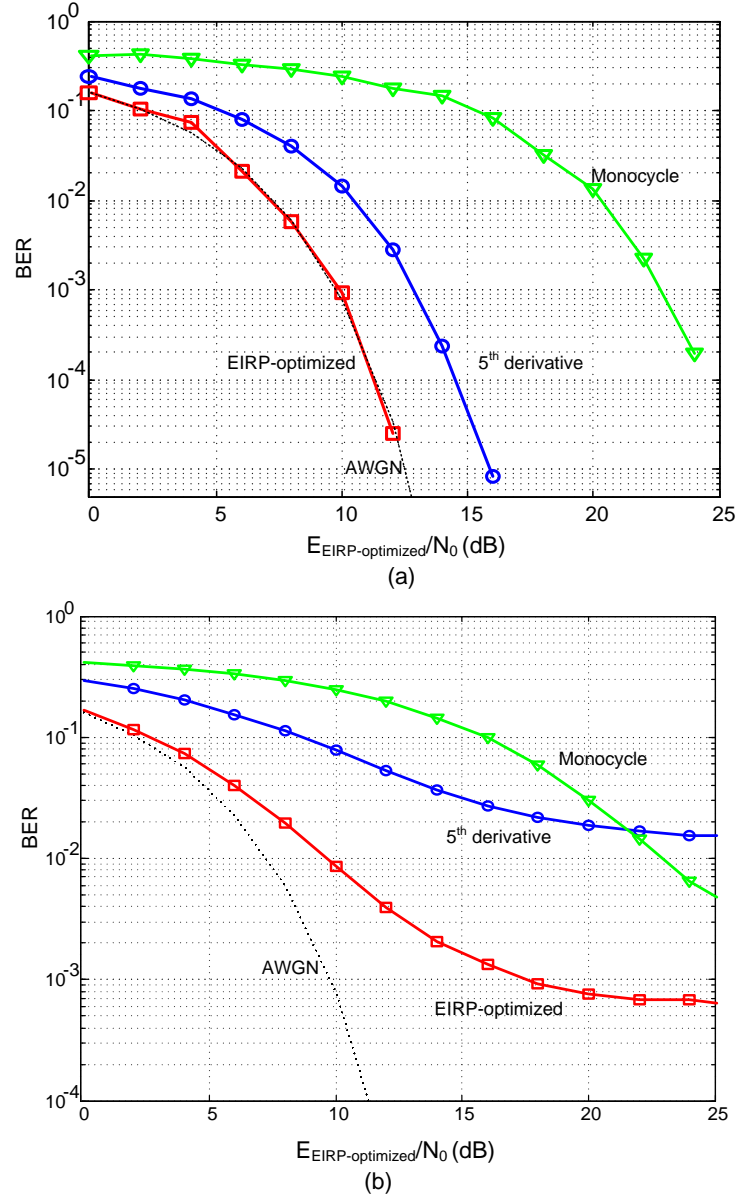


Figure 4.7: BER simulations; (a) the AWGN channel, (b) average over 52 LOS indoor multipath UWB channels.



and monocycle compared to the AWGN channel. Note that at low noise values, the BER performance is mainly limited by the ISI caused by the multipath propagation, whereas the waveform energy is more significant at the higher noise values. The Gaussian monocycle causes less ISI on the average channel compared to the Gaussian fifth derivative, leading to a better BER performance at high SNR values.

## 4.6 Conclusion

The Gaussian monocycle and the Gaussian fifth derivative, common UWB pulses, do not have good FCC mask coverage. In this chapter, we compared these pulses with optimally shaped pulses in realistic experimental conditions. By studying the bandpass characteristics of UWB antennas, we designed UWB pulses that efficiently exploit the FCC spectral mask. To do so, we used an optimization program to take into account the effects of the antenna to maximize the transmitted power, while respecting the FCC spectral mask.

Given the frequency response of each antenna, a unique pulse was designed for each antenna. The pulses were generated using an optical UWB waveform generator. The FCC-optimized pulses showed up to 17.7 dB improvement over the Gaussian monocycle and 2.9 dB improvement over the Gaussian fifth derivative. This result confirms that the antenna alone is not an appropriate filter to boost the power efficiency of the monocycle over the FCC mask; this approach is far from optimal. Highpass filtering the monocycle pulse is an effective method to improve its power efficiency, but the transmit power is still several dBs below that of shaped pulses. Even when using the Gaussian fifth pulse, the passband antenna cannot provide the same level of power efficiency as a pulse shaped to match the FCC mask. Simulation results showed that the FCC-optimized pulse has a significant BER performance improvement compared to the Gaussian monocycle and the Gaussian fifth derivative pulse under multipath propagation. The energy improvement in UWB pulses directly improves the receiver signal-to-noise ratio and extends the reach of the communication link.

# Chapter 5

## UWB receivers

In Chapter 2 we briefly discussed UWB receivers. We saw that the receivers are generally divided into two categories of coherent and noncoherent, depending on whether they exploit the absolute phase of the received signal or not. While coherent receiver has better performance, it is much more challenging to implement for UWB signals. We have simulated UWB receiver in previous chapters of this thesis to investigate the performance of our transmitters. In Chapter 3 we captured experimental data and simulated the BER performance of a linear filter and a square-law receiver in Matlab. In Chapter 4 we simulated the performance of a linear receiver for various pulse shapes and confirmed the superiority of power efficient pulses under multipath propagation.

In this chapter we focus on coherent receivers. The chapter is divided into two main sections. In Section 5.1 we use a novel electromagnetic bandgap (EBG) device, designed at McGill university, as a linear filter matched to the transmit waveform. The transmit waveform is a UWB pulse with high power efficiency designed to respect the FCC mask when using the SkyCross antenna (Section 4.3.1). The matched filter is synthesized and fabricated in microstrip technology with a section of quasi-continuous width modulation and a reflection response approximating the target waveform. The frequency response of the matched filter is measured using a VNA and shows close agreement with the target UWB pulse spectrum (Section 5.1.4). In Section 5.1.5 BER measurements are presented for the matched filter and a direct conversion filter. The direct conversion receiver or the homodyne receiver uses a mixer for downconversion of the pulses to baseband [31]. The BER measurements confirm superior performance of the matched filter compared to the direct conversion receiver in a back-to-back transmitter receiver

configuration.

In Section 5.2 we consider equalization of Gb/s UWB signal received by the linear filter matched to transmit waveform after passing through multipath wireless channel. Because of intersymbol interference at high bit rates caused by multipath propagation, equalization techniques need to be investigated for UWB reception. The Intel channel measurements are used in our simulations to find the performance of the equalizers in realistic indoors channel conditions. We investigate the Viterbi algorithm with a limited number of states and the decision feedback equalizer (Section 5.2.2). We examine both LOS and NLOS channels for the receiver with a linear filter matched to the transmit waveform. BER simulations confirm that equalization considerably improves the performance compared to symbol detection (Section 5.2.3).

## 5.1 UWB Reception Using an EBG

### 5.1.1 Introduction

Two common radio receivers are the matched filter and the correlator. A correlator receiver multiplies the received signal with a precisely synchronized signal template. The correlator maximizes the SNR in an AWGN channel [48]. The challenges in a correlator receiver are generation and synchronization of the template pulse. A matched filter receiver, when sampled at the peak signal output, yields the same output as the correlator, and hence has the same performance under ideal conditions. The matched filter receiver, like the correlator, requires precise timing. However, the required precision is less stringent than the correlator since the matched filter output peak is temporally twice as wide as that of the correlator (due to convolution properties).

Another common receiver structure is the direct conversion receiver. Direct conversion receivers are popular for use in mobile terminals due to advantages over other architectures such as heterodyne receivers in terms of cost, electrical current, and physical size [73]. The direct conversion receiver is similar to an integrate and dump strategy for baseband signals. The integration results in relaxed sampling requirements, being on the order of the symbol rate rather than pulse duration.

Implementation of matched filters for UWB reception is still the subject of much research. For example, matched filtering was performed with an optical pulse shaper in [74]. This method requires conversion of signals from the electrical to the optical domain and vice versa at the receiver. Phase matching at the receiver was shown to retrieve and compress distorted received signals. In [5], a matched filter was designed and implemented using the microstrip technology and electromagnetic bandgap (EBG) structures. The filter was designed to match a UWB sinusoidal burst that did not comply with the FCC mask. The filter was characterized by a vector network analyzer, but was not used in a receiver system.

In this work, we also use an EBG matched filter structure. We consider a power efficient UWB pulse that respects the FCC spectral mask when using the SkyCross antenna (Section 4.3.1). Note that here we tailor the filter to match the anticipated transmit pulse. Although optimal for an AWGN channel, this filter will not be optimal in multipath channel conditions. We measure BER performance of the matched filter receiver and we compared it to that of a direct conversion receiver in a back-to-back transmitter receiver configuration. We illustrate how a passive mechanism such as an EBG matched filter can yield good coherent detection results without the need for a high-power local oscillator in the mixing operation of direct conversion.

### 5.1.2 Experimental setup

Fig. 5.1a shows our target UWB pulse. This waveform is a power efficient, full-band UWB pulse spectrally shaped to utilize most of the available power [11]. This pulse is designed to reach its maximum efficiency when used with the SkyCross SMT-3TO10MA antenna as transmitter. The pulse was found by the optimization technique proposed in [17], and adapted to use with the antenna in [11].

We use our previously reported optical spectral shaping method for high precision pulse shaping (Section 4.4.1). A simplified block diagram of the transmitter is shown in Fig. 5.2. A Mach-Zehnder modulator is biased at quadrature and driven by 1 Gb/s data to modulate the impulses in an OOK format. A variable optical attenuator is used to adjust the optical intensity of the pulses. By varying the attenuation, we control the power of UWB pulses while measuring receiver-side BER curves. The gain-switched pulses next go through the FBG pulse shaper. There is a good match with the target

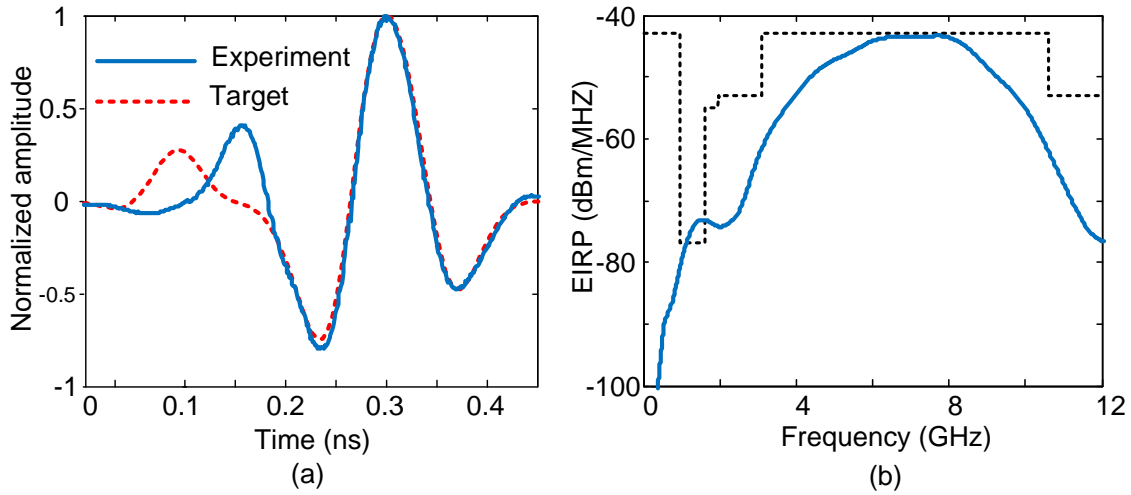


Figure 5.1: (a) The target UWB waveform (dotted line) and the generated pulse (solid line), (b) The spectral density of the generated UWB waveform under the FCC mask.

pulse in the time domain, except for a misplaced first peak (Fig. 5.1a). The EIRP is shown in Fig. 5.1b.

We consider two receivers as shown in Fig. 5.2, namely, the matched filter receiver and the direct conversion receiver. The matched filter is designed for the pulse shown in Fig. 5.1. Since the EBG filter works in reflection (*i.e.*, the desired frequency response is achieved in the  $S_{11}$  term of the scattering matrix), we require the use of a circulator (DiTom D3C4080) to collect the scattered pulse. We will see that the isolation between the circulator ports is an important factor to consider in overall performance of the matched filter.

The second receiver is a direct conversion receiver in which the UWB signal is mixed with a 6 GHz sinusoidal from the local oscillator (LO) to down convert the signal to baseband. We use the MiniCircuits ZMX-8GLH mixer with an RF port bandwidth of 3.7 - 8 GHz and an IF bandwidth of 0 - 2 GHz. The conversion loss of the mixer is around 5 dB when used with a 10 dBm LO. The use of a delay line in the transmitter allows for phase adjustment between the two mixed signals to achieve the best extinction ratio for 1 and 0 bits. Note that the same function could be performed by an RF phase shifter at LO. The output from the mixer is filtered with a lowpass filter. We do not include antennas in this work and consider only a back-to-back transmitter and receiver.

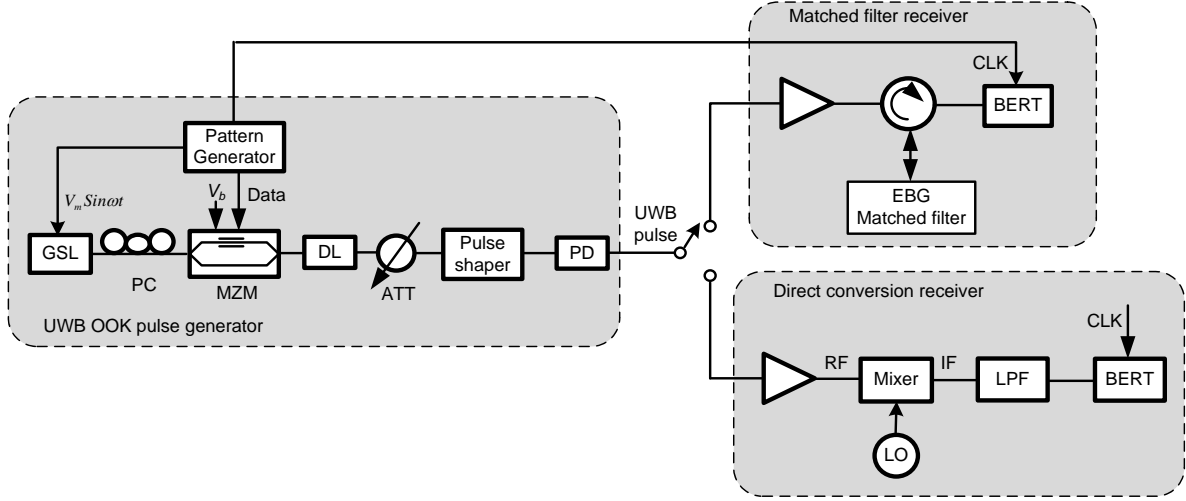


Figure 5.2: The schematic diagram of the UWB transmitter and receiver systems. GSL: gain switched laser, PC: polarization controller, MZM: Mach-Zehnder modulator, DL: delay line, ATT: attenuator, PD: photodetector, EBG: electromagnetic bandgap, LO: local oscillator, BERT: bit-error-rate tester.

### 5.1.3 EBG Design and Fabrication

We designed the response of the matched filter EBG using a synthesis method described in [75], by which a target impulse response is sampled in the frequency domain and converted into a corresponding set of values for a coupling coefficient between the co- and counter-propagating quasi-TEM mode along a fixed length of transmission line. There is then a one-to-one conversion between the desired reflective coupling coefficient and the impedance (and therefore width) of the transmission line. The resulting structure is a (nominally 50 ohm) microstrip line with a section of quasi-continuous width modulation (*i.e.*, a "wiggly-line" filter) and a reflecting  $S_{11}$  parameter approximating the target response.

The matched filter is synthesized out of a 10 cm long width-modulated microstrip line on a 0.635 mm-thick Rogers RT6010 substrate ( $\epsilon_r = 10.2$ ,  $\tan \delta = 0.0023$ ). The choice of high-permittivity material reduces the required length of the structure for a given level of precision in synthesizing the response. The synthesis technique assumes the material to be lossless although simulations in Ansoft's HFSS software were used prior to fabrication to ensure that the impact of losses was minimal.

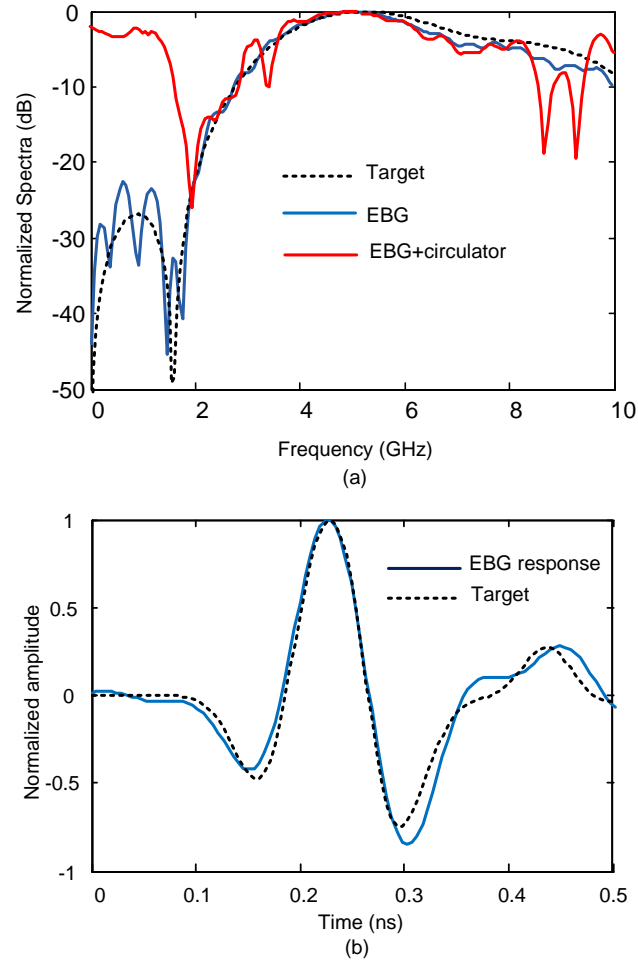


Figure 5.3: Characterization of the EBG filter. (a) The target frequency response of the filter, the measured response, and the response of the filter when used with the circulator, (b) the impulse response of the EBG compared to the ideal matched filter impulse response. Amplitude values are normalized.

#### 5.1.4 Matched filter characterization

The frequency response of the matched filter,  $S_{11}(f)$ , is measured by a vector network analyzer (VNA-N5230A). The second port of the EBG is terminated into a  $50\ \Omega$  matched load. Fig. 5.3a shows the measured frequency response of the EBG, as well as the target frequency response. There is a good agreement between the two curves, but we can observe that the filter is showing slightly less reflection than the designed values at higher frequencies. We also characterize the EBG when used with the circulator (Fig. 5.3a). The circulator distorts the frequency response and degrades the quality of the matched filter. The circulator we used has a 20 dB isolation from 4 GHz to 8 GHz.

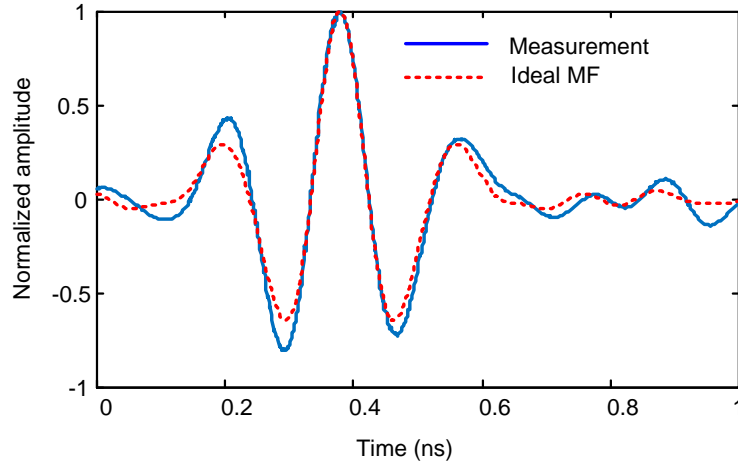


Figure 5.4: The normalized output waveform of the matched filter. The measurement is in good agreement with the theory.

The ripples in the frequency response are mainly caused by the power leakage in the isolated ports of the circulator. The circulator has completely distorted the frequency response at frequencies below 2 GHz. This is not an issue since the UWB pulse is extremely weak at these low frequencies.

The impulse response of the matched filter is found by the inverse Fourier transform of the measured frequency response. Fig. 5.3b shows a good match between the target impulse response and the actual response of the filter. The circulator, however, adds some reflections in the time domain (Fig. 5.5a).

Fig. 5.4 shows the normalized output of the matched filtered measured by the oscilloscope. This measurement is compared to the ideal matched filter response obtained from the convolution of the UWB waveform with its time-reversed copy. We can see a good match between the measurement result and the ideal matched filter output. There are also some reflections from the circulator which occur temporally earlier than the matched filter main output as seen in Fig. 5.5a. Another source of error is that our generated UWB pulse is not exactly the same as the pulse chosen for the EBG design (Fig. 5.1a). This error is caused by the optical filters in the pulse shaper.



### 5.1.5 BER measurement and discussion

To measure the BER, we use the standard  $2^7 - 1$  PRBS as OOK data with a bit-rate of 1 Gb/s. By adjusting the delay and the threshold of the BERT, the output of the matched filter is sampled at its peak and the decision threshold is optimized for each received power. Fig. 5.6 plots the BER versus the normalized optical power. The pulse power is changed by adjusting the optical attenuator at transmitter. Fig. 5.6 also shows the BER measurement for the direct conversion receiver. The relative phase of the LO and the incoming UWB sequence is adjusted to maximize the eye opening in this case for the best performance. The two receivers have different insertion losses, such that for an equal input power, the output power of the matched filter receiver is around 2.5 dB higher than the direct conversion receiver.

We observe an error floor in the BER curves of Fig. 5.6. A matched filter receiver does not induce a floor when the noise is Gaussian, but rather waterfall BER curves [48]. We attribute the error floor to non-idealities in the optical source. The gain-switched laser suffers from relatively high timing jitter of several picoseconds. This source also shows higher amounts of noise than a mode-locked laser. The reflection from the circulator (Fig. 5.5) thickens the zero of the eye-diagram and increases the error.

Besides the better BER performance, another advantage of the matched filter over direct conversion is that the EBG is a passive device, whereas the mixer constantly needs a 10 dBm LO. The disadvantage of the matched filter is the need for precise synchronization to find the sampling point at the receiver. Channel estimation and synchronization schemes have been subject to much research in the literature [76]. In the direct conversion receiver the signal has a wider peak, alleviating the synchronization requirements and reducing the receiver complexity.

The BER measurements in this work were performed in back-to-back operation. Obviously, a wireless channel severely degrades the BER performance by attenuating and adding ISI. Using forward error correction (FEC) codes and equalization techniques at the receiver are essential to combat the channel ISI [47].

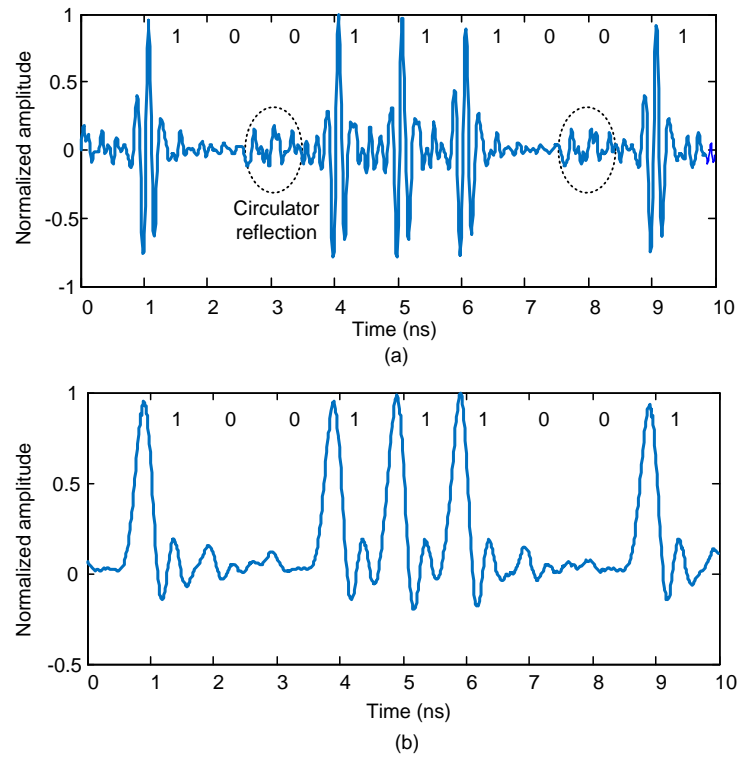


Figure 5.5: (a) The output waveform of the matched filter for a bit sequence of [1 0 0 1 1 1 0 0 1], (b) the output of the direct conversion receiver for the same bit sequence.

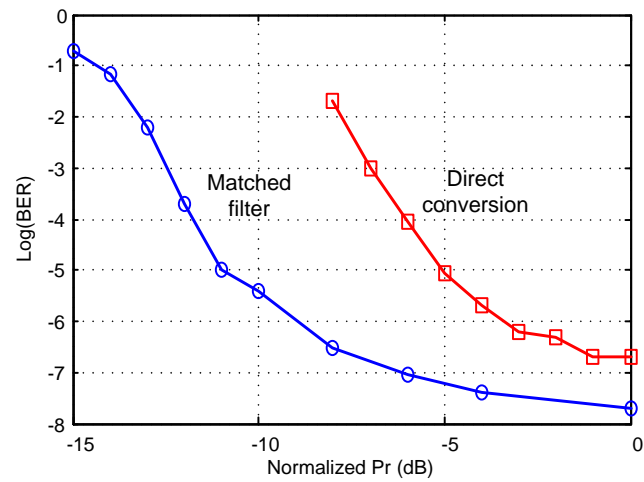


Figure 5.6: The measured BER curves for the matched filter and the direct conversion receivers.

## 5.2 Equalizers for IR-UWB Linear Receivers

In Chapter 4, we showed pulse shaping techniques that eke out most of the available power under the FCC mask [11]. Pulse shaping improves receiver performance by increasing the received SNR. In this section we focus on another UWB system challenge, operation in severe multipath while assuming pulse shapes that address the power limitation. During transmission, UWB pulses are spread to several nanoseconds. At data rates where the channel delay spread is longer than the symbol period, significant ISI occurs at the receiver. The ISI rapidly becomes a major limiting factor to increasing of data rate.

Equalizers compensate for the ISI induced by the channel. The Viterbi algorithm, though computationally complex, can optimally (maximum likelihood) remove distortion that stems from a linear system with finite memory [77]. For multipath propagation, the memory is due to ISI. In [78], the VA was used to equalize the output of a nonlinear receiver for UWB OOK signal transmission at 50 Mb/s. The decision feedback equalizer is a simple, nonlinear equalizer which is particularly useful for channels with severe amplitude distortion; feedback is used to cancel the interference from symbols which have already been detected [79]. The DFE was applied to ISI in a nonlinear UWB receiver in [46]. The memory of the equalizer was set to one and it was mentioned that the data rate could not be increased far beyond 100 Mb/s without severe performance degradation.

Another strategy to reduce the ISI is to use multiband OFDM so that each carrier operates at a lower rate [80]. This method, however, exacerbates power limited operation, as roughly only one twelfth of permitted power can be transmitted in one 500 MHz band. For this reason, we concentrate on impulse radio ultra-wideband.

As it has been shown throughout this thesis, UWB transmitters with bit rates above 500 Mb/s for IR-UWB communications have become very common. Although transmitters are capable of operating at several Gb/s, UWB system performance quickly deteriorates because of ISI at these fast bit rates. The communication speed limit does not come from the transmitter, but rather from the ISI that limits receiver operation. We consider a complete UWB link composed of a pulse transmitter, antennas, true UWB multipath channel measurements, and a linear receiver (Section 5.2.1). We examine the VA and the DFE and investigate equalizer memory requirements for reliable

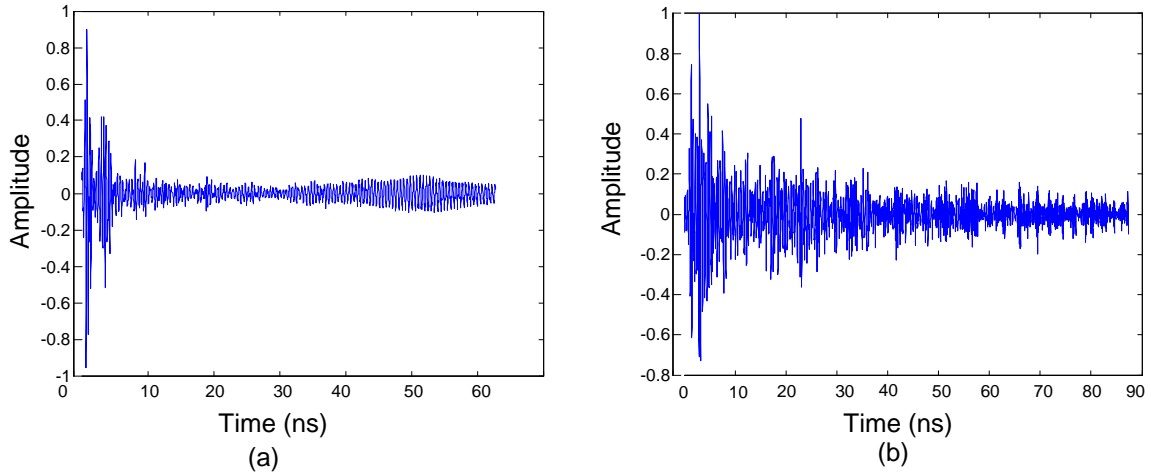


Figure 5.7: (a) LOS impulse response measurement (b) NLOS impulse response measurement.

Gb/s IR-UWB transmission for LOS channels. NLOS channels are also investigated, however at lower speeds.

We use residential channel measurements from the Intel corporation [4], available at [http://ultra.usc.edu/uwb\\_database/](http://ultra.usc.edu/uwb_database/). These measurements were collected for the 2 to 8 GHz band covering most of the FCC spectral mask. The measurements are available for 52 LOS and NLOS channels. These measurements formed the basis for the IEEE 802.15.3a channel model [4, 33].

To obtain the wireless channel response, the effects from components behavior were taken out. The time domain channel impulse response is found by the inverse Fourier transform. The zero time mark is set to the arrival of the first detectable path. As an example, Figure 5.7a shows the impulse response measured for a LOS channel. Fig. 5.7b shows the impulse response measured for a NLOS channel. Given the higher number of paths for NLOS channel, receiver complexity may be increased for systems designed for use in NLOS environments.

We consider a simple linear receiver followed by equalization and target achieving a BER performance better than  $10^{-3}$ , which is the FEC limit (Section 5.2.3). We examine both the VA and the DFE to compensate the ISI in LOS and NLOS channel conditions. As the bit rates are high, the optimal VA is exceedingly complex, hence we examine the VA with a reduced number of states. The trade-offs of the two methods are discussed.

Table 5.1: Channel parameters from [4]

	LOS	NLOS
Number of channels	52	52
Distance	<10 m	<15 m
Mean excess delay	12.6 ns	19.3 ns
RMS excess delay	21.4 ns	24.2 ns
Time resolution	62.5 ps	62.5 ps

We will show that data-rates up to 1 Gb/s can be achieved in line-of-sight multipath channels.

### 5.2.1 System Model

Fig. 5.8 shows the complete system model used in the simulation of the IR-UWB pulse transmission. At the transmitter, the pulses are modulated with either the OOK or the BPSK scheme. We consider an efficient UWB pulse specially shaped to utilize most of the available power [11]. The transmit antenna is SkyCross SMT-3TO10MA antenna. The pulse was designed by an optimization process of combining seven Gaussian monocycle pulses to achieve very high power efficiency when using the SkyCross antenna [11]. The gain response of the antenna is measured using a vector network analyzer as described in [11]. The simulated pulse stream (matching that measured) is passed through the multipath channel, as explained in the next paragraph, and received by an antenna identical to the transmit antenna.

The transmitted pulses are convolved with impulse response measurements from Intel. Impulse responses were calculated from measurements recorded in the frequency domain, from 2 to 8 GHz [4]. The measurements were performed in a typical residential house and are available as 52 LOS and 52 NLOS cases. These impulse responses are normalized and only consider multipath propagation and do not take into account any fading. Table I shows some of the parameters associated with these measurements. While more computationally intensive than using a statistical model, this has the advantage of testing the receiver in real world UWB home environments.

The receiver is composed of a linear filter, a sampler at the symbol-rate,  $T$ , and

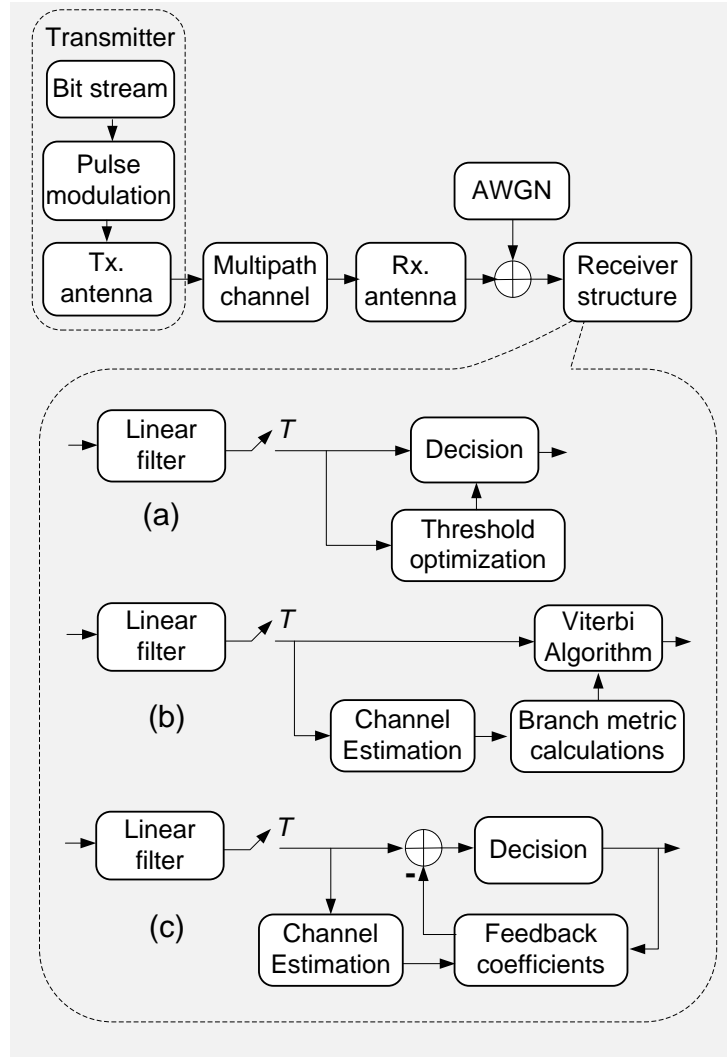


Figure 5.8: The system model.

the decision algorithm (Fig. 5.8). The linear filter is a filter matched to the transmit pulse shape. Because of the high number of multipath components in the received signal, receivers matched to the received pulse are extremely complex for UWB systems. Matching to the transmit pulse is not optimal, but its implementation is straightforward. In [81], the performance of the matched filter was compared to RAKE receivers. The matched filter has poorer performance as it collects less than the maximum available energy at the receiver.

In our simulations, we determine the sampling point by sending a training sequence of a single 1 followed by a sufficient number of 0s to cover the channel memory. We sample at the point where the linear filter output amplitude is maximum. Other synchronization schemes are also possible, e.g. [76].

Bit estimates are produced either by threshold detection of the sample (Fig. 1a), or by employing equalization (Figs. 5.8b and 5.8c). The BER performance is very sensitive to the threshold value for the receiver in Fig. 5.8a. We find the optimal threshold by sending a training sequence of random bits and varying the threshold value. At each SNR, the threshold value that minimizes the number of decision errors is chosen as the optimal threshold. This threshold value exactly corresponds to the middle of the received signal eye diagram opening.

At high data rates, ISI limits the performance of symbol detection schemes as the eye diagram can be completely closed. Equalizers, discussed in the next section, are added to the receiver to compensate for the ISI; Fig. 5.8b shows the Viterbi equalizer, and the decision feedback equalizer is shown in Fig. 5.8c.

### 5.2.2 Equalization

The transmit symbol sequence is

$$x(t) = \sum_i b_i s(t - iT), \quad (5.1)$$

where the data bits are  $b_i = \{0, 1\}$  in an OOK modulation scheme and  $b_i = \{-1, 1\}$  in a BPSK scheme;  $s(t)$  is the spectrally efficient UWB pulse from [11]. The received signal after propagation is

$$r(t) = \sum_i b_i p_R(t - iT) + n(t), \quad (5.2)$$

where  $n(t)$  is AWGN with a two-sided spectral density  $N_0/2$ , and  $p_R(t)$  is the received signal that can be expressed as

$$p_R(t) = s(t) * g_{Tx}(t) * h(t) * g_{Rx}(t), \quad (5.3)$$

where  $g_{Tx}(t)$  and  $g_{Rx}(t)$  are the measured transmit and receive antenna gain responses,  $h(t)$  is the channel impulse response, and  $*$  denotes the convolution operation. The output of the linear receiver filter is

$$z(t) = r(t) * s(T - t), \quad (5.4)$$

where the linear filter response is matched to the transmitted UWB pulse shape. In an AWGN channel, the impulse response of this filter maximizes the output SNR. This

is not true for multipath conditions where ISI exists.  $z(t)$  is sampled with period  $T$ , and forms the input to the equalizers. We use the AWGN channel BER performance as a reference for our simulation,  $Pe = Q(\sqrt{Eb/N_0})$  for OOK modulation, and  $Pe = Q(\sqrt{2Eb/N_0})$  for BPSK modulation [82].

### The Viterbi Algorithm (VA)

The Viterbi algorithm is a maximum likelihood sequence estimator (MLSE). The detection is based on choosing the most likely random sequence  $U = \{u_k, u_{k+1}, \dots\}$  from a received sequence  $Z = \{z_k, z_{k+1}, \dots\}$  where  $k$  is the sample value at time  $t_k$ , and  $z_k = u_k + n_k$ , where  $n_k$  are the noise samples. The maximum likelihood rule can be expressed as

$$p(Z|\hat{U}) = \arg \max p(Z|U), \quad (5.5)$$

where  $U$  is the ensemble of all possible ISI-distorted sequences [77]. The linear filter bandwidth is around 10 GHz. Therefore, the noise samples after sampling with period  $T$  can be assumed independent, as  $T$  is much longer than the coherence time of the noise. Thus, the likelihood in (5.5) becomes:

$$p(Z|U) = \prod_k p(Z_k|U_k). \quad (5.6)$$

The noise samples after the linear receiver are zero-mean Gaussian with equal variances. Therefore, the MLSE can be performed using the VA with branch metrics  $(z_k - u_k)^2$ , at time  $t_k$ . Assuming the binary scheme and memory length  $M$ ,  $2 \times 2^M$  branch metrics should be calculated at each time instant. As shown in Fig. 5.8b, we need the channel estimation to compute the metrics. We assume that a noiseless estimate of the channel is available.

### The Decision Feedback Equalizer (DFE)

As the complexity of the Viterbi algorithm increases exponentially with channel memory, certain memory lengths (above 10) can pose serious complexity challenges. Sub-optimal equalizers, such as the VA with a limited number of states and the decision feedback equalizer, are interesting alternatives [79].

In a DFE (Fig. 5.8c), the decision made on a symbol is fed back, via a filter, to



cancel its ISI contribution to the subsequent bits. The filter weights are set to a sampled version of the system impulse response. For the OOK modulation, the DFE adjusts the signal samples according to

$$\text{if } z_k > 0 : z_{k+i} = z_{k+i} - w_i, \quad (5.7)$$

where  $i = 1, 2, \dots, M$  and  $w_i$  are the filter coefficients,

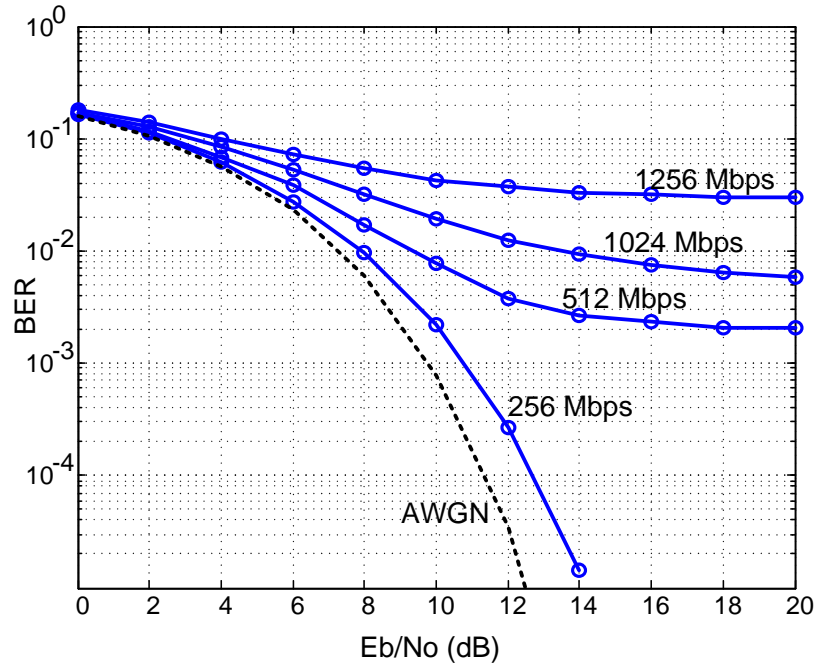
$$w_i = p_R(t) * s(t - T)|_{t=T_s+iT}, \quad (5.8)$$

where  $T_s$  is the sampling time at the maximum of the linear filter output and  $w_1, w_2, \dots, w_M$  are the residual sample values leaking into the consequent bits. By increasing the number of taps, more ISI can be corrected, but the DFE may suffer from error propagation where an incorrect decision causes more errors by sending incorrect feedback. Note that the DFE complexity increases only linearly with the number of taps, while the VA complexity increases exponentially with memory.

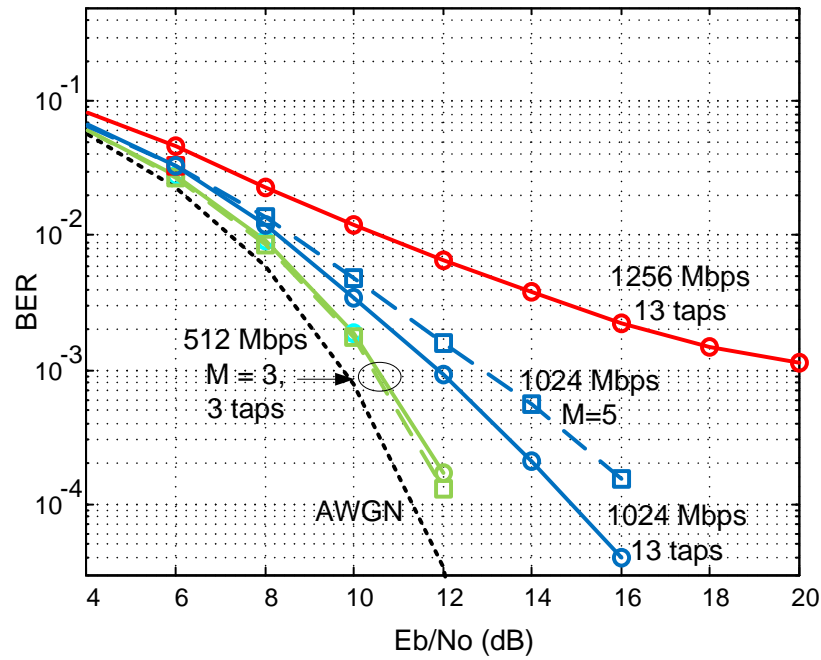
### 5.2.3 Simulation results

In this section we compare the performance of the three detection methods introduced in Section 5.2.1. The BER simulations are found from averaging over 52 LOS and 50 NLOS multipath channels. Our target is to reach a probability of error better than  $10^{-3}$ , thus falling within the effective region of error correction codes. The VA has a maximum memory of 5, whereas the DFE has up to 21 taps. The true memory depends on channel and bit rate, and can vary from a few bits to tens of bits. The BER curves for an ideal AWGN channel are considered as references.

Fig. 5.9 shows the BER simulations for the OOK modulation scheme. The symbol detection scheme works well at 256 Mb/s, but we observe error floors caused by ISI at speeds higher than 512 Mb/s (Fig. 5.9a). Fig. 5.9b shows the BER with equalization to reduce the ISI. There is no error floor at 512 Mb/s when using either  $M = 3$  in the VA, or 3 taps in the DFE. We can see when both DFE and VA are set to the same channel memory target (3 in this case), the VA performs slightly better than the DFE. At 1024 Mb/s, the simulation results show that using 13 taps in the DFE leads to better performance than the VA with  $M = 5$ . Using 13 taps in the DFE, we can still reach the FEC threshold at 1256 Mb/s. The Viterbi algorithm with such a high number of memory is extremely computational and practically impossible. In this case, the larger memory coverage in the DFE lets it outperform the VA.



(a)



(b)

Figure 5.9: BER simulations of OOK UWB signals in LOS multipath channel conditions; (a) symbol detection, and (b) the VA versus the DFE.

BER simulations of the BPSK modulation format are shown in Fig. 5.10. For an AWGN channel BPSK has a 3 dB advantage over OOK. This advantage is even greater in multipath channels. Fig. 5.10a plots the BER for the symbol detection scheme, where error floors are observed at data-rates higher than 768 Mb/s. Fig. 5.10b shows how the equalization improves the performance. At 768 Mb/s, the VA with  $M = 5$  performs better than the DFE with 13 taps. At 1536 Mb/s, there is still an error floor, but the BER reaches  $10^{-3}$  at SNR=18.

Fig. 5.11 shows simulation results obtained for NLOS multipath propagation of BPSK UWB signals. Achievable data rates are much lower than with LOS, even after equalization. At 128 Mb/s, an equalization memory of 5 brings the performance very close to the AWGN channel. At 256, the DFE with 21 taps performs much better than the VA with  $M = 5$ .

In Fig. 5.11, we observe that the average BER performance of the NLOS channels degrades quickly with increasing data rate. That is because the average BER is dominated by the performance of the worst channels, despite most channels exhibiting good performance. To investigate this behavior, we define a fault percentage as the percentage of the channels that have an error rate higher than  $10^{-3}$  at SNR = 20 dB. Fig. 5.12 plots the fault percentage for the OOK and BPSK modulation formats obtained for 50 NLOS channels, when using a DFE with 21 taps. It is clear that equalization significantly reduces the fault percentage. From Fig. 5.12, we can observe that the BPSK format has a lower fault percentage compared to the OOK format, both before and after equalization. The fault rate of the NLOS transmission quickly saturates as the data rate increases.

We observe that for a given equalizer memory, the VA performs slightly better than the DFE. The VA, however, is computationally prohibitive and limited to a few memory lengths. The computational complexity of the VA is proportional to  $2^M$ , whereas in the DFE, the complexity is linearly proportional to the number of taps. Note that an increase in the number of states of the VA always leads to an improvement in the BER. The DFE results do not necessarily improve by increasing the number of taps, although they do in most cases. Taking into account the complexity of the algorithms, the DFE provides an effective method for mitigating ISI in high data rate UWB communication systems.

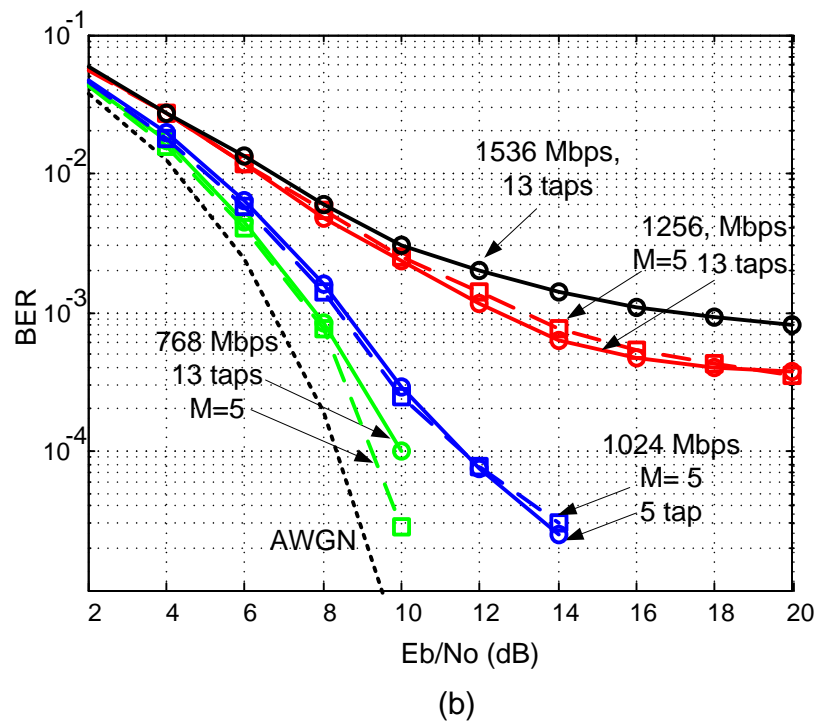
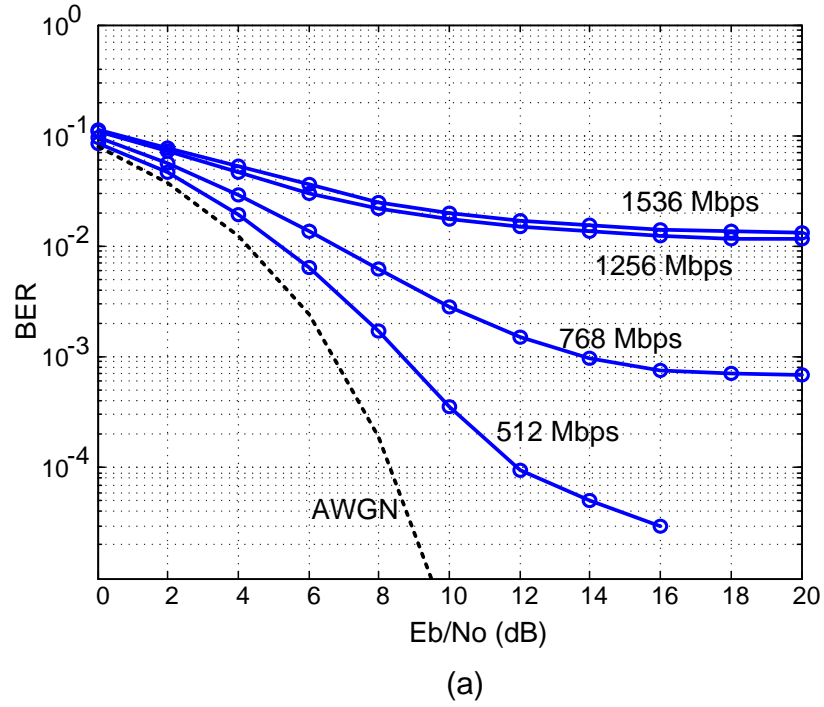


Figure 5.10: BER simulations of BPSK UWB signals in LOS multipath channel conditions; (a) symbol detection, and (b) the VA versus the DFE.

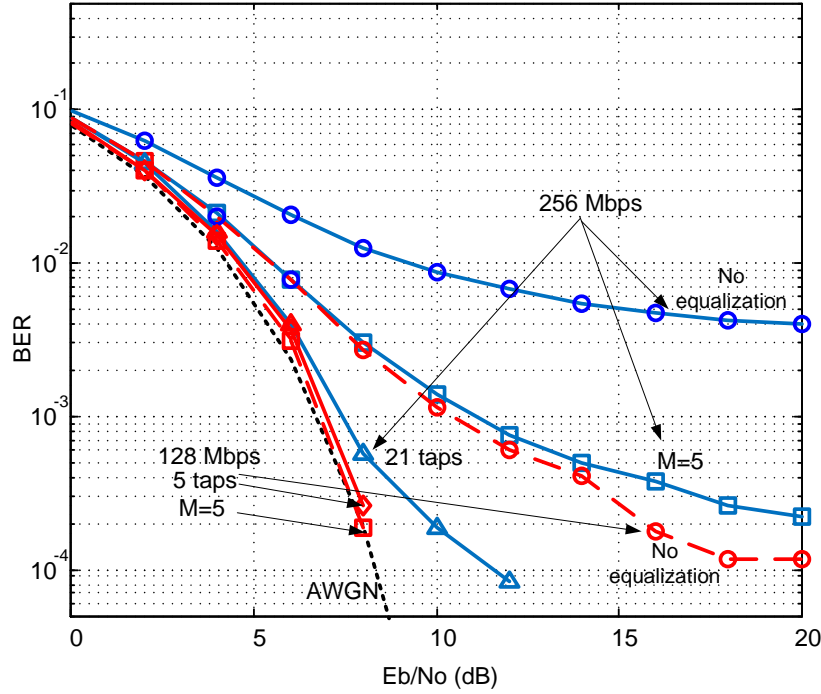


Figure 5.11: BER simulations of BPSK UWB signals in NLOS multipath channel conditions.

### 5.3 Conclusion

We designed and fabricated a matched filter to receive efficiently designed UWB pulses. The matched filter was synthesized and fabricated in microstrip technology. The frequency response of the matched filter showed close agreement with the target UWB pulse spectrum. However, the use of a circulator with the filter distorted this frequency response and caused slight reflections in the time domain impulse response. The output of the matched filter was close to an ideal matched filter response. BER simulations quantified the superior performance of the matched filter compared to a direct conversion receiver. Future work includes testing the matched filter receiver in multipath wireless channel conditions and comparing the performance to incoherent receivers.

The UWB channel is very rich in multipath leading to ISI at high bit rates. In this work, we considered a complete UWB link composed of a pulse transmitter, antennas, realistic multipath channels, and a linear receiver. The OOK and BPSK modulation formats were considered. Simulation results showed that the performance of such system degrades significantly for data-rates higher than 500 Mb/s. To compensate the

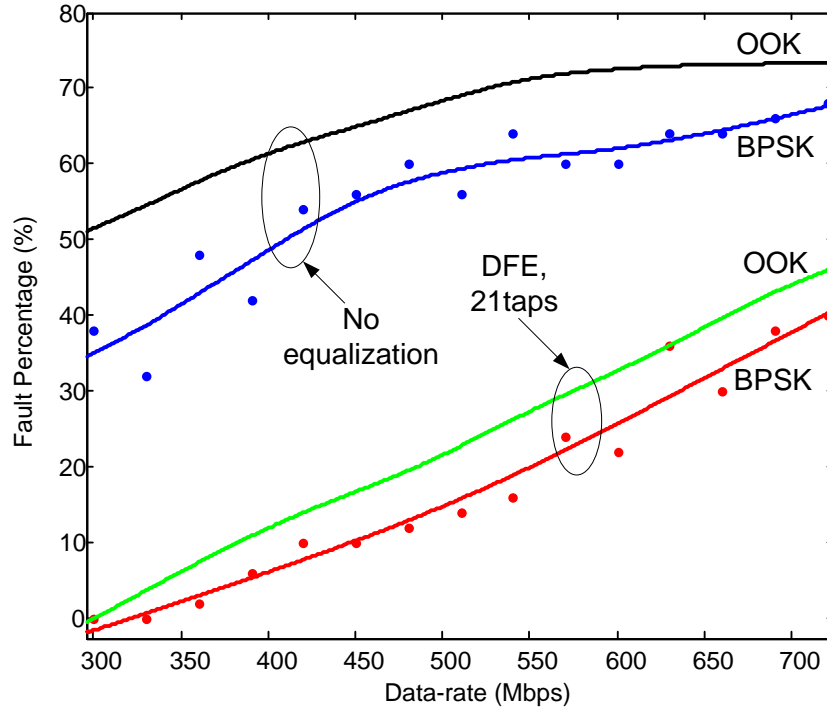


Figure 5.12: The fault percentage of NLOS UWB signal detection using a DFE with 21 taps.

severe ISI at gigabit rates, we investigated the Viterbi algorithm with a limited number of states and the decision feedback equalizer. We examined the required number of states in the VA, and the number of taps in the DFE for reliable Gb/s IR-UWB transmission for LOS channels. NLOS channels were also investigated at lower speeds. BER simulations confirmed that equalization considerably improves the performance compared to symbol detection. The DFE results in better performance compared to the VA when using comparable complexity as the DFE can cover greater channel memory with a relatively low complexity level. The low computation complexity of the DFE makes it a suitable equalizer to be employed at high data rate UWB receivers.

# Chapter 6

## Conclusions and Future Work

FCC regulations limit the radiated power of UWB signals to avoid interference with narrowband radios. The extremely low power of UWB limits its reach to a few meters. We have considered optical generation and transportation of UWB pulses over fiber to address this problem. The huge bandwidth of the optics suits generation of these wideband signals, and the optical fiber offers a low loss medium to carry radio signals for several kilometers. In a radio over fiber scheme, the data is modulated on laser light at the central office. The data for several users can be combined to form a WDM signal. The WDM signal propagates in the optical fiber and is demultiplexed at a remote node. Photodetection converts the signals to the electrical domain at the end user side before wireless transmission. The RF environment is more challenging for UWB communications because of extremely low power of these signals and also the multipath propagation.

In this thesis our first contribution was proposing novel optical UWB signal generation methods. In our first transmitter, we used a gain-switched laser as a pulsed optical source. An MZM was used to multiply the pulses with a 6.85 GHz sinusoidal signal, upconverting the pulses to the center of the FCC spectral mask. A differential photodetection scheme removed the low-frequency components. The generated OOK UWB pulse showed a good FCC spectral mask compliance, with a power efficiency of 42%. We showed good power efficiencies for fiber lengths between 15 km and 25 km. The use of an MZM as the pulse shaping device promises future optical on-chip UWB transmitters based on silicon photonics technology. In our second pulse generation scheme, to generate BPSK pulses, we used a combination of data and a sinusoidal signal to modulate

a CW laser using an MZM. Fiber propagation caused no significant degradation to the pulses, validating use of such systems in PONs. In our third proposed transmitter, for a low cost integrated solution we designed a silicon micro-ring resonator to spectrally filter gain-switched laser pulses. SMF propagation performed the frequency-to-time mapping and balanced photodetection removed the low frequency components of the generated RF signals. The experimental results matched our simulations and the pulse spectrum respected the FCC mask.

Our second contribution was exploiting UWB antenna frequency response to design pulses with high power efficiencies. We proposed a nonlinear optimization technique to take into account the antenna distortions to find waveforms that maximize the transmitted power, while respecting the FCC spectral mask. We considered three antennas and designed a unique pulse for each one. The FCC-optimized pulses showed up to 17.7 dB improvement over the Gaussian monocycle and 2.9 dB improvement over the Gaussian fifth derivative. This result confirms that the antenna alone is not an appropriate filter to boost the power efficiency of the monocycle over the FCC mask. Simulation results showed that the FCC-optimized pulse has a significant BER performance improvement compared to the Gaussian monocycle and the Gaussian fifth derivative pulse under multipath propagation. The energy improvement in UWB pulses directly improves the receiver signal-to-noise ratio and extends the reach of the communication link.

Our third contribution was evaluating a matched filter to receive efficiently designed UWB pulses. The matched filter was synthesized and fabricated in microstrip technology as an electromagnetic bandgap device. The frequency response of the matched filter showed close agreement with the target UWB pulse spectrum. BER measurements quantified the superior performance of the matched filter compared to a direct conversion receiver.

Because of advances in electrical and optical UWB transmitters, multi Gb/s data rates are achieved. The UWB channel is very rich in multipath leading to ISI at high bit rates. Our last contribution was investigating the performance of receivers by simulating a system employing realistic channel conditions. Simulation results showed that the performance of such system degrades significantly for data-rates higher than 500 Mb/s. To compensate the severe ISI at gigabit rates, we investigated the Viterbi algorithm (VA) with a limited number of states and the decision feedback equalizer (DFE). We examined the required number of states in the VA, and the number of taps in the DFE for reliable Gb/s IR-UWB transmission for line-of-sight channels.



Non-line-of-sight channels were also investigated at lower speeds. BER simulations confirmed that equalization considerably improves the performance compared to symbol detection. The DFE results in better performance compared to the VA when using comparable complexity as the DFE can cover greater channel memory with a relatively low complexity level.

An interesting subject for future work is low cost silicon integrated UWB transmitters. Silicon photonics provides solutions for low cost, small footprint optical integrated circuits that can be integrated with electronic chips. Silicon Mach-Zehnder modulators have good performance and can be used in our proposed transmitters. Furthermore, we can integrate splitters, attenuators and photodetection on chip. Another interesting research could be using integrated Bragg gratings to shape UWB pulses.

Most challenges for UWB communications lie in the electrical domain and receiver design. There are different choices between coherent and noncoherent receivers with performance and complexity tradeoffs. Each receiver requires certain timing precision. Synchronization techniques are crucial specially for coherent receivers. There are other equalizers such as frequency domain equalizer that can be investigated at Gb/s data rates. Higher order modulation, such as QAM or QPSK require a lower symbol rate and reduce the ISI. Investigating these modulation formats and also OFDM can be of interest.

Regarding our work with the EBGs for matched filter design, future work includes incorporating the antenna frequency response in design of the filter, testing the matched filter receiver in multipath wireless channel conditions, applying equalization and forward error correcting codes and comparing the performance to noncoherent receivers.

# Publication List

I have contributed to the following works during the time of my PhD, most of which I have presented in great details in this thesis.

1. M. Mirshafiei, S. LaRochelle, and L. A. Rusch, "Optical UWB waveform generation using a micro-ring resonator," *IEEE Photonics Tech. Lett.*, vol.PP, no.99, pp.1, 0.
2. M. Mirshafiei, M. Abtahi, P. LaRochelle and L. A. Rusch, "UWB Pulse Shaping: Bypassing the Limitations of the Gaussian Monocycle," *Accepted at the IET Communications*.
3. M. Mirshafiei and L. A. Rusch, "Low Complexity Optical distribution of Gb/s BPSK UWB signals," *IEEE Photonics Techol. Lett.*, vol.24, no.10, pp.803-805, May15, 2012.
4. M. Mirshafiei, A. Ghazisaeidi, D. Lemus, S. LaRochelle and L. A. Rusch, "Upconversion of Gain-Switched Laser Pulses for Optical Generation of UWB Signals," *IEEE J. Lightw. Techol.*, vol.30, no.2, pp.207-214, Jan. 2012.
5. M. Mirshafiei, J. D. Schwartz, D. Plant, L. A. Rusch, "UWB Matched Filter Reception Using an Electromagnetic Bandgap Structure," *IEEE Int. Conf. on Ultra-Wideband*, Italy, Sept. 14-16, 2011.
6. M. Mirshafiei, L. A. Rusch, "Equalizer Complexity/Performance Trade-Offs for High Data-Rate IR-UWB Linear Receivers in Multipath Channels," *IEEE Int. Conf. on Ultra-Wideband*, Italy, Sept. 14-16, 2011.
7. M. Mirshafiei, M. Dastmalchi, M. Abtahi, S. LaRochelle, L. A. Rusch, "Optical Distribution of UWB: Low Complexity Pulse Generation Supporting OOK and PSK," *IEEE Topical Meeting on Microwave Photonics*, 5-9 Oct., 2010.

8. M. Mirshafiei, A. Ghazisaeidi, D. Lemus, L. A. Rusch, "Optical Generation of UWB Waveform via Upconversion of Gain-Switched Laser Pulses," *The 23rd Annu. Meeting of the IEEE Photonics Soc.*, Denver, Colorado, 7-11 Nov., 2010.
9. M. Mirshafiei, M. Abtahi, P. LaRochelle and L. A. Rusch, "Pulse Shapes That Outperform Traditional UWB Antenna/Waveform Combinations," *IEEE Globecom 2010*, Miami, Florida, USA, 6-10 Dec., 2010.
10. M. Mirshafiei, M. Abtahi, L. A. Rusch, and S. LaRochelle, "Wideband Antenna EIRP Measurements for Various UWB Waveforms," *IEEE Int. Conf. on Ultra-Wideband*, Hannover, Germany, Sept. 10-12, 2008.

# Bibliography

- [1] First report and order, (Revision of part 15 of the commission's rules regarding ultra-wideband transmission systems), US. Fed. Comm. Commission, adopted Feb. 14, 2002, released Apr. 22, 2002. Technical report.
- [2] WiMedia. The worldwide ultra-wideband platform for wireless multimedia. *Wireless Symposium*, Jun. 2007.
- [3] M. Abtahi, M. Dastmalchi, S. LaRochelle, and L.A. Rusch. Generation of Arbitrary UWB Waveforms by Spectral Pulse Shaping and Thermally-Controlled Apodized FBGs. *IEEE Journal of Lightwave Technology*, 27(23):5276 –5283, Dec. 2009.
- [4] Jeff Foerster and Qinghua Li. UWB Channel Modeling Contribution from Intel. *IEEE P802.15 Working Group*, 24 June, 2002.
- [5] I. Arnedo, I. Arregui, M. Chudzik, A. Lujambio, M.A.G. Iaso, T. Lopetegi, J.D. Schwartz, J. Azaña, and D.V. Plant. Arbitrary UWB pulse generation and optimum matched-filter reception. *IEEE International Conference on Ultra-Wideband*, pages 43 –48, 2009.
- [6] D.D. Wentzloff and A.P. Chandrakasan. Gaussian pulse generators for subbanded ultra-wideband transmitters. *IEEE Transactions on Microwave Theory and Techniques*, 54(4):1647 – 1655, June 2006.
- [7] Enbo Zhou, Xing Xu, K.S. Lui, and K.K.Y. Wong. Photonic ultrawideband pulse generation with hnl-dsf-based phase and intensity modulator. *IEEE Photonics Technology Letters*, 23(7):396 –398, April, 2011.
- [8] Q. Wang and J. Yao. UWB doublet generation using nonlinearly-biased electro-optic intensity modulator. *Electronics Letters*, 42(22):1304 –1305, 2006.
- [9] Tien-Thang Pham, Xianbin Yu, L. Dittmann, and I.T. Monroy. Integration of Optically Generated Impulse Radio UWB Signals Into Baseband WDM-PON. *IEEE Photonics Technology Letters*, 23(8):474 –476, April 2011.

- [10] J. Chou, Y. Han, and B. Jalali. Adaptive RF-phonic arbitrary waveform generator. *IEEE Photonics Technology Letters*, 15(4):581–583, 2003.
- [11] M. Abtahi, M. Mirshafiei, S. LaRochelle, and L.A. Rusch. All-Optical 500-Mb/s UWB Transceiver: An Experimental Demonstration. *IEEE Journal of Lightwave Technology*, 26(15):2795 –2802, Aug. 2008.
- [12] D. Porcino and W. Hirt. Ultra-wideband radio technology: potential and challenges ahead. *IEEE Communications Magazine*, 41(7):66–74, 2003.
- [13] M. Ghavami, L.B. Michael, and R. Kohno. *Ultra wideband signals and systems in communication engineering*. John Wiley & Sons, 2004.
- [14] T. M. Cover and J. A. Thomas. *Elements of Information Theory*. John Wiley & Sons, 2001.
- [15] Intel white paper on "Ultra-wideband (UWB) technology," .
- [16] P. Smyth. *Mobile and wireless communications: key technologies and future applications*. Peter Peregrinus Ltd, 2004.
- [17] Xianren Wu, Zhi Tian, T.N. Davidson, and G.B. Giannakis. Optimal waveform design for UWB radios. *IEEE International Conference on Acoustics, Speech, and Signal Processing*, 4:521 – 524, May 2004.
- [18] A. Azakkour, M. Regis, F. Pourchet, and G. Alquié. A new integrated monocy-  
cle generator and transmitter for ultra-wideband (UWB) communications. *IEEE Radio Frequency integrated Circuits (RFIC) Symposium*, pages 79 – 82, June 2005.
- [19] J.D. Schwartz, J. Azana, N. Zicha, and D.V. Plant. Design and analysis of a compact UWB pulse generator with programmable pulse shape. *IEEE International Conference on Ultra-Wideband*, pages 38 –42, Sept. 2009.
- [20] Xin Wang, Siqiang Fan, He Tang, Lin Lin, Jian Liu, Qiang Fang, Hui Zhao, A. Wang, Li wu Yang, and Bin Zhao. A Whole-Chip ESD-Protected 0.14-pJ/p-mV 3.1-10.6-GHz Impulse-Radio UWB Transmitter in 0.18-um CMOS. *IEEE Transactions on Microwave Theory and Techniques*, 59(4):1109 –1116, April 2011.
- [21] Chao Wang, Fei Zeng, and Jianping Yao. All-fiber ultrawideband pulse generation based on spectral shaping and dispersion-induced frequency-to-time conversion. *IEEE Photonics Technology Letters*, 19(3):137–139, 2007.

- [22] I.S. Lin, J.D. McKinney, and A.M. Weiner. Photonic synthesis of broadband microwave arbitrary waveforms applicable to ultra-wideband communication. *IEEE Microwave and Wireless Components Letters*, 15(4):226 – 228, April 2005.
- [23] Fei Zeng and Jianping Yao. Ultrawideband Impulse Radio Signal Generation Using a High-Speed Electrooptic Phase Modulator and a Fiber-Bragg-Grating-Based Frequency Discriminator. *IEEE Photonics Technology Letters*, 18(19):2062 –2064, Oct., 2006.
- [24] Q. Wang and J. Yao. Switchable optical UWB monocycle and doublet generation using a reconfigurable photonic microwave delay-line filter. *Optics Express*, 15(22):14667–14672, 2007.
- [25] Q. Wang, F. Zeng, S. Blais, and J. Yao. Optical ultrawideband monocycle pulse generation based on cross-gain modulation in a semiconductor optical amplifier. *Optics letters*, 31(21):3083–3085, 2006.
- [26] A. Zadok, X. Wu, J. Sendowski, A. Yariv, and A.E. Willner. Reconfigurable Generation of High-order Ultra-wideband Waveforms Using Edge Detection. *Journal of Lightwave Technology*, 28(16):2207–2212, 2010.
- [27] Kaszubowska-Anandarajah, A. and Barry, L.P. UWB system based on Gain-Switched Laser. *International Topical Meeting on Microwave Photonics*, pages 1 –4, Oct. 2006.
- [28] H. Shams, A. Kaszubowska-Anandarajah, P. Perry, P. Anandarajah, and L.P. Barry. Electro-optical generation and distribution of ultrawideband signals based on the gain switching technique. *IEEE/OSA Journal of Optical Communications and Networking*, 2(3):122–130, 2010.
- [29] S. Pan and J. Yao. Ir-uwband-over-fiber systems compatible with wdm-pon networks. *IEEE Journal of Lightwave Technology*, 29(20):3025–3034, 2011.
- [30] K. Grobe and J.-P. Elbers. Pon in adolescence: from tdma to wdm-pon. *IEEE Communications Magazine*, 46(1):26 –34, Jan. 2008.
- [31] D. Pozar. *Microwave engineering*. John Wiley & Sons, 2005.
- [32] A.F. Molisch. Ultrawideband propagation channels-theory, measurement, and modeling. *IEEE Transactions on Vehicular Technology*, 54(5):1528–1545, 2005.

- [33] A.F. Molisch, J.R. Foerster, and M. Pendergrass. Channel models for ultrawide-band personal area networks. *IEEE Wireless Communications*, 10(6):14–21, 2003.
- [34] Witrisal, K. and Leus, G. and Janssen, G. and Pausini, M. and Troesch, F. and Zasowski, T. and Romme, J. Noncoherent ultra-wideband systems. *IEEE Signal Processing Magazine*, 26(4):48–66, July 2009.
- [35] M.E. Sahin, I. Guvenc, and H. Arslan. Optimization of energy detector receivers for UWB systems. *IEEE Vehicular Technology Conference*, pages 1386 – 1390, May 2005.
- [36] M. Mirshafiei, A. Ghazisaeidi, D. Lemus, and L.A. Rusch. Optical generation of uwb waveform via upconversion of gain-switched laser pulses. *23rd Annual Meeting of the IEEE Photonics Society*, pages 655–656, Nov. 2010.
- [37] P. Lombard, Y. Le Guennec, G. Maury, E. Novakov, and B. Cabon. Optical distribution and upconversion of MB-OFDM in ultrawide-band-over-fiber systems. *IEEE Journal Lightwave Technology*, 27(9):1072–1078, 2009.
- [38] G.H. Nguyen, B. Cabon, and Y. Le Guennec. Generation of 60-GHz MB-OFDM signal-over-fiber by up-conversion using cascaded external modulators. *IEEE Journal of Lightwave Technology*, 27(11):1496–1502, 2009.
- [39] Y. Le Guennec and R. Gary. Optical Frequency Conversion for Millimeter-Wave Ultra-Wideband-Over-Fiber Systems. *IEEE Photonics Technology Letters*, 19(13):996–998, July 2007.
- [40] Beltran, M. and Morant, M. and Perez, J. and Llorente, R. and Marti, J. Photonic generation and frequency up-conversion of impulse-radio UWB signals. *IEEE Lasers and Electro-Optics Society, LEOS*, pages 498–499, Nov. 2008.
- [41] David Lemus. Laser source for UWB pulse generation. Master’s thesis, Laval University, Quebec, Canada, 2011.
- [42] J.D. McKinney, I.S. Lin, and A.M. Weiner. Shaping the power spectrum of ultra-wideband radio-frequency signals. *IEEE Transactions on Microwave Theory and Techniques*, 54(12):4247–4255, 2006.
- [43] M. Abtahi, J. Magne, M. Mirshafiei, L.A. Rusch, and S. LaRochelle. Generation of Power-Efficient FCC-Compliant UWB Waveforms Using FBGs: Analysis and Experiment. *IEEE Journal of Lightwave Technology*, 26(5):628–635, March 2008.

- [44] J.D. McKinney. Background-Free Arbitrary Waveform Generation via Polarization Pulse Shaping. *IEEE Photonics Technology Letters*, 22(16):1193–1195, Aug. 2010.
- [45] Mehrdad Mirshafiei, Mohammad Abtahi, Patrick Larochelle, and Leslie Rusch. Pulse shapes that outperform traditional UWB Antenna/Waveform combinations. *IEEE Globecom 2010 - Wireless Communications Symposium (GC10 - WC)*, Dec. 2010.
- [46] M.E. Sahin and H. Arslan. Inter-symbol interference in high data rate UWB communications using energy detector receivers. *IEEE International Conference on Ultra-Wideband*, pages 176–179, Sept. 2005.
- [47] M. Mirshafiei and L.A. Rusch. Equalizer complexity/performance trade-offs for high data-rate IR-UWB linear receivers in multipath channels. *IEEE International Conference on Ultra-Wideband*, pages 215–219, Sept. 2011.
- [48] J.G. Proakis and M. Salehi. *Digital communications*. McGraw-Hill, 1995.
- [49] Shilong Pan and Jianping Yao. UWB-Over-Fiber Communications: Modulation and Transmission. *IEEE Journal of Lightwave Technology*, 28(16):2445–2455, Aug. 2010.
- [50] Xianbin Yu, T.B. Gibbon, and I.T. Monroy. Experimental Demonstration of All-Optical 781.25-Mb/s Binary Phase-Coded UWB Signal Generation and Transmission. *IEEE Photonics Technology Letters*, 21(17):1235–1237, Sept. 2009.
- [51] Pham, T.T. and Guerrero Gonzalez, N. and Yu, X. and Zibar, D. and Dittmann, L. and Tafur Monroy, I. Robust BPSK Impulse Radio UWB-over-Fiber Systems Using Optical Phase Modulation. *Optical Fiber Communication Conference*, 2011.
- [52] M. Mirshafiei, M. Dastmalchi, M. Abtahi, S. LaRochelle, and L.A. Rusch. Optical distribution of UWB: Low complexity pulse generation supporting OOK and PSK. *IEEE Topical Meeting on Microwave Photonics*, pages 346–349, Oct. 2010.
- [53] M. Abtahi and L.A. Rusch. RoF Delivery over PONs of Optically Shaped UWB Signals for Gigabit/s Wireless Distribution in the Home. *IEEE Journal on Selected Areas in Communications*, 29(6):1304–1310, June 2011.
- [54] F. Liu, T. Wang, Z. Zhang, M. Qiu, and Y. Su. On-chip photonic generation of ultra-wideband monocycle pulses. *Electronics Letters*, 45(24):1247–1249, Nov. 2009.



- [55] Marpaung, D. and Chevalier, L. and Burla, M. and Roeloffzen, C. Impulse radio ultrawideband pulse shaper based on a programmable photonic chip frequency discriminator. *Optics Express*, 19(25):24838–24848, 2011.
- [56] J. Xu H. Hou X. Zhang D. Huang Y. Ding, C. Peucheret. Ultra-wide band signal generation using a silicon micr-ring resonator. *IEEE Photonics Conference*, pages 258–259, 2011.
- [57] Y. Yue, H. Huang, L. Zhang, J. Wang, J.Y. Yang, O.F. Yilmaz, J.S. Levy, M. Lipson, and A.E. Willner. Experimental demonstration of uwb monocycle pulse generation using two-photon absorption in a silicon waveguide. *European Conference on Optical Communication, ECOC*, pages 1–3, 2011.
- [58] M.H. Khan, H. Shen, Y. Xuan, L. Zhao, S. Xiao, D.E. Leaird, A.M. Weiner, and M. Qi. Ultrabroad-bandwidth arbitrary radiofrequency waveform generation with a silicon photonic chip-based spectral shaper. *Nature Photonics*, 4(2):117–122, 2010.
- [59] D. Taillaert, Harold Chong, P.I. Borel, L.H. Frandsen, R.M. De La Rue, and R. Baets. A compact two-dimensional grating coupler used as a polarization splitter. *IEEE Photonics Technology Letters*, 15(9):1249 –1251, Sept. 2003.
- [60] R. Jones, J. Doylend, P. Ebrahimi, S. Ayotte, O. Raday, and O. Cohen. Silicon photonic tunable optical dispersion compensator. *Optics Express*, 15(24):15836, 2007.
- [61] N. Rouger, L. Chrostowski, and R. Vafaei. Temperature effects on silicon-on-insulator (SOI) racetrack resonators: A coupled analytic and 2-D finite difference approach. *Journal of Lightwave Technology*, 28(9):1380–1391, 2010.
- [62] A.B. Fallahkhair, K.S. Li, and T.E. Murphy. Vector finite difference modesolver for anisotropic dielectric waveguides. *IEEE Journal of Lightwave Technology*, 26(11):1423–1431, 2008.
- [63] P. Dumon, W. Bogaerts, V. Wiaux, J. Wouters, S. Beckx, J. Van Campenhout, D. Taillaert, B. Luyssaert, P. Bienstman, D. Van Thourhout, and R. Baets. Low-loss SOI photonic wires and ring resonators fabricated with deep UV lithography. *IEEE Photonics Technology Letters*, 16(5):1328 –1330, May 2004.
- [64] F. Zito, D. Pepe, and D. Zito. UWB CMOS Monocycle Pulse Generator. *IEEE Transactions on Circuits and Systems*, 57(10):2654 –2664, Oct. 2010.

- [65] Zhefeng Hu, Junqiang Sun, Jing Shao, and Xinliang Zhang. Filter-Free Optically Switchable and Tunable Ultrawideband Monocycle Generation Based on Wavelength Conversion and Fiber Dispersion. *IEEE Photonics Technology Letters*, 22(1):42–44, Jan 2010.
- [66] G. Quintero, J.F. Zurcher, and A. Skrivervik. Omnidirectional pulse dispersion of planar circular monopoles. *IEEE International Conference on Ultra-Wideband*, pages 395–399, Sept. 2009.
- [67] O. Ahmed and A. R. Sebak. A Printed Monopole Antenna With Two Steps and a Circular Slot for UWB Applications. *IEEE Antennas and Wireless Propagation Letters*, 7:411–413, 2008.
- [68] N.C. Beaulieu and Bo Hu. On determining a best pulse shape for multiple access ultra-wideband communication systems. *IEEE Transactions on Wireless Communications*, 7(9):3589–3596, Sept. 2008.
- [69] J. Timmermann, A.A. Rashidi, E. Pancera, T. Zwick, and P. Walk. Application of optimal pulse design in non-ideal ultra-wideband transmission. *German Microwave Conference*, pages 1–4, 2009.
- [70] J.F. Sturm. Using SeDuMi 1.02, a MATLAB toolbox for optimization over symmetric cones. *Optimization methods and software*, 11(1):625–653, 1999.
- [71] Jianxin Liang, C.C. Chiau, Xiaodong Chen, and C.G. Parini. Study of a printed circular disc monopole antenna for UWB systems. *IEEE Transactions on Antennas and Propagation*, 53(11):3500–3504, Nov. 2005.
- [72] Keren Li, D. Kurita, and T. Matsui. A novel UWB bandpass filter and its application to UWB pulse generation. *IEEE International Conference on Ultra-Wideband.*, pages 446–451, Sept. 2005.
- [73] B. Lindoff and P. Malm. BER performance analysis of a direct conversion receiver. *IEEE Transactions on Communications*, 50(5):856–865, May 2002.
- [74] Hamidi, E. and Weiner, A.M. Post-Compensation of Ultra-Wideband Antenna Dispersion Using Microwave Photonic Phase Filters and Its Applications to UWB Systems. *IEEE Transactions on Microwave Theory and Techniques*, 57(4):890–898, April 2009.

- [75] Arnedo, I. and Laso, M.A.G. and Falcone, F. and Benito, D. and Lopetegi, T. A Series Solution for the Single-Mode Synthesis Problem Based on the Coupled-Mode Theory. *IEEE Transactions on Microwave Theory and Techniques*, 56(2):457–466, Feb. 2008.
- [76] C. Carbonelli and U. Mengali. Synchronization algorithms for UWB signals. *IEEE Transactions on Communications*, 54(2):329–338, 2006.
- [77] B. Sklar. How I learned to love the trellis. *IEEE Signal Processing Magazine*, 20(3):87 – 102, May 2003.
- [78] F. Troesch, T. Zasowski, and A. Wittneben. Non-Linear UWB Receivers with MLSE Post-Detection. *IEEE Vehicular Technology Conference*, pages 468 –472, May 2008.
- [79] S.U.H. Qureshi. Adaptive equalization. *Proceedings of the IEEE*, 73(9):1349 – 1387, Sept. 1985.
- [80] A. Batra, J. Balakrishnan, G.R. Aiello, J.R. Foerster, and A. Dabak. Design of a multiband OFDM system for realistic UWB channel environments. *IEEE Transactions on Microwave Theory and Techniques*, 52(9):2123 – 2138, Sept. 2004.
- [81] G. Durisi and S. Benedetto. Comparison between coherent and noncoherent receivers for UWB Communications. *EURASIP Journal on Applied Signal Processing*, 3:359–368, 2005.
- [82] B. Sklar. *Digital communications*. Prentice-Hall, Englewood Cliffs, NJ, 1988.